University of Alberta

ELASTIC BEAM MODELS FOR DYNAMICS OF MULTIWALL CARBON NANOTUBES

By

Juil Yoon

A thesis submitted to the Faculty of Graduate Studies and Research in partial fulfillment of the requirements for the degree of

Doctor of Philosophy

Department of Mechanical Engineering

Edmonton, Alberta
Spring, 2006

Your file Votre référence
ISBN: 0-494-14068-2
Our file Notre référence
ISBN: 0-494-14068-2

This Dissertation is dedicated to my parents, to my wife and to my son.

Abstract

Since the discovery of carbon nanotubes (CNTs) in 1991, extensive research related to the nanotubes in the fields of physics, material science and mechanical and electrical engineering has been came out. Most potential applications of CNTs are heavily based on a thorough understanding of their mechanical behavior. For this reason, numerous experiments and atomistic simulations have been conducted to study mechanical behavior of CNTs. Since these methods meet many difficulties, solid mechanics models offer an effective alternative method for CNTs. In this dissertation, several elastic beam models, which account for the interlayer van der Waals interaction and radial displacements, have been developed to study dynamics of multiwall CNTs (MWNTs), such as free vibration, sound wave propagation and flow-induced instability.

First, using a multiple-Euler-beam model, non-coaxial vibration of MWNTs is predicted for the first time in the literature. This novel phenomenon, first predicted by the present model, has been confirmed by more recent molecular dynamic simulations. Moreover, the multiple-Euler-beam model is used to study wave

propagation in MWNTs. Our results show that sound wave propagation in MWNTs is essentially coaxial only when the frequency is much below a critical frequency.

When the aspect ratio of MWNTs is about or below 20, the wavelength of the higher-order modes is just few times the outermost diameter. In this case, rotary inertia and shear deformation would have a significant effect on dynamics of CNTs. For this reason, a multiple Timoshenko-beam model is developed to study vibration of short CNTs. The results predicted have been found to be in good agreement with more recent molecular dynamics simulations for wavelengths down to about 1nm. These results suggest that elastic beam models would be valid for CNTs even at very small scale provided some subtle factors can be further taken into account.

Finally, the influence of internal moving fluid on free vibration and flow-induced structural instability of CNTs is studied based on a simple Euler-beam model. The results indicate that internal moving fluid could substantially affect resonant frequencies especially for longer suspended CNTs of larger innermost radius at higher flow velocity, and the critical flow velocity for structural instability in some cases could fall within the range of practical significance.

Acknowledgements

I would like to extend my deepest gratitude and appreciation to Drs. Chongqing Ru and Andrew Mioduchowski for their invaluable guidance, support and encouragement throughout my graduated years.

I am also grateful to my parents, my wife and my son for their patience, love and support throughout my studies

Content

The List of Tables

The List of Figures

Chapter 1

Introduction

1.1 Carbon Nanotubes (CNTs)

Carbon is an extraordinary element, considering the diversity of materials it forms. Carbon-based materials have been studied and used for centuries, and carbon science was long thought to be a mature field until a completely new form of carbon materials – the fullerenes, such as C_{60}, C_{70} and C_{80} – was discovered in 1985. With the study of C_{60} and C_{70}, it was soon realized that an infinite variety of closed graphitic structures could be formed. In 1991, Sumio Iijima [1] of NEC discovered the carbon nanotubes, which appeared perfectly graphitized (i.e. the carbon atoms are in perfect hexagonal arrangement) and capped at each end with pentagons, just like the fullerene molecules.

The discovery of CNTs in 1991 [1] has stimulated world-wide research activities in science and engineering devoted to carbon nano-structure and their applications, since CNTs are only a few nanometers in diameter, having extraordinary mechanical, electrical and thermal properties while providing strong, light and high toughness characteristics [2-7]. To mention a few, CNTs are about 6 times lighter and 10 times stronger than steel, can conduct electricity better than copper and transmit heat better than diamonds, and can

sustain large elastic strain more than 5%. Therefore, CNTs may find use in a wide range of applications in nanoelectronics [8-14], nanodevices [15-22], and super-strong nano-composites [23-32]. For example, it has been suggested that the CNTs could be used to design a 23,000 mile cable from a space station to Earth without suffering a high gravitation force due to its own weight at that length [29].

1.1.1 Molecular Structure of CNTs

The first CNTs discovered by Iijima in 1991 [1] were multiwall carbon nanotubes (MWNTs) in Fig. 1.1. About two years later, he made the observations of single wall carbon nanotubes (SWNTs). A MWNT consists of an array of such SWNT with an interlayer spacing of 0.34nm, close to the interlayer separation of graphite, 0.335nm. The lengths of the two types of tubes can be up to hundreds of microns, although shorter CNTs of aspect ratio as small as 10 or 20 are used in some cases [10, 15, 17, 20-22, 33, 34].

The bonding mechanism in a CNT is similar to that of graphite, since a CNT can be thought of as a rolled-up graphite sheet. In the cylindrical plane of a CNT, each carbon atom is connected with three adjacent atoms via strong in-plane σ–bond separated from each other by 120°. This in-plane σ–bond is a strong covalent bond that binds the atoms in the plane, and results in the high stiffness and high strength of a CNT. However, different from graphite, the atomic hexagons of a CNT are arranged in a certain degree of helicity, i.e., the screw orientation with respect to the axis of a CNT. In general, the CNTs could

be specified in terms of the tube diameter d, and the chiral angle θ, which are shown in Fig. 1.2. The chiral vector $\mathbf{C_h}$ can be defined in terms of the lattice translation indices (n,m) and the basic vectors $\mathbf{a_1}$ and $\mathbf{a_2}$ of the hexagonal lattice (a layer of graphene sheet) [35], i.e.

$$\mathbf{C_h} = n\mathbf{a_1} + m\mathbf{a_2}.$$

Different types of CNTs are thus uniquely defined by of the values of n and m (Fig. 1.3). Three major categories of CNT can also be defined by chiral angle θ as follows

$\theta = 0°$,	"Zigzag"
$0° < \theta < 30°$,	"Chiral (Intermediate)"
$\theta = 30°$,	"Armchair"

Based on simple geometry, the diameter d and the chiral angle θ can be given as

$$d = 0.783\sqrt{n^2 + nm + m^2}$$

$$\theta = \sin^{-1}\left[\frac{\sqrt{3}m}{2(n^2 + nm + m^2)}\right]$$

In particular, chirality is known to have a strong impact on the electronic properties of CNTs. Graphite is considered to be a semi-metal, but it has been shown that CNTs can be either metallic or semi-conducting,

depending on tube chirality [9]. However, the chirality of CNTs has little effect on the mechanical properties such as Young's modulus [36].

1.1.2 Mechanical and Electrical Properties of CNTs

♦Mechanical properties

Many studies based on experiment and simulation have addressed that nanotubes possess high tensile modulus and strength as high as 1 TPa and 200 GPa, respectively, which belong to the framework of continuum elasticity. The most important results, based on experiment and simulation, are summarized as follows.

In 1996, Treacy et al. [37] first investigated the elastic modulus of isolated MWNTs by measuring the amplitude of their intrinsic thermal vibration in a transmission electron microscope (TEM). The average value obtained over 11 samples was 1.8 TPa. Wong et al. [38] first performed direct measurement of the stiffness and strength of MWNT with the help of an atomic force microscopy (AFM). They reported the elastic modulus to be 1.26 TPa and the average bending strength to be 14.2 ± 8 GPa. Yu et al. have investigated the tensile loading of MWNTs [39] and SWNT ropes [40]. In their work, the CNTs were attached between two opposing AFM tips and loaded under tension (Fig.1.4). The experimentally calculated tensile strengths of the outer most layers ranged from 11 to 63 GPa and the elastic modulus ranged from 270 to 950 GPa [39]. In their subsequent investigation of SWNT ropes, Yu calculated

tensile strengths of 13 to 52 GPa and average elastic modulus of 320 to 1470 GPa [40]. Yu et al. also found breaking strain 12% for MWNTs [39] and 5.3% for SWNT ropes [40].

Numerous theoretical studies were performed based on various molecular dynamic simulations. To mention a few, Yakobson et al. [41] compared molecular dynamics simulation results to the continuum shell model and thereby fitted both a value for Young's modulus 5.5 TPa and for effective thickness of the CNTs 0.066nm. Lu [36] found from his MD simulations that the Young's modulus of a SWNT is approximately 970GPa, which is close to that of a graphite plane, and is independent of diameter and chirality.

In addition to the high Young's modulus and strength, another unique feature of CNTs is their remarkable flexibility under axial compression or bending. For example, by intentionally creating large curvature bends in MWNTs, Falvo et al. [42] observed buckles and periodic ripples. They reported that some MWNTs could sustain up to 16% strain without obvious structural or mechanical failure (Fig. 1.5). Similarly, Lourie et al. [23] observed that MWNTs can be bent to a large angle in excess of 90° or even 100°.

In summary, the CNTs are stronger than any other materials, but only one-sixth as heavy. Although the scatterings of the measured results have been found in different literatures, according to numerous previous studies, Young's modulus 1TPa (with the wall thickness 0.34nm) are in broad agreement with each other. Moreover, Validity of elastic models (especially beam models) for CNTs is confirmed by numerous experimental fitting to mechanical

measurements of the Young's modulus of CNTs, which have been mostly made by assuming the CNTs to be elastic beams. Here, it is worth mentioning that, since the high in-plane rigidity and strength as well as low density of CNTs are, in fact, inherited from in-plane properties of graphite, it is this extraordinary resilience and resistance to fracture that distinguish CNTs from graphite.

♦ **Electronic properties**

The electronic properties of CNTs are sensitively depended on the nanotube's diameter and chirality. These properties are uniquely characterized by the chiral vector [6, 9]. For example, the armchair nanotubes (n=m) possess metallic properties. However, for all other CNTs with chiral indices of (n,m) and (n,0), two possible intrinsic properties exist. When n-m=3p (where p is an integer), the CNTs are expected to be metallic. In the rest case, the CNTs are predicted to be semi-conducting materials.

In addition, CNTs have extremely low electrical resistance [6, 9, 43]. Resistance occurs when an electron collides with some defect in the crystal structure of the material through which it is passing. The electrons inside CNTs are not so easily scattered because of their very small diameter and huge ratio of length to diameter. Since any scattering gives rise to electrical resistance, this reduced scattering gives CNTs their very low resistance. Moreover, superconductivity, which is characterized by the complete absence of electrical resistance, is another novel electronic property of CNTs. Recently, a Chinese research group from Hong Kong has developed individual SWNT of very small

diameter 0.4nm that demonstrate superconducting behavior at around 15K [44].

Another important issue is nanotube electromechanical properties. The effects of mechanical deformation to the electrical properties of CNTs were studied by several groups [45-50] due to the potential application of CNTs such as nanoscale electro-mechanical devices. For example, Tombler et al. [50] investigated by experiment the electromechanical properties of CNTs. The CNT conductance decreases when the AFM tip pushes the CNTs down, but recovers as the tip retracts. The conductance is found to decrease by a factor of 2 at ~5° bending angle (strain ~3%), but decreases more dramatically by two orders of magnitude at a bending angle ~14° (strain ~3%) in Fig. 1.6.

1.1.3 Applications of CNTs

As shown above, CNTs have extraordinary mechanical and electrical properties. These properties provide substantial promise for CNTs as the leading candidate material for nanoelectronics [8-14], nanodevices [15-22], and super-strong nano-composites [23-32]. The most important applications of CNTs are briefly summarized as follows.

♦ **Nanoelectronics**

An application of CNTs is not a future dream any more and has already been developed in some areas. One use of CNTs is for extremely fine electron guns, which could be used as miniature cathode ray tubes (CRTs) in thin high-brightness low-energy low-weight displays. This type of display would consist

of a group of many tiny CRTs, each providing the electrons to hit the phosphor of one pixel, instead of having one giant CRT whose electrons are aimed using electric and magnetic fields. These displays are known as Field Emission Display (FED). For example, FED having CNT emitters has been fabricated for several years in Samsung [13]. Such devices have shown superior qualities, such as high emission current density and high stability.

One possible future application of CNTs is the exploration of so-called molecular electronics [10, 14]. Dreams about the use of single molecules as active electronic elements have been around for decades. Experimental realization of such dreams has proved hard, but interest in these ideas has been revived with the advent of nanotube molecules. Recently, Rueckes et al. [10] demonstrated the potential of CNT-based molecular device element and molecular wires for reading and writing information. Each device element is based on a suspended, crossed CNTs geometry that leads to bi-stable, electrostatically switchable on/off states. Such CNT device elements can be used both as nonvolatile RAM and as configurable logic tables and thus could serve as the key building blocks for a molecular-scale computer.

♦ **Nanodevices**

Another example for CNTs is probes for atomic force microscopy [15, 20]. For example, Snow et al. [20] examined the factors that govern the stability of imaging using SWNTs as probes for atomic force microscopy. They found the elastic response, due to non-vertical alignment of the CNTs, causes the CNT

tip to jump into contact with the surface and renders it unsuitable for imaging for long CNTs. For short CNTs (aspect ratio = 15~30), stable noncontact-mode imaging can be achieved using a small cantilever vibration amplitude. Their result reveals the limitations of SWNTs AFM probes and suggests that thicker, MWNT probes or very short SWNT probes might be better candidates for imaging.

Kim and Lieber [17] used CNTs to create nanotweezers that can be utilized for nanoscale manipulation and measurement. Attaching two thin and rigid CNTs to electrodes on glass rod forms these nanotweezers, which can be opened and closed by changing voltage applied on the two tubes. Their experiments demonstrate that these nanotweezerc can be readily grab and manipulate nanostructres which was 500nm in size.

♦ Nanofluidic devices

Because of perfect hollow cylindrical geometry and superior mechanical strength, CNTs hold substantial promise as nanocontainers for gas storage, and nanopipes for conveying fluid. For example, CNTs can act as inner-connects between microfluidic chips or between a chip (such as a drug delivery system) and the subject (such as cell). CNTs that act like tiny straws could deliver medicines, slowly and over time, to a person's bloodstream or to a highly specific location in the body [51]. In 1997, Gadd et al. [52] succeeded in trap argon gas at high pressure within hollow CNTs, which had an outer diameter of between 20 and 150nm. This filled tubes were found to retain their Ar content

over several months at room temperature with little change. These findings demonstrate the potential for storing gases in such CNTs. Che et al. [53] demonstrated that both the outer and inner CNT tubules are electrochemically active in intercalation of lithium-ion, suggesting possible applications in lithium-ion battery.

♦ **Super-strong nano-composites**

CNTs should be the ideal reinforcing fibers for composites due to their exceptional mechanical properties. Qian et al. [26] have reported that by adding 1% of nanotubes into polystyrene matrices resulted in increases of over all tensile modulus and strength by approximately 42 and 25%, respectively. For example, this kind super strong material is ideal for space industries. NASA Johnson Space Center (JSC) is developing materials using CNTs for space applications [32], where weight-driven cost is the major concern. Composites based on CNTs could offer strength to weight ratios beyond any materials currently available. Another space application of CNTs is space cable, which has been suggested by Harris [29]. He estimated that the CNTs could be designed as the longest cable in the world, which connects space station and Earth without suffering a high gravitation force due to its own weight at that length. Because of enormous resilience and tensile strength, in the future, embedded into a composite, CNTs could be used to make cars that bounce in a wreck or buildings that sway rather than crack in an earthquake [9].

1.2 Recent Studies on CNT Mechanics

As reviewed in previous section, CNTs have been identified as one of the most promising building blocks for future development of nano-structures. Thus, the mechanical behavior of CNTs has been the subject of numerous experimental, atomistic simulations, and elastic continuum modeling studies.

1.2.1 Experimental Research

The small dimensions of CNTs, with diameter of tens of nanometers for MWNTs and about 1nm for SWNTs, and lengths of the order of microns, impose challenges for experimental determination of mechanical behavior and properties. Nevertheless, several experimental studies based on transmission electronic microscopy (TEM), scanning electronic microscopy (SEM), atomic force microscopy (AFM), have been attempted to measure the mechanical properties. The most important experiments based on these techniques are summarized as follows.

♦ SEM method

Electron Microscopes such as SEM and TEM are scientific instruments that use a beam of highly energetic electrons to examine objects on a very fine scale. Electron Microscopes uses high-energy electron beams for scattering and diffraction, which allows the achievement of high resolving power, including down to sub-nanometer resolution because of the extremely short wavelength of electrons at high kinetic energy.

Yu et al. have investigated the tensile loading of MWNTs [39] and SWNT ropes [40], with the help of SEM and AFM (Fig. 1.4). The individual CNTs were attached to AFM probes inside the SEM. The measured force versus elongation data were converted, by SEM measurement, to a stress versus strain curve and the breaking strength of each CNT was obtained by measuring the maximum tensile loading force at break. More recently, Waters et al. [54] studied axially compressed buckling for short MWNTs using a SEM.

♦ TEM method

Since TEMs normally have a better resolution than SEMs, TEMs are widely used in experimental research. Using TEM images, Treacy et al. [37] were able to deduce values for Young's modulus for individual MWNTs. They measured the amplitude from recorded TEM images of the thermal vibration of cantilevered MWNTs.

Poncharal et al. [55] designed a TEM holder to study the mechanical resonance of cantilevered MWNTs, and measured the bending modulus. In their experiment, when the frequency of the input AC signal matched the mechanical resonance frequency of the MWNTs, oscillation corresponding to the resonance mode of the cantilever MWNTs was observed (Fig.1.7) and the resonance frequency of the MWNTs thereby determined. The radial deformability for tubes has also been studied using TEM images. Ruoff et al. [56] first studied radial deformation between adjacent nanotubes. Partial flattening due to van der Waals forces was observed in TEM images of two adjacent and aligned

MWNTs along the contact region. Numerous buckling of CNTs was observed via TEM study. For example, Iijima et al. [57] observed kinks or local buckling on the inner side of a bent CNT due to compression. Lourie et al. [23] and Bower et al. [25] were able to investigate buckling behaviors of MWNTs embedded within a polymer matrix.

♦ AFM method

The AFM is a very powerful microscope invented in 1986. The AFM consists of a cantilever with a sharp tip at its end with tip sizes on the order of nanometers. The tip is brought into close proximity of a sample surface. The force between the tip and the sample leads to a deflection of the cantilever. Typically, the deflection is measured using a laser spot reflected from the top of the cantilever into detector. The AFM operated in either lateral force mode, contact mode, or tapping mode has been the main tool in studying the mechanical response of CNTs under static load.

Wong et al. [38] first performed direct measurement of the stiffness and strength of individual, structurally isolated MWNTs using AFM operated in lateral force mode. The CNT was pinned at one end and load was applied to the tube by means of the AFM tip. The bending force was measured as a function of displacement along the unpinned length, and a value of 1.26 TPa was obtained for the elastic modulus. Using contact mode AFM, Falvo et al. [42] directly applied bending force to a MWNT and repeatedly bent it through large angles in various configurations and thus buckles and periodic ripples were

observed (Fig. 1.5). By using an AFM and a special substrate, Salvetat et al. [58, 59] measured the elastic and shear modulus of SWNT ropes and MWNT. By AFM tip applying a load to the portion of CNTs with a suspended length, the maximum deflection at the center of the beam is directly measured (Fig. 1.8). Therefore force versus deflection curves were obtained and compared with theoretical modeling based on beam mechanics.

1.2.2 Atomistic Simulations

Numerical computer simulations of the finite sample systems have been widely used to describe mechanical behavior of CNTs. There are three major categories of atomistic simulation methods: classical molecular dynamics (MD), tight binding molecular dynamics (TBMD), and ab initio methods. The three simulation methods have their own advantages and are suitable for studies for a variety of properties of material systems. MD simulations have least computational cost, followed by TBMD methods. Ab initio methods are the most costly among the three. With well-fitted empirical potentials, MD simulations are quite suitable for studies of dynamical properties of large-scale systems. While ab initio methods can provide highly accuracy, the high computational cost limits them to systems up to hundreds of atoms currently. Tight binding methods lay in between MD simulations and ab initio methods, as to the computational cost and accuracy, and are applicable for systems up to thousands of atoms.

♦ **MD methods**

Molecular dynamics is essentially a particle method since the objective is to solve the governing equations of particle dynamics based on Newton's second low. The MD methods for carbon based systems involves analytic many-body force field functions such as Tersoff-Brenner potentials, which is specially suited for carbon-based systems, such as diamond, graphite, fullerenes, and nanotubes. For example, Iijima et al. [57] performed to simulate buckling behaviors of SWNTs and double wall CNTs (DWNTs) under bending using classical MD simulation. Consistent with their own experimental observation, the simulation showed that buckling or kinks occurred on the concave side of a bent CNT and the number of kinks increased with the increasing bending load. Yakobson et al. [41] reported the Young's modulus to be as high as 5.5TPa, using the MD methods based on Tersoff-Brenner potential.

♦ **Ab initio methods**

Ab initio is a simulation to directly solve the complex quantum many-body Schrödinger equation. Ab initio method provides a more accurate description of quantum mechanical behavior of materials properties even though the system size is currently limited to only about few hundred atoms. For example, using ab initio based on density functional theory (DFT), Sanchez-Portal et al. [60] have found that the stiffness of SWNTs is close to that of graphite. Srivastava et al. [61] carried out axial compression of SWNT and have found Young's modulus to be about 1.2 TPa, using tight-binding

molecular dynamics (TBMD) and ab initio method based on DFT.

♦ **TBMD methods**

In the intermediate regimes, for up to few thousand atoms, the TBMD approach provides very good accuracy. For example, through a TBMD method, Hernandez et al. [62] found the Young's modulus to be approximately 1.2TPa, which is larger than that of graphite, and is slightly dependent on the tube size especially for small diameter nanotubes (less than 1.2nm). Srivastava et al. [63] used a TBMD method and have found that within the Euler buckling length limitation, an (8,0) CNT collapses locally at 12% compressive strain.

1.2.3 Elastic Models

As discussed above, numerous studies based on atomistic simulations have been done so far. Despite constant increases in available computational improvement, even classical molecular dynamics computations are still limited to simulating small scale. The simulation of larger systems or longer times must currently be left to continuum elastic model [37, 38, 55, 64-78].

Among various methods, solid mechanics models, such as elastic beam or shell, have been widely and successfully used to study static and dynamics structural behavior of CNTs. Many studies indicated "the laws of continuum mechanics are amazingly robust and allow one to treat even intrinsically discrete objects only a few atoms in diameter" [5]. For example, buckling force predicted by the Euler-beam model is in good agreement with

experimental data [77], resonant frequencies and vibrational modes of CNTs given by the cantilever beam model agree well with experiments [37, 55], and sound velocity predicted by the Euler-beam model agrees well with data obtained by other methods [78].

♦ **Elastic Beam Models**

CNTs are only few nanometers in diameter, while as long as a few mm. Therefore, aspect ratio of CNTs is usually very large, up to 1000 or beyond, although shorter CNTs of aspect ratio as small as 10 or 20 are also used in some cases, such as CNT-based nanotweezers [17] and AFM tips [15, 20, 34]. In all these cases, because there are large numbers of atoms along the longitudinal direction, elastic-rod or elastic-beam model is adequate for overall mechanical deformation of CNTs. It is known that transverse dynamics of an elastic beam under axial force F and transverse distributed pressure p(x) (per unit axial length) is governed by [79, 80]

$$p(x) + F\frac{\partial^2 w}{\partial x^2} = EI\frac{\partial^4 w}{\partial x^4} + \rho A\frac{\partial^2 w}{\partial t^2} \tag{1.1}$$

where x is the axial coordinate, t is time, w(x, t) is the deflection of the beam, I and A are the moment of inertia and the area of the cross-section of the beam, E and ρ are Young's modulus and the mass density (per unit volume). Thus, (ρA) is the mass density per unit axial length, (EI) represents the bending stiffness of

the beam, and (EA) represents the axial stiffness which is defined by the axial force divided by the axial strain (the latter does not appear explicitly in Eq (1.1)). In addition, bending moment M and transverse shear force V are given by

$$M = EI\frac{\partial^2 w}{\partial x^2}, V = EI\frac{\partial^3 w}{\partial x^3} \tag{1.2}$$

These equations provide a complete description of elastic beam model with appropriate boundary conditions (such as pinned, clamped, and free ends).

In order to apply elastic beam model (1.1) to CNTs, it is sufficient to know the mass density per unit axial length (ρA), the bending stiffness (EI), and the axial stiffness (EA). Once the three parameters are known, the deflection of CNTs can be determined by (1.1) even without knowing the details of the cross-sectional geometry (such as I and A). Recognition of this simple fact is important for understanding applicability of the elastic beam model to one-dimensional nanoscale structures, such as CNTs or DNA molecules which are only few atoms in diameter and thus doubtful about applicability of continuum models across their cross-sections. For instance, there have been different opinions on the thickness of SWNTs. Although most researchers have adopted the equilibrium interlayer spacing between adjacent nanotubes (about 0.34 nm) as the representative thickness of SWNTs combined with a Young modulus of about 1 TPa, some authors have suggested a much smaller thickness (say, 0.066 nm, [5, 41]) combined with a Young's modulus of about 5 TPa. It is obvious

that axial stiffness (EA) keeps unchanged if the Young's modulus is 5 times larger and, at the same time, the thickness is 5 times smaller. Furthermore, it is readily seen that these different definitions of thickness do not significantly affect the value of bending stiffness (EI) provided the cross-section of SWNTs is treated as a thin annulus. Thus, the governing equation (1.1) and the overall deflection of SWNTs remain essentially unchanged when these different thickness of SWNTs are adopted. More detailed examples will be shown Chapter 2.

♦ **Elastic Shell Models**

When aspect ratios of CNTs are small, or local deformation is concerned, CNTs should be treated as elastic shell rather than elastic beam. Continuum elastic shell models also have been effectively used to study static and dynamic structural behavior of CNTs, particularly in buckling problem.

Axially compressed buckling of SWNTs: Axially compressed buckling of SWNTs was studied in [65] using elastic shell model. For example, the critical strain for SWNTs of diame

SWNTs of radius 0.67nm is about 1.2nm, which is in good agreement with the value 1.3nm obtained in [82] by molecular dynamics simulations.

SWNT ropes under high pressure: An interesting phenomenon of SWNT ropes is the pressure-induced abrupt changes observed for vibrational modes and electric conductivity when the applied external pressure reached a critical value ranging from 1.5 to 1.9 GPa [83-85]. The conventional elastic honeycombs model is modified and applied to the honeycomb-like structure of SWNT ropes under high pressure [66]. For example, for SWNT ropes of diameters 1.3 nm, the critical pressure predicted by the elastic model [66] is about 1.8 GPa, in excellent agreement with the known data ranging from 1.5 GPa to 1.9 GPa [83-85].

MWNT under high pressure: Tang et al. [86] studied electronic properties of a specific group of MWNTs of about twenty layers (with the innermost radius 1.5 nm, and the outermost radius 8 nm) under high pressure. They observed that an abrupt change of conductivity of MWNTs occurs when the applied external pressure reaches a critical value about 1.5 GPa. Wang et al. [87] studied this problem with a multiple-shell model, and found that the predicted critical pressure for the MWNTs tested in [86] is about 1 GPa, in reasonably good agreement with the experimental result 1.5 GPa [86].

1.3 Contributions of the Present Work [70-76]

Most of the potential applications of CNTs are heavily based on a thorough understanding of their mechanical behavior. For example, experiments and molecular dynamics simulations showed that electronic properties of CNTs can be changed by mechanical deformations up to several orders of magnitude [45-50]. This can explain why the study of mechanical behavior of CNTs has been one topic of major concern [37-39, 41, 42, 55, 64-76, 78, 88-94].

Among various methods, solid mechanics models, such as elastic beam or shell, have been widely and successfully used to study static and dynamics structural behavior of CNTs. Particularly, elastic models provide simple formulas in many important cases, which clearly identify major factors affecting mechanical behavior of CNTs. Indeed, because controlled experiments at nanoscale are usually difficult, and molecular dynamics simulation remains expensive and formidable (especially for large sized atomic systems), solid mechanics models offer a effective alternative method for the study of CNTs. On the other hand, owing to new phenomena at nanoscale (especially for the multi-layer structure of MWNTs and the interlayer van der Waals interaction), traditional elastic models cannot be applied to CNTs in many cases of practical and academic interest. This has raised a major challenge to solid mechanics.

The present work [70-76] is based on the multiple-beam model [67], which accounts for the interlayer van der Waals interaction, and is devoted to a systematic study on the dynamics of CNTs, such as vibration, wave propagation and flow-induced instability of CNTs. The objective of this research is to study

the unique features of mechanical behavior of CNTs (especially MWNTs with interlayer van der Waals interaction) and to spark and facilitate further interest in this research topic. Since many of the results given in [70-76] are newly discovered phenomenon in CNTs mechanics, some of them cannot be compared to any known experiments and atomistic simulations available in the literature. However, some of the new results predicted by the present models [70-76], such as non-coaxial vibration of MWNTs and the relevance of Timoshenko-beam model for short wavelength dynamics of CNTs, have been well confirmed by more recent atomistic simulations conducted by other researchers [95-97].

In Chapter 2, the general formulation of several elastic beam models is outlined. The existing single-beam models are reviewed and the predicted results are compared to experiments and atomistic simulations. Particularly, the multiple-Euler-beam model and multiple-Timoshenko-beam model are developed, and the intertube van der Waals interaction coefficient is defined.

In Chapter 3, vibration of MWNTs [70, 71] is discussed, using the multiple Euler-beam model. For the first time, this research predicts that non-coaxial vibrations in MWNTs will be excited at terahertz frequencies. These results predicted by a simple multiple-beam-model [70, 71] are found to agree well with more recent molecular simulations [95, 96] on non-coaxial vibration of MWNTs. For example, Zhao et al. [95] MD simulations show that non-coaxial instability does occur for frequencies in the terahertz range. More recently, Li and Chou [96] have also found non-coaxial vibration of DWNTs using molecular structural mechanics method. Li and Chou concluded that

"This phenomenon was first reported by Yoon et al. [70] based on an elastic continuum multishell model. Our simulation results agree with Yoon et al. in that the vibration modes associated with the fundamental frequencies are almost coaxial, and non-coaxial vibrations are exited at higher frequencies." These results confirm the effectiveness of the multiple elastic beam model for MWNTs.

In Chapter 4, using the multiple-Euler-beam model, transverse sound wave propagation in MWNTs is studied [72]. It is predicted that (N-1) critical frequencies exist for an N-wall CNT, at which the number of the wave speeds changes. When the frequency is higher than at least one of the critical frequencies, non-coaxial vibrational modes emerge, which propagate along the MWNT at different wave speeds. These results represent some interesting features of wave propagation in MWNTs, which cannot be described by the existing single-beam model.

In Chapter 5, vibration of short MWNTs is discussed [74], using the multiple-Timoshenko-beam model. Because rotary inertia and shear deformation are significant for higher-order modes of shorter elastic beams, the CNTs studied here are modeled as Timoshenko-beams instead of classical Euler-beams. Detailed results are demonstrated for DWNTs of aspect ratio 10, 20 or 50, based on the Timoshenko-beam model and the Euler-beam model, respectively. This work suggests that the Timoshenko-beam model, rather than the Euler-beam model, is relevant for terahertz vibration of short CNTs.

In Chapter 6, using the multiple-Timoshenko-beam model, effects of

rotary inertia and shear deformation on transverse wave propagation in individual MWNTs are discussed [73]. The results show that the effects of rotary inertia and shear deformation are negligible and transverse wave propagation can be described satisfactorily by the existing single-Euler-beam model only when the frequency is far below the lowest critical frequency. When the frequency is very close to or higher than the lowest critical frequency, rotary inertia and shear deformation come to significantly affect the wave speed. The effects of rotary inertia and shear deformation on transverse wave propagation predicted by the present model, have been found to be in good agreement with more recent atomistic simulation [97]. Therefore, these results shows that terahertz transverse wave propagation in MWNTs should be better modeled by Timoshenko-beam model, instead of Euler-beam model.

In Chapter 7, the elastic (hollow) beam model is employed to study the CNTs conveying fluid [75]. The emphasis is on the influence of internal moving fluid on free vibration and flow-induced structural instability of CNTs. The results indicate that internal moving fluid could substantially affect resonant frequencies especially for suspended longer carbon nanotubes of larger innermost radius at higher flow velocity, and the critical flow velocity for structural instability in some cases could fall within the range of practical significance. On the other hand, even a compliant surrounding elastic medium (such as polymer matrix with 1GPa) can significantly reduce the effect of internal moving fluid on resonant frequencies, and suppress or eliminate structural instability within the practical range of flow velocity.

Chapter 8 studies the influence of internal moving fluid on free vibration and flow-induced flutter instability of cantilever CNTs [76]. In contrast to Chapter 7, non-conservative characteristics of cantilever CNTs is highlighted. Indeed, cantilever CNTs conveying fluid are damped with decaying amplitude for flow velocity below a certain critical value, while flutter instability occurs and vibration becomes amplified with growing amplitude when the flow velocity exceeds the critical value.

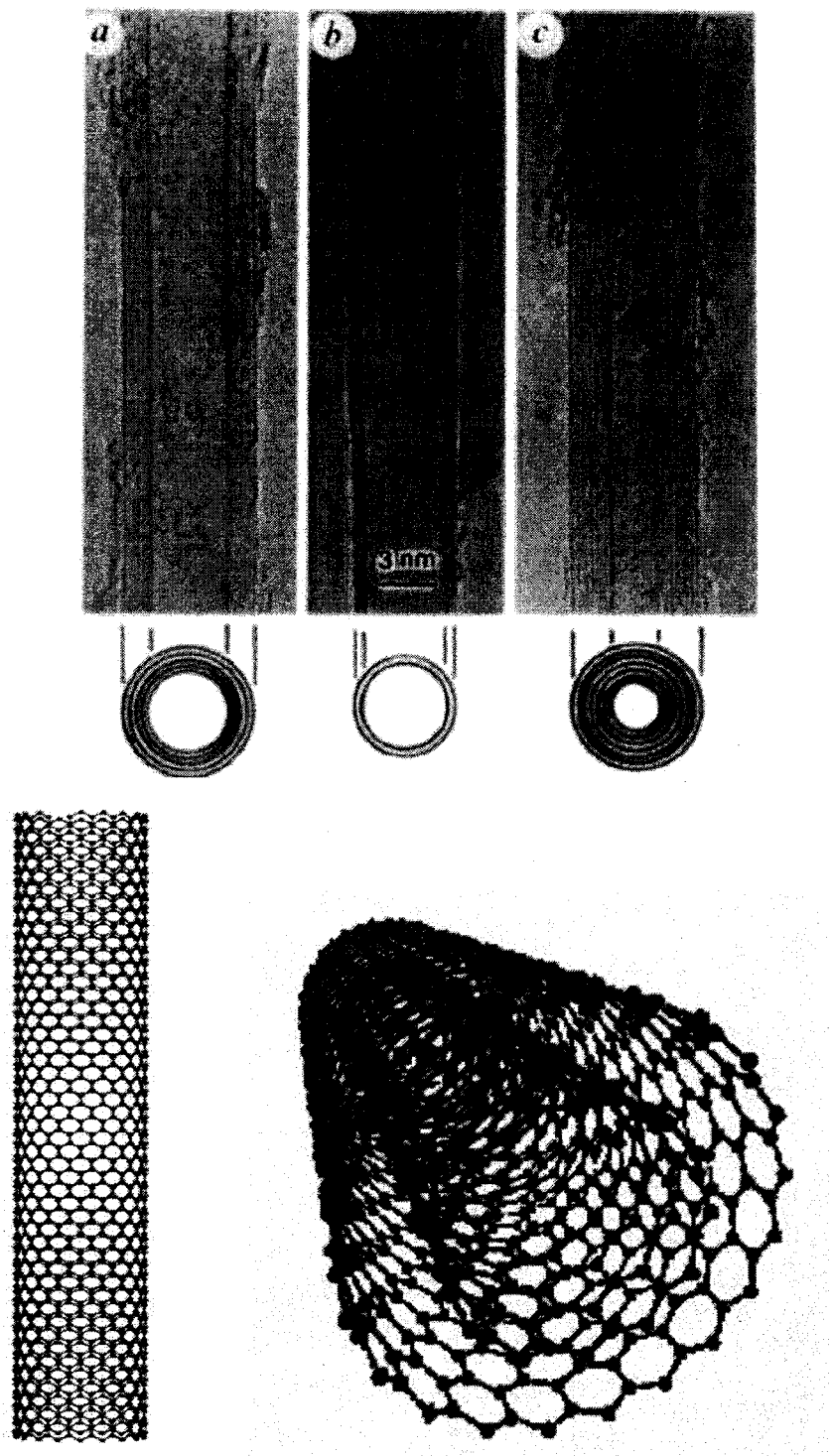

Fig. 1.1. (Top) Transmission electron microscopy (TEM) image of MWNTS [1], (Bottom) Schematic structures of SWNTs and MWNTs

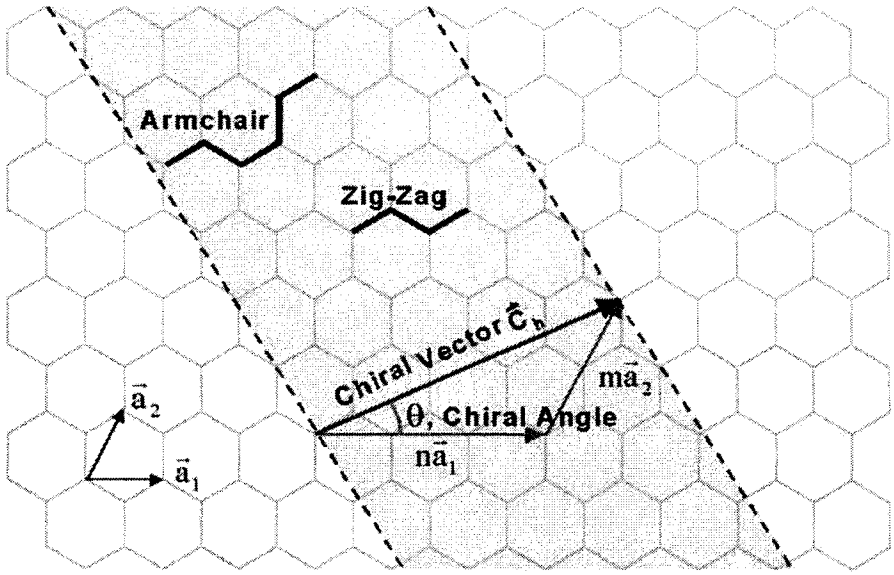

Fig 1.2. The chiral vector $\mathbf{C_h}$ is defined on the hexagonal lattice of carbon atoms by unit vectors $\mathbf{a_1}$ and $\mathbf{a_2}$ and the chiral angle θ [27]

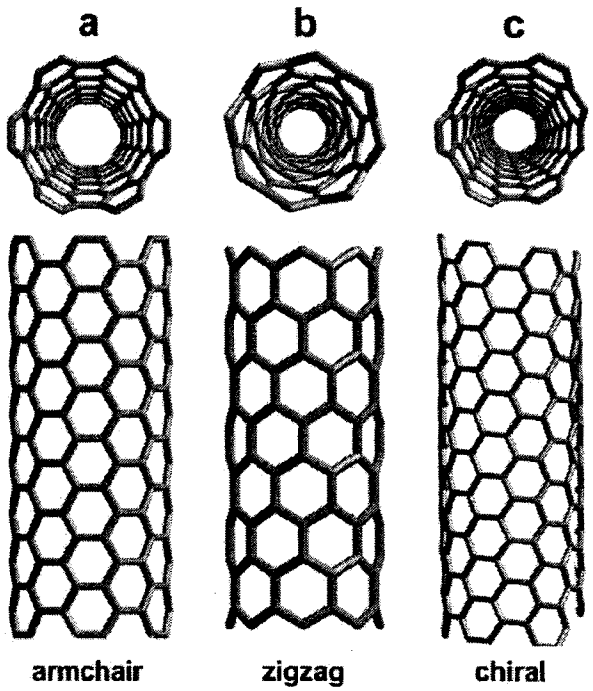

Fig. 1.3. Examples of zigzag, chiral, and arm chair CNTs

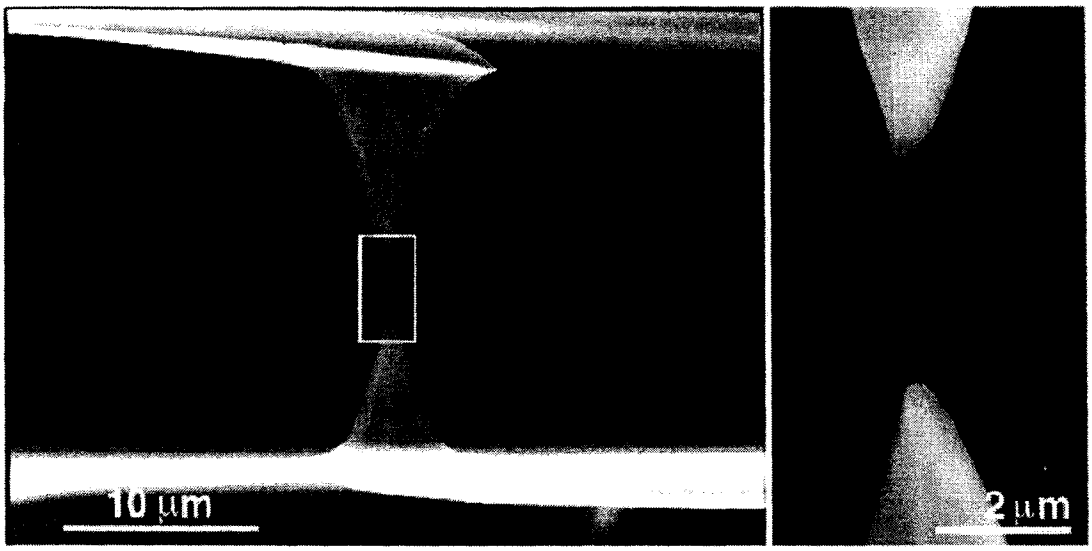

Fig. 1.4. Micrographs showing the apparatus for tensile loading of MWNTs [39] (Left) An SEM image of two AFM tips holding MWNTs, (Right) High magnification SEM image of the indicated region in left

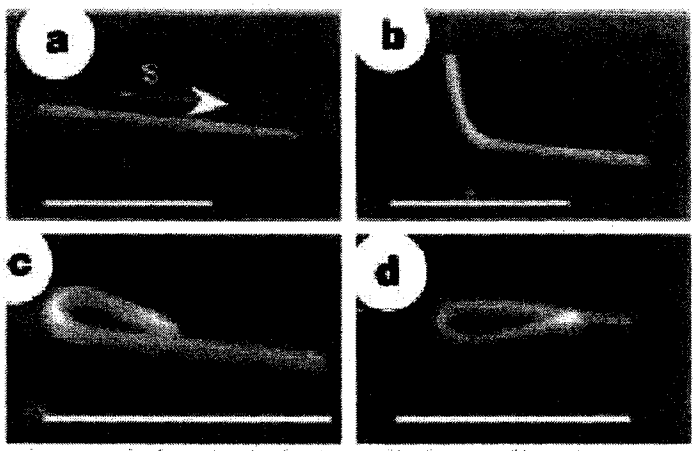

Fig. 1.5. Bending and buckling of CNT [42], (a) Original shape of CNT, (b) until it bends all the way back onto itself, (c) CNT is bent upwards all the way back onto itself, (d) The same CNT is bent all the way back the other way onto itself

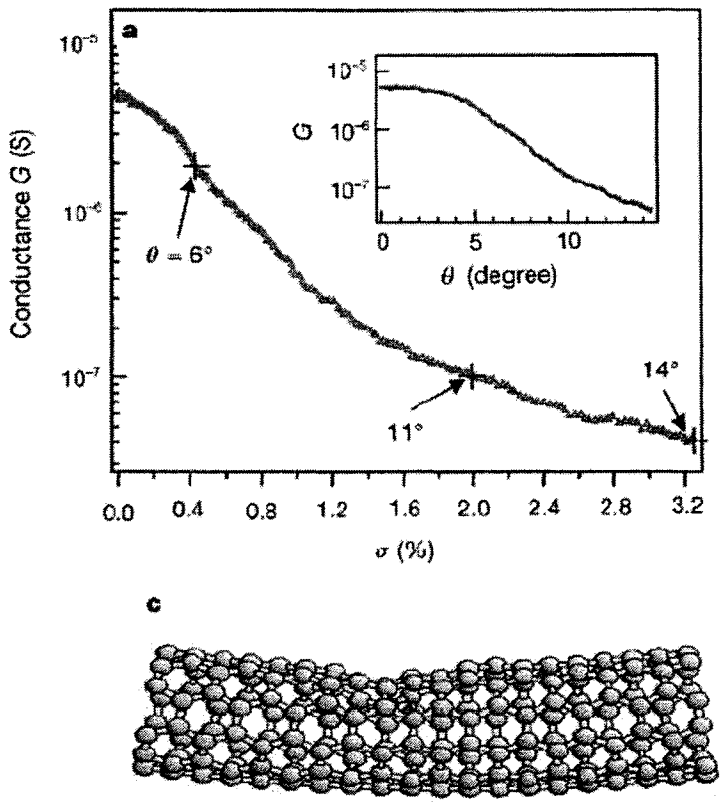

Fig. 1.6. Experimental result [50] of conductance (G) of the SWNT versus strain (σ) in the suspended part of the CNTs. (Inset) conductance (G) versus bending angle (θ)

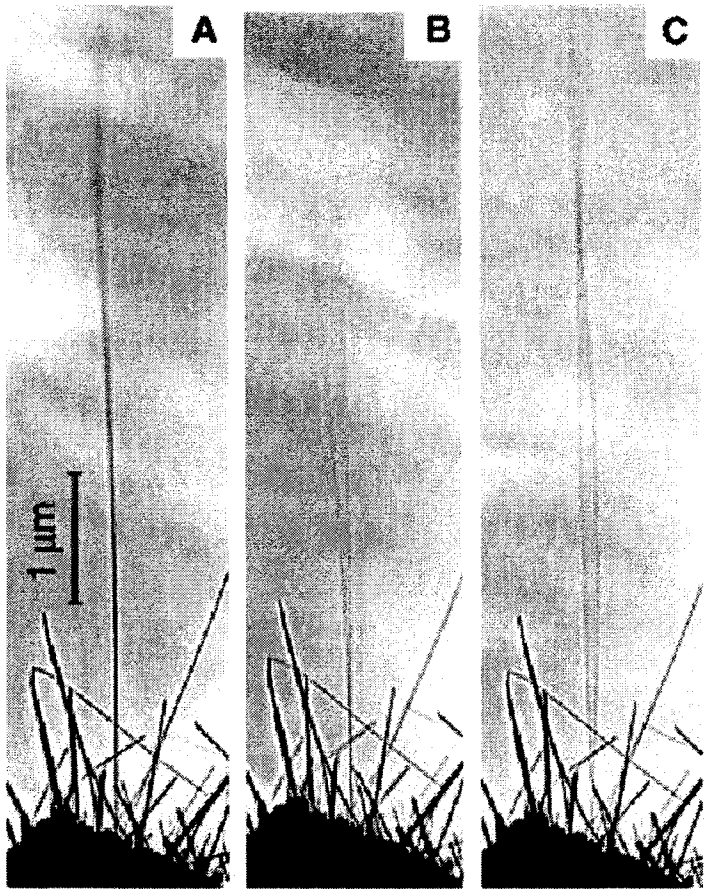

Fig. 1.7. CNT response to resonant alternating applied potential [55], (a) In the absence of potential, (b) fundamental mode of vibration (530KHz), (c) second mode of vibration (3.01MHz)

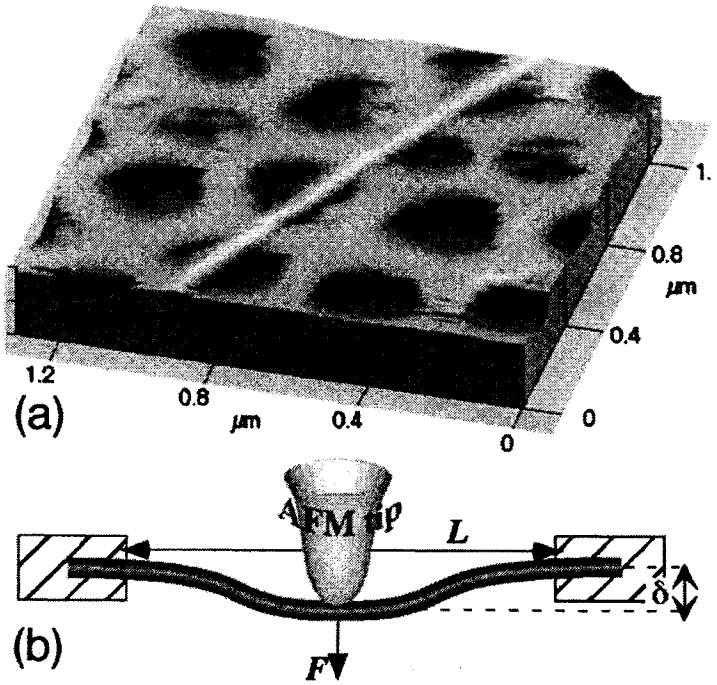

Fig. 1.8. (a) AFM image of a SWNT ropes adhered to the membrane. (b) Schematic of the measurement [58]

Chapter 2

Elastic Beam Models for Multiwall Carbon Nanotubes (MWNTs)

2.1 Introduction

CNTs are only a few nanometers in diameter, while as long as a few mm. Therefore, elastic beam model is ideal for the study of the overall mechanical deformation of CNTs. Many studies showed that the classic Euler-beam offers a simple and reliable model for overall mechanical deformation of CNTs provided the characteristic wavelength is much larger than the diameter of CNTs. Although CNTs can have diameters only several times larger than the length of a bond between carbon atoms (d=0.142nm), continuum elastic beam models [37, 38, 55, 64-78] have been effectively used to study static and dynamic structural behavior of CNTs, such as static deflection [38], column buckling [77], resonant frequencies and modes [37, 55], and sound wave propagation [78]. Since the elastic beam models enjoy very simple mathematical formulas, they have the potential to identify the key parameters affecting basic mechanical behavior of CNTs (and thus rule out other less important parameters), explain or predict new physical phenomena, and stimulate and guide further experiments and molecular dynamics simulations. This chapter studies systematically elastic beam models such as conventional

single-beam model, multiple-Euler-beam model, and multiple-Timoshenko-beam model.

2.2 Single-Beam Models

Static deflection: For a cantilever beam of length L under a concentrated force P at a point x=a measured from the fixed end, the deflection at any point between x=a and the free end x=L is [98]

$$y = \frac{Pa^2}{6EI}(3x - a), a \le x \le L \tag{2.1}$$

The $1/a^3$ dependency of P/y when x=a predicted by this formula has been confirmed by the experimental data for CNTs [38] (Fig. 2.1). As another example, the maximum deflection of a simple beam under a concentrated force P applied at its midspan is [98]

$$y = \frac{PL^3}{48EI} \tag{2.2}$$

where the number 48 becomes 192 for a clamped beam. This relation has been used [99] to estimate the Young's modulus of CNTs based on experimental data of the maximum deflection. The estimated value (E=0.81 TPa) is in good agreement with the values obtained by other methods. It is emphasized that the thickness of SWNTs in these studies has been taken as 0.34 nm and the

thickness of MWNTs has been calculated by the difference of the outermost radius R_{out} and the innermost radius R_{in}, and thus $I=\pi(R_{out}^4-R_{in}^4)/4$.

Column buckling: Dai et al. [15] used MWNTs as AFM tip and treated them as a hinged elastic column, and thus the maximum axial force MWNTs could sustain is estimated by the Euler force given by [98]

$$P=\frac{\pi^2 EI}{L^2} \tag{2.3}$$

Assuming E=1TPa, for example, these authors found that the Euler force for a 250nm-long, 5nm-diameter MWNT (treated as a column of solid circular cross-section) is about 5nN. The Euler force is also estimated by Yao & Lordi [100] for some other examples of CNTs. In particular, the Young's modulus of CNTs has been estimated by comparing the values of Euler force obtained by molecular dynamics simulations with those given by (2.3), see Garg et al. [77]. Their results confirmed that the Young's modulus estimated by such a comparison is around 1TPa, in satisfactory agreement with the values obtained by other methods.

Winkler-model: CNTs have been suggested as reinforcement fibers for super-strong composites [23-32]. Therefore, the role of surrounding elastic medium in mechanical behavior of embedded CNTs is a significant topic. A simplified model for the surrounding elastic medium is provided by the

Winkler-like model [101, 102] which assumes that interaction pressure acting on the embedded CNT per unit length is given by

$$p = -ky(x) \tag{2.4}$$

where y(x) is the deflection of the embedded CNT, k is a spring constant of the surrounding elastic medium which may depend not only on the Young's modulus of the surrounding elastic medium and the outermost diameter of the CNT, but also on the wavelength of the deformed CNT. The minus sign on the right-hand side indicates that the interaction pressure is opposite to the deflection. This simplest model has been used to study column buckling of embedded CNTs by Lourie et al. [23] and Ru [67], and vibration of embedded MWNTs by Yoon et al. [71].

Resonant frequencies: The n-order resonant (circular) frequency of a MWNT of length L, given by the single-beam model [37, 55, 79, 80, 91, 103], has the form

$$\omega_n = \lambda_n^2 \sqrt{\frac{EI}{\rho A}} = \frac{\lambda_n^2}{2} \sqrt{\frac{E(R_{out}^{\ 2} + R_{in}^{\ 2})}{\rho}} \tag{2.5}$$

where ρ is the mass density (per unit volume) of CNTs, I and A are the moment of inertia and the area of the cross-sectional of MWNT, and R_{out} and R_{in}, are the

outermost and the innermost radii. In addition, λ_n is a constant depending on the number n and end conditions. For instance, for fixed end conditions (that is, all nested individual tubes of the MWNT are clamped at both ends), $\lambda_1 L=4.73$, $\lambda_2 L=7.85$, $\lambda_3 L=10.996$. For cantilever end conditions, $\lambda_1 L=1.875$, $\lambda_2 L=4.694$, $\lambda_3 L=7.855$, see [79, 80]. If the CNT is embedded in an elastic medium characterized by the Winkler model (2.4), the n-order resonant (circular) frequency is [71, 79]

$$\omega_n = \sqrt{\frac{\lambda_n^4 EI + k}{\rho A}} \tag{2.6}$$

Prior experiments [37, 55, 91, 103] have convincingly shown that resonant frequencies of CNTs can be calculated by the formula (2.5). For example, for a CNT tested in [55], the experimental ratio ω_2/ω_1 is 5.68, in good agreement with the theoretical ratio 6.2 predicted by (2.5). In addition, the second-order vibrational mode was observed in [55], and the experimental value of a characteristic length is 0.76L, in good agreement with the theoretical value 0.8L (Fig. 1.7).

Sound wave speeds: It is well known that longitudinal and transverse sound wave speeds (phase velocity) in an elastic beam are [74]

$$v_L = \sqrt{\frac{E}{\rho}}, \qquad v_T = \left(\frac{EI\omega^2}{\rho A}\right)^{1/4} \tag{2.7}$$

In particular, the transverse speed v_T depends on both the frequency ω and the cross-sectional shape, while the longitudinal speed v_L depends on none of them. Popov et al. [78] have used these formulas to calculate sound speeds along CNTs. The value of Young's modulus of CNTs obtained by (2.7) based on a comparison with another method is about 1TPa, in good agreement with the known values. This indicates that the classic elastic beam formulas (2.7) can be applied to sound wave propagation in CNTs [78, 93, 94].

2.2 Multiple-Beam Models

Most of CNTs are MWNTs, which consist of arrays of SWNTs with an interlayer spacing of 0.34nm and each tube is coupled with its neighboring tubes through van der Waals interactions (Fig. 2.2). Therefore, Carbon MWNTs are different from traditional elastic beams due to their hollow multi-layer structure and the associated interlayer van der Waals forces. On one hand, it is known that friction between adjacent tubes in MWNTs is so low that the adjacent tubes could easily slide to each other [18, 104, 105]. On the other hand, although the van der Waals repulsive forces resist any reduction of interlayer spacing between adjacent tubes in MWNTs, it is not clear whether the magnitude of the repulsive forces in CNTs is so strong that the change in interlayer spacing in MWNTs can always be neglected even in some extreme cases. In spite of this, all previous beam models, such as those mentioned above, have ignored interlayer radial displacements in MWNTs and treated a MWNT

as a single-elastic beam. The previous work based on single-beam model [37, 55, 88, 90] assumes that all originally concentric tubes of a MWNT remain coaxial during deformation and thus can be described by a single deflection curve. In reality, however, individual tubes of a MWNT could deform individually with non-zero interlayer radial displacements, while their individual deformations are coupled through the interlayer van der Waals interaction.

2.3.1 Interlayer van der Waals Forces and the Interaction Coefficient

The van der Waals interaction energy potential, as a function of the interlayer spacing between two adjacent tubes, can be estimated by the Lennard-Jones model [106]. In view of the linearized analysis, the van der Waals interaction pressure at any given point between two adjacent tubes should be a linear function of the deflection jump at that point. On the other hand, because the resultant interaction pressure, or its energy potential, is defined per unit axial length, it should be proportional to the circumferential dimension (for instance, the inner radius) of the adjacent tubes.

Thus one can assume that the interaction energy potential per unit axial length between any two adjacent tubes is $2R_i g(\delta)$, where $g(\delta)$ is a universal function of the intertube spacing δ, and the R_i is the inner radius. Note that the radii of nanotubes are usually not smaller than 0.5nm [107], $g(\delta)$ can be well estimated by using the energy potential per unit area between two flat graphite

sheets, as given by Girifalco and Lad [106]. In doing so, the resultant interaction pressure (from both sides) between any two adjacent tubes of the inner radius R_i is given by

$$p = 2R_i \left.\frac{dg}{d\delta}\right|_{\delta=\delta_0} + c_i(\Delta w), \qquad c_i = 2R_i \left.\frac{d^2 g}{d\delta^2}\right|_{\delta=\delta_0}, \tag{2.8}$$

where δ_0 is the initial interlayer spacing, (Δw) is the deflection jump due to any deflection, and all higher order terms have been neglected because the present analysis is linearized in nature. For the present study, the initial interlayer spacing (about 0.34nm) is equal or very close to the equilibrium interlayer spacing at which $dg/d\delta=0$ [106], then the first term of Eq. (2.8) vanishes.

According to the data given in Girifalco and Lad [106], the coefficient of interaction pressure can be estimated

$$c_j = \frac{200(2R_j)erg/cm^2}{0.16d^2}, d = 0.142nm \tag{2.9}$$

where R_j is the radius of the j^{th} nanotube. A slightly different approximate value of the interaction coefficient can be obtained using the data given in a more recent work [108] for a specific group of DWNTs of very small radii, in which the curvature effect of CNTs is considered. According to the data given in Saito et al. [108], the coefficient of interaction pressure can be estimated (see Fig.

2.3)

$$c_j = \frac{320(2R_j)erg/cm^2}{0.16d^2}, d = 0.142nm \tag{2.10}$$

Throughout this dissertation, both interaction coefficients will be used. Evidently, a small difference in the interaction coefficient will not cause any significant consequences to the final results.

2.3.2 Multiple-Euler-Beam Model

The single-elastic beam model widely used in the literature [21, 37, 38, 55, 88, 90] assumes that all nested individual tubes of a MWNT remain coaxial during deformation and thus can be described by a single deflection curve. Such a model cannot be used to describe interlayer displacement of MWNTs. For this reason, a multiple-Euler-beam model has been developed in [67] to study column buckling of MWNTs embedded within an elastic medium and successfully used to study vibration [70, 71] of MWNTs and sound wave speeds [72] in MWNTs. In addition, unlike the single-elastic beam model [37, 55, 88, 90] which assumes that all originally concentric tubes of a MWNT remain exactly coaxial during vibration and thus can be described by a single deflection curve, the present analysis considers interlayer radial displacements within the MWNT and assumes that each individual tube of MWNTs has an individual deflection curve which is not necessarily coincident with the

deflection curves of other nested tubes of the MWNT. Thus, in a multiple-Euler-beam model, each of the nested, originally concentric nanotubes of a MWNT is described as an individual elastic Euler-beam, and the deflections of all nested tubes are coupled through the van der Waals interaction between any two adjacent tubes (Fig. 2.2). Since all nested tubes of a MWNT are originally concentric and the van der Waals interaction is determined by the interlayer spacing, the net van der Waals interaction pressure remains zero for each of the tubes provided they deform coaxially. Thus, for small-deflection linear problems, the interaction pressure at any point between any two adjacent tubes linearly depends on the difference of their deflections at that point. Thus, N nested tubes of an embedded N-wall CNT is described by the following N coupled equations [67, 70-72]

$$
\begin{aligned}
& c_1[w_2 - w_1] = EI_1 \frac{\partial^4 w_1}{\partial x^4} + \rho A_1 \frac{\partial^2 w_1}{\partial t^2}, \\
& c_2[w_3 - w_2] - c_1[w_2 - w_1] = EI_2 \frac{\partial^4 w_2}{\partial x^4} + \rho A_2 \frac{\partial^2 w_2}{\partial t^2}, \\
& \qquad \cdots\cdots\cdots\cdots\cdots\cdots\cdots\cdots \\
& \qquad \cdots\cdots\cdots\cdots\cdots\cdots\cdots\cdots \\
& p_m - c_{(N-1)}[w_N - w_{(N-1)}] = EI_N \frac{\partial^4 w_N}{\partial x^4} + \rho A_N \frac{\partial^2 w_N}{\partial t^2},
\end{aligned}
\tag{2.11}
$$

where x is the axial coordinate, t is time, $w_j(x, t)$ (j=1,2,...N) is the deflection of the j^{th} tube, I_j and A_j (j=1,2,...N) are the moment of inertia and the area of the cross-section, the subscripts 1, 2, ... N denote the quantities of the innermost

tube, its adjacent tube, and the outermost tube, respectively, and the two tubes have the same Young's modulus E and the mass density ρ per unit volume. The interaction coefficients c_j can be calculated by Eq (2.9) or (2.10). In addition, the pressure p_m per unit axial length, acting on the outermost tube due to the surrounding elastic medium, can be described by a Winkler-like model (Eq 2.4)

2.3.2 Multiple-Timoshenko-Beam Model

Many proposed applications and designs of CNTs, however, are involved with short CNTs of aspect ratio down to 10, or periodically supported CNTs with finite spans. For short CNTs, as will be shown Chapter 3, non-coaxial intertube vibration of MWNTs will be excited at ultrahigh frequencies at which the characteristic wavelength of vibrational modes is just a few times the outermost diameter of MWNTs. In this case, rotary inertia and shear deformation, which are ignored in the classical Euler-beam model, would become substantial for vibration of elastic beams when the characteristic wavelength is just a few times the diameter of their cross-section. For this reason, a multiple-Timoshenko-beam Model has been developed in [74] to study vibration of MWNTs. Thus, all nanotubes of MWNTs are modeled as a Timoshenko-beam, instead of classical Euler-beam. It is known that the total deflection w(x,t) of a Timoshenko-beam, and the slope φ(x, t) of the beam due to bending deformation alone are determined by the following two coupled equations [79, 109-111]

$$
\begin{aligned}
&-KAG\left(\frac{\partial\varphi}{\partial x}-\frac{\partial^2 w}{\partial x^2}\right)+p=\rho A\frac{\partial^2 w}{\partial t^2}\\
&EI\frac{\partial^2\varphi}{\partial x^2}-KAG\left(\varphi-\frac{\partial w}{\partial x}\right)=\rho I\frac{\partial^2\varphi}{\partial x^2}
\end{aligned}
\tag{2.12}
$$

where x is the axial coordinate, t is time, I and A are the moment of inertia and the area of the cross-section of the beam, p is the distributed pressure per unit axial length, E and G are Young's modulus and shear modulus, respectively, ρ is the mass density per unit volume, and K is the so-called shear coefficient which is about 0.6 ~ 0.7 for thin-walled circular cross-sections and 0.9 for solid circular cross-sections [110, 111].

Let us apply equations (2.12) to all tubes of a MWNT. Thus, multiple-Timoshenko-beam model of a N wall CNT, of length L and outer diameter d (Fig. 2.1), is described by the following equations

$$
\begin{aligned}
&-KA_1G\left(\frac{\partial\varphi_1}{\partial x}-\frac{\partial^2 w_1}{\partial x^2}\right)+c_1(w_2-w_1)=\rho A_1\frac{\partial^2 w_1}{\partial t^2}\\
&EI_1\frac{\partial^2\varphi_1}{\partial x^2}-KA_1G\left(\varphi_1-\frac{\partial w_1}{\partial x}\right)=\rho I_1\frac{\partial^2\varphi_1}{\partial t^2}\\
&-KA_2G\left(\frac{\partial\varphi_2}{\partial x}-\frac{\partial^2 w_2}{\partial x^2}\right)+c_2(w_3-w_2)-c_1(w_2-w_1)=\rho A_2\frac{\partial^2 w_2}{\partial t^2}\\
&EI_2\frac{\partial^2\varphi_2}{\partial x^2}-KA_2G\left(\varphi_2-\frac{\partial w_2}{\partial x}\right)=\rho I_2\frac{\partial^2\varphi_2}{\partial t^2}\\
&\qquad\cdots\cdots\cdots\cdots\cdots\cdots\cdots\cdots\cdots\cdots\\
&\qquad\cdots\cdots\cdots\cdots\cdots\cdots\cdots\cdots\cdots\cdots\\
&-KA_NG\left(\frac{\partial\varphi_N}{\partial x}-\frac{\partial^2 w_N}{\partial x^2}\right)-c_{(N-1)}(w_N-w_{(N-1)})=\rho A_N\frac{\partial^2 w_N}{\partial t^2}\\
&EI_N\frac{\partial^2\varphi_N}{\partial x^2}-KA_NG\left(\varphi_N-\frac{\partial w_N}{\partial x}\right)=\rho I_N\frac{\partial^2\varphi_N}{\partial t^2}
\end{aligned}
\tag{2.13}
$$

where $w_j(x, t)$ and $\varphi_j(x, t)$ (j=1,2,...N) are the total deflection and the slope due to bending of the j^{th} nanotube, I_j and A_j are the moment of inertia and the area of the cross-section of the j^{th} tube, here the 1, 2, ... N denote the quantities of the innermost tube, its adjacent tube, and the outermost tube, respectively, and the interaction coefficients c_j can be calculated by Eq (2.9) or (2.10).

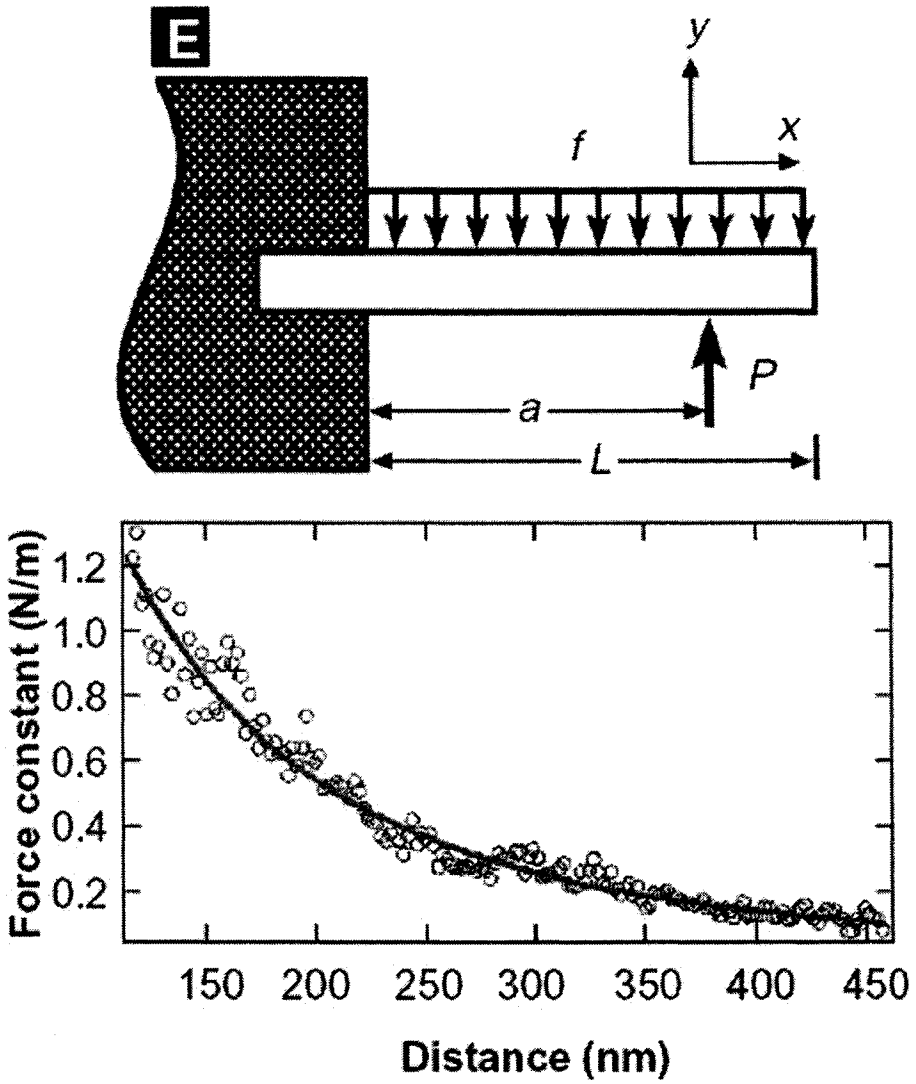

Fig. 2.1. (Top) Schematic of a cantilevered CNT with a free end. The CNT of length L is subjected to a point load P at x=a, (Bottom) The dependence of force constant (P/y) on position x (dot: experiment, solid line: results given by Euler-beam) [38]

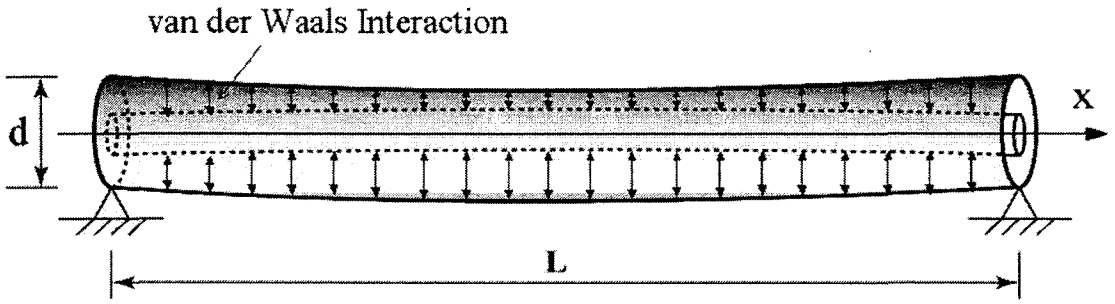

Fig. 2.2. Schematic of a MWNT under intertube van der Waals interaction.

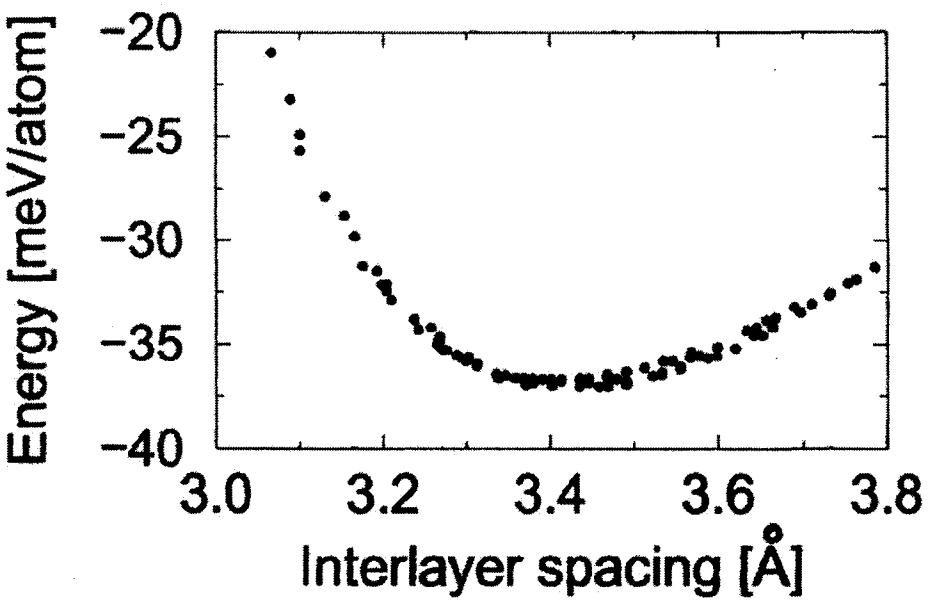

Fig. 2.3. The potential energy of the van der Waals potential per carbon atom plotted as a function of the interlayer spacing [108].

Chapter 3

Vibration of MWNTs Modeled as Euler-Beams

3.1 Introduction

The single-elastic beam model, which ignores non-coaxial intertube radial displacements and the related internal degrees of freedom, has been widely used to study static and dynamic behavior of MWNTs [21, 37, 38, 42, 55, 90, 112]. However, in many proposed designs of SWNT or MWNT-based electronics and nanodevices, CNT are often supported periodically [9-12, 19]. In some other applications, such as nanotweezers [17] and AFM tips[15, 20, 34], shorter CNTs are preferred to prevent undesirable kinking and buckling. Therefore, vibrational behavior of CNTs of smaller aspect ratios, or embedded in an elastic medium are of both practical and theoretical interest. In theses cases, it is anticipated that intertube radial displacements of MWNTs, which are completely ignored by the existing single-elastic beam model, would come to play a significant role and give rise to complicated intertube resonant frequencies and non-coaxial vibrational modes (defined by substantially non-coincident axes of the nested nanotubes). Although the intertube vibration would unlikely affect overall deflection of the outermost tube of MWNTs, it will inevitably cause internal non-coaxial deformation and distort the otherwise

concentric geometry of MWNTs. Especially, because each of the nested tubes of a MWNT could have different electronic properties than the others, non-coaxial distortion could significantly affect some important physical (electronic [113-120] and optical [121, 122]) properties of MWNTs. Hence, it is relevant to study when vibration of MWNTs becomes substantially non-coaxial. In this chapter, using a multiple-Euler-beam model, intertube vibration of MWNTs is presented with an emphasis on the role of van der Waals force.

3.2 Non-Coaxial Vibration of MWNTs

3.2.1 Resonant Frequencies and Vibrational Modes of a Double-Wall CNT (DWNT)

To clearly demonstrate essential concepts of non-coaxial vibration of MWNTs, let us first consider a DWNT [70, 108, 123, 124] of length L without surrounding medium (Fig 3.1). Applying Eq. (2.11) to each of the two concentric tubes, the multiple-beam model gives the equations for vibration of a DWNT as [70]

$$\begin{aligned} c[w_2 - w_1] &= EI_1 \frac{\partial^4 w_1}{\partial x^4} + \rho A_1 \frac{\partial^2 w_1}{\partial t^2}, \\ -c[w_2 - w_1] &= EI_2 \frac{\partial^4 w_2}{\partial x^4} + \rho A_2 \frac{\partial^2 w_2}{\partial t^2} \end{aligned} \tag{3.1}$$

where, Young's modulus E = 1TPa and the mass density ρ=1.3g/cm^3. (Here, it should be mentioned that a mass density ρ=1.3g/cm^3, based on a definition

[p724, [94]], has been used in Chapter 3 and 4 [70-72].) It is seen from (3.1) that vibration of the inner tube is coupled with vibration of the outer tube through the van der Waals interaction. Equation (3.1) is mathematically similar to the governing equations for vibration of an elastically connected double-beam system [125], or coupled harmonic oscillators [126, 127]. Here, let us consider the case in which the inner and outer nanotubes have the same end conditions. Thus, the inner and outer tubes share the same vibrational mode Y(x) determined by

$$\frac{d^4Y(x)}{dx^4} = \lambda^4 Y(x) \tag{3.2}$$

with the given end conditions. The value λ and the associated mode Y(x) are determined as the eigenvalue and associated eigenfunction of (3.2) with the given end conditions. For instance, for fixed end conditions, the first three eigenvalues of (3.2) are $\lambda_1 L=4.73$, $\lambda_2 L=7.85$, $\lambda_3 L=10.996$. For cantilever end conditions, $\lambda_1 L=1.875$, $\lambda_2 L=4.694$, $\lambda_3 L=7.855$ [79, 80]. Thus, for the n-order vibrational mode $Y_n(x)$ (n=1,2..., defined by the eigenfunction associated with the n-th eigenvalue of (3.2)), the frequency-equation can be obtained by substituting $w_1 = a_1 e^{i\omega t} Y_n(x)$, $w_2 = a_2 e^{i\omega t} Y_n(x)$ to (3.1), where a_1 and a_2 represent the amplitudes of the inner and the outer tubes, respectively, and ω is the (circular) frequency. It turns out that, in contrast to the only n-order resonance frequency (2.5) given by the single-beam model [37, 55, 91, 103], the multiple-beam model [70] predicts two n-order resonant (circular) frequencies as

$$\omega_{n1}^2 = \frac{1}{2}(\alpha_n - \sqrt{\alpha_n^2 - 4\beta_n}),$$
$$\omega_{n2}^2 = \frac{1}{2}(\alpha_n + \sqrt{\alpha_n^2 - 4\beta_n}), \tag{3.3}$$

where

$$\alpha_n = \frac{EI_1\lambda_n^4 + c}{\rho A_1} + \frac{EI_2\lambda_n^4 + c}{\rho A_2} > \sqrt{4\beta_n},$$
$$\beta_n = \frac{EI_1 EI_2 \lambda_n^8}{\rho^2 A_1 A_2} + c\lambda_n^4 \frac{EI_1 + EI_2}{\rho^2 A_1 A_2} \tag{3.4}$$

Here, the subscript 1 stands for the lowest (natural) n-order resonant frequency, in order to distinguish it from other n-order intertube resonant frequency characterized by substantially non-coaxial vibrational modes. For each of the resonant frequencies, the associated amplitude ratio of vibrational modes of the inner to the outer tubes is

$$\frac{a_1}{a_2} = 1 + \frac{EI_2\lambda_n^4}{c} + \frac{\rho\omega^2 A_2}{c} \tag{3.5}$$

Here, it should be stated that the present work is limited to infinitesimal vibration. Therefore, as usual, nonlinear large deflection effects are not taken into account.

♦ **Resonant Frequency of a Fixed CNT**

For a periodically supported MWNT, it is reasonable to assume that the deflection and the slope are zero at the supporters due to the symmetry. Thus, let us consider a fixed DWNT. For instance, assume that the inner and the outer diameters are 0.7 and 1.4 nm, respectively [70, 108, 123, 124]. Thus, the two n-order resonant frequencies given by Eq. (3.3), for n=1-5, are listed in Table 3-1 for several smaller aspect ratios.

		Mode (n)				
	L/D_{out}	1	2	3	4	5
ω_{n1}	10	14	38	72	106	141
	20	3.5	10	19	31	46
	50	0.6	1.6	3.1	5.1	7.5
ω_{n2}	10	103	107	123	162	225
	20	102	102	103	105	110
	50	102	102	102	102	102

Table 3.1 Resonant frequencies (10^{11} Hz) of a fixed DWNT (with the inner diameter 0.7 and the outer diameter 1.4nm)

It is found from Table 3.1 that:

1) The natural n-order resonant frequency ω_{n1} is always close to that given by the single-beam model (2.5), with a relative error less than 1% for n=1, and less than 25% for n=5.

2) The intertube n-order resonant frequency ω_{n2}, about 10 THz, is insensitive to the mode number n, and is much higher than the lowest natural frequency ω_{11} for larger aspect ratios. Therefore, the single-beam model is accurate for coaxial vibrations of DWNTs of larger aspect ratios at relatively lower frequencies, such as studied in [37, 55, 91, 103].

3) For shorter DWNT, however, the lowest non-coaxial resonant frequencies ω_{n2} are comparable to the first few higher natural frequencies.

For example, for aspect ratio 10 (for which the beam model is adequate), the first few intertube frequencies ω_{n2} (for n=1, 2, 3, 4 or 5) are around 10 THz, comparable to the 3rd-order natural frequency ω_{31}= 7.17 THz, and 4th-order natural frequency ω_{41}= 10.6 THz. In this case, the non-coaxial intertube resonant frequencies and the associated non-coaxial vibrational modes will be excited at the higher natural frequencies.

♦ **Resonant Frequency of a Cantilever CNT**

Shorter cantilever MWNTs are used in some nanodevices (such as nanotweezers and AFM tips [15, 17, 20, 34]. Here, the first few resonant frequencies of a shorter cantilever DWNT are listed in Table 3.2. It is seen from Tables 3.1 and 3.2 that all conclusions obtained for fixed DWNTs remain qualitatively true for cantilever DWNTs. In particular, the lowest intertube resonant frequencies are almost the same in the two cases, indicating that they are insensitive to the end conditions.

		Mode (n)				
	L/D_{out}	1	2	3	4	5
ω_{n1}	10	2	14	38	72	106
	20	0.6	3.5	10	19	31
	50	0.1	0.6	1.6	3.1	5.1
ω_{n2}	10	102	103	107	123	162
	20	102	102	102	103	105
	50	102	102	102	102	102

Table 3.2 Resonant frequencies (10^{11} Hz) of a cantilever DWNT (with the inner diameter 0.7 and the outer diameter 1.4nm)

♦ **Amplitude Ratio**

For both fixed and cantilever DWNTs, the amplitude ratio a_1/a_2 of the inner to the outer tubes for the natural frequency ω_{n1} is always close to unity, indicating that the associated vibrational modes are almost coaxial. On the other hand, the amplitude ratio a_1/a_2 for the intertube resonant frequency ω_{n2} is about –2, indicating that the deflection of the inner tube is opposite to the deflection of the outer tube and thus the associated vibrational mode will distort otherwise concentric geometry of DWNTs. Since the concentric structure is the geometrical characteristic of MWNTs, such a non-coaxial intertube vibration would crucially affect some of their important physical properties.

3.2.2 Resonant Frequencies and Vibrational Modes of a 5-Wall CNT

Further, let us consider a five-wall CNT with the innermost diameter 0.7 nm, and the outermost diameter 3.5nm. In this case, the equations (2.11) with N=5 lead to five coupled equations.

$$
\begin{aligned}
c_1[w_2 - w_1] &= EI_1 \frac{d^4 w_1}{dx^4} + \rho A_1 \frac{d^2 w_1}{dt^2}, \\
c_2[w_3 - w_2] - c_1[w_2 - w_1] &= EI_2 \frac{d^4 w_2}{dx^4} + \rho A_2 \frac{d^2 w_2}{dt^2}, \\
c_3[w_4 - w_3] - c_2[w_3 - w_2] &= EI_3 \frac{d^4 w_3}{dx^4} + \rho A_3 \frac{d^2 w_3}{dt^2}, \\
c_4[w_5 - w_4] - c_3[w_4 - w_3] &= EI_4 \frac{d^4 w_4}{dx^4} + \rho A_4 \frac{d^2 w_4}{dt^2}, \\
-c_4[w_5 - w_4] &= EI_5 \frac{d^4 w_5}{dx^4} + \rho A_5 \frac{d^2 w_5}{dt^2}
\end{aligned}
\qquad (3.6)
$$

For each of the vibrational modes $Y_n(x)$ (n=1,2...) determined by (3.2), the frequency-equation can be obtained by substituting $w_j = a_j e^{i\omega t} Y_n(x)$ (j=1,2,3,4,5) into (3.6). It turns out that, the 5-wall CNT has five resonance frequencies ω_{n1}(lowest) < ω_{n2} < ω_{n3} < ω_{n4} < ω_{n5}(highest), in contrast to the single resonance frequency given by the single-beam model (2.5).

For example, for fixed end conditions, all five resonant frequencies for n=1-5 are shown in Table 3.3.

		Mode (n)				
	L/D_{out}	1	2	3	4	5
ω_{n1}	10	4.9	13.4	25.5	38.9	50.5
	20	1.2	3.4	6.6	10.9	16.1
	50	0.2	0.5	1.1	1.8	2.6
ω_{n2}	10	53	54	57	65	80
	20	53	53	53	53	54
	50	53	53	53	53	53
ω_{n3}	10	90	91	93	97	106
	20	90	90	91	91	91
	50	90	90	90	90	90
ω_{n4}	10	122	122	123	127	133
	20	121	121	122	122	122
	50	121	121	121	121	121
ω_{n5}	10	145	145	147	150	157
	20	145	145	145	145	145
	50	145	145	145	145	145

Table 3.3 Resonant frequencies (10^{11} Hz) of a fixed DWNT (with the inner diameter 0.7 and the outer diameter 1.4nm)

It is seen that all results obtained for DWNTs remain qualitatively true for the 5-wall CNT, while the lowest intertube resonant frequency now decreases to

5.25 THz. Again, it confirms that the single-beam model is relevant to coaxial vibrations of MWNTs of larger aspect ratios at relatively lower frequencies [37, 55, 91], and non-coaxial vibrations occur only at much higher frequencies. Here, four non-coaxial intertube vibrational modes are shown in Fig.3.2. It is seen that the intertube vibration causes complex non-coaxial distortion of the MWNT. In particular, non-coaxial vibration could occur inside a MWNT even without significant deflection of the outermost tube. Of course, the jump of the deflection between any two adjacent tubes is bounded by the initial intertube spacing (about 0.34nm). This is not a problem for small deflection linear vibrations studied here.

3.3 The Effect of a Surrounding Elastic Medium on Vibration of MWNT

In many proposed applications and designs, however, CNTs are often embedded in another elastic medium [23, 25-27, 128, 129]. Therefore, vibrational behavior of CNTs of embedded in an elastic medium are of both practical and theoretical interest.

Transverse vibration of N nested tubes of an embedded N-wall CNT (Fig. 3-3) is described by the N coupled equations (2.11), where, Young's modulus E = 1TPa and the mass density ρ=1.3g/cm^3. In addition, the pressure p_m per unit axial length, acting on the outermost tube due to the surrounding elastic medium, can be described by a Winkler-like model (2.4), and k is a

constant determined by the material constants of the elastic medium, the outermost diameter of the embedded MWNT, and the wavelength of vibrational modes. It is known [101, 130] that the simple model (2.4) is especially relevant if the constant k is allowed to be dependent on the wavelength. For example, for an elastic medium (such as polymers) of a Young's modulus of 2GPa [23], the dependency of k on the mode number n (defined later) is shown in Fig. 3.4. ([101], Eqs. (53, 54)). For the present analysis, the parameter ($n\pi d/2L$) is between 0.03 and 0.5. It is seen that the constant k almost linearly increases with the mode number n in this range. On the other hand, because k is proportional to the Young's modulus of the surrounding elastic medium, the value of k for other Young's modulus can be easily obtained from Fig. 3.4. Finally, it should be stated that the model (2.4) can be employed to describe not only a MWNT embedded in an elastic medium, but also a MWNT embedded within an elastic thin film, or within a CNT-sheet, or within a CNT-rope. Therefore, vibration of MWNTs held by an elastic constraint described by (2.4) is of great practical and theoretical interest.

3.3.1 Resonant Frequencies and Vibrational Modes of a DWNT

To clearly demonstrate essential ideas of intertube vibration of an embedded MWNT, let us first consider a DWNT of length L, as shown in Fig. 3.3. For a DWNT, the equations are given by (2.11) with N=2 as follows

$$c_1[w_2 - w_1] = EI_1 \frac{d^4 w_1}{dx^4} + \rho A_1 \frac{d^2 w_1}{dt^2},$$
$$-kw_2 - c_1[w_2 - w_1] = EI_2 \frac{d^4 w_2}{dx^4} + \rho A_2 \frac{d^2 w_2}{dt^2} \tag{3.7}$$

The two n-order resonant frequencies and the associated amplitude ratio of the inner to the outer tubes are given by

$$\omega_{n1}^2 = \frac{1}{2}(\alpha_n - \sqrt{\alpha_n^2 - 4\beta_n}),$$
$$\omega_{n2}^2 = \frac{1}{2}(\alpha_n + \sqrt{\alpha_n^2 - 4\beta_n}), \tag{3.8}$$
$$\frac{a_1}{a_2} = 1 + \frac{EI_2\lambda_n^4}{c_1} - \frac{\rho\omega^2 A_2}{c_1} + \frac{k}{c_1}$$

where

$$\alpha_n = \frac{EI_1\lambda_n^4 + c_1}{\rho A_1} + \frac{EI_2\lambda_n^4 + c_1 + k}{\rho A_2} > \sqrt{4\beta_n},$$
$$\beta_n = \frac{EI_1 EI_2 \lambda_n^8}{\rho^2 A_1 A_2} + c_1\lambda_n^4 \frac{EI_1 + EI_2}{\rho^2 A_1 A_2} + k\frac{EI_1\lambda_n^4 + c_1}{\rho^2 A_1 A_2} \tag{3.9}$$

Here, ω_{n1} is the lower n-order resonant frequency and ω_{n2} is the higher n-order resonant frequency, and the spring constant k may depend on the mode number n.

For the sake of comparison, the n-order resonant frequency of a MWNT, embedded in an elastic medium characterized by the spring constant k, given by

the single-beam model (2.6) is denoted by

$$\omega_{n0}^2 \equiv \omega_n^2 = \frac{\lambda_n^4 EI + k}{(\rho A)} \tag{3.10}$$

where I and A are the total moment of inertia and the total cross-sectional area of MWNT. Thus, $I=I_1+I_2$ and $A=A_1+A_2$ for a DWNT.

If the parameter c_1 is so large that

$$\frac{c_1}{\lambda_n^4 EI} >> 1, \qquad \frac{c_1}{k} >> 1 \tag{3.11}$$

it can be verified that the jump of the deflections between any two adjacent tubes is negligible, and thus the lower n-order resonant frequency ω_{n1} given by (3.8) reduces to (3.10) given by the single-elastic beam model. In this case, the higher n-order intertube resonant frequency ω_{n2} given by (3.10) reduces to

$$\omega_{n2}^2 \approx \frac{c_1(A_1 + A_2)}{\rho A_1 A_2} \tag{3.12}$$

For example, for a fixed DWNT with the inner diameter 0.7 nm and the outer diameter d=1.4 nm [70, 108, 123, 124], the two resonant frequencies ω_{nj} given by (3.8) for n=1, 2, 3 and j=1,2 are shown in Fig. 3.5. for different aspect ratios, mode number n, and spring constant k. Similar results for a cantilever DWNT are given in Fig. 3.6. It is found that

1) When the spring constant k is smaller than the interaction coefficient c_1 (such as a polymer medium [23]), the lower n-order resonant frequency ω_{n1} given by (3.8) is close to the natural frequency ω_{n0} given by the single-beam model (3.10). The relative error is less than 2% for n=1, and less than 10% for n=3. In this case, the lower resonant frequencies ω_{n1} can be estimated by the single-beam model (3.10).

2) However, as the ratio k/c_1 is bigger than unity and approaches 100, the lower resonant frequency ω_{n1} tends to 6.6 THz for n=1, to 7 THz for n=2, and to 8.1 THz for n=3 with the fixed end condition, and to 6.56 THz for n=1, to 6.61 THz for n=2, and to 7 THz for n=3 with the cantilever end condition. In these cases, the lower resonant frequency ω_{n1} is almost one order of magnitude lower than the frequency ω_{n0} given by the single-beam model. Therefore, the single-beam model fails to predict the lower n-order resonant frequency.

3) When the spring constant k is much lower than the interaction coefficient c_1 (say, $k/c_1 < 0.1$), the higher n-order intertube resonant frequency ω_{n2} (for n=1,2,3) is insensitive to the mode number, the aspect ratio, and the end condition. The intertube resonant frequency ω_{n2} is always above 1 THz, and thus much higher than the lowest resonant frequency ω_{11} for large aspect ratios (say $L/d \geq 50$). However, for smaller aspect ratios (say L/d=10, see [15, 17] for application of MWNTs of small aspect ratio, and [20] for recent progress in MWNTs of small aspect ratio as AFM tip), the first few intertube resonant frequencies ω_{n2} are comparable to the 3-order resonant frequency ω_{31} and the 3-order natural frequency ω_{30} given by the single-beam model (3.10). For

example, for a fixed DWNT of aspect ratio 10 and $k/c_1 = 0.001$, the first three intertube resonant frequencies ω_{n2} (n=1,2,3) are 8.1 THz, 8.7 THz, and 11 THz, comparable to the 3-order natural frequency ω_{30}= 6.9 THz.

4) However, as the ratio k/c_1 is larger than unity and approaches 100, the higher n-order intertube resonant frequency ω_{n2} rapidly goes up. The ratio ω_{n2}/ω_{n0} converges to 1.23 (n=1,2,3). In this case, the frequency given by the single-beam model (3.10) is close to the higher n-order resonant frequency ω_{n2}, rather than the lower one ω_{n1}. This is due to the fact that the intertube interaction is much weaker than the constraint of the surrounding elastic medium.

5) When the spring constant k is much lower than the interaction coefficient c_1 (say, $k/c_1 < 0.1$), the amplitude ratio a_1/a_2 of the inner to the outer tubes for the lower n-order resonant frequency ω_{n1} is found to be very close to unity, which indicates that the associated resonant mode is almost coaxial and close to that given by the single-beam model. However, as the ratio k/c_1 increases, the amplitude ratio a_1/a_2 for the lower n-order resonant frequency ω_{n1} is no longer close to unity. On the other hand, when the spring constant k is much smaller than c_1, the amplitude ratio a_1/a_2 for the higher n-order intertube resonant frequency ω_{n2} is found to be always negative, which indicates that the deflection of the inner tube is opposite to the deflection of the outer tube, and thus the associated intertube resonant mode is substantially non-coaxial. As the ratio k/c_1 increases, the amplitude ratio a_1/a_2 for the higher n-order intertube resonant frequency ω_{n2} goes to zero. For instance, for a fixed DWNT of aspect ratio 10 and $k/c_1 = 100$, a_1/a_2 is about –0.02. This implies that the amplitude of

the outer tube is much bigger than the amplitude of the inner tube, because the intertube interaction is so weak that the inner tube is almost disconnected from the outer tube.

3.3.2 Resonant Frequencies and Vibrational Modes of a 5-wall CNT

Further, let us consider a 5-wall CNT with the innermost diameter 0.7 and the outermost diameter D_{out} = 3.5nm. Thus, the 5-wall CNT has five resonance frequencies ω_{n1}(lowest) < ω_{n2} < ω_{n3} < ω_{n4} < ω_{n5}(highest), in similar to two different resonance frequencies of the DWNT. The five n-order resonant frequencies ω_{nj} for n=1, 2, 3 and j=1,2,..,5 are shown in Fig. 3.7-3.10 for different aspect ratios, end conditions, mode number n, and spring constant k. It is found that

1) When the spring constant k is much smaller than the interaction coefficient c_4 (say, $k/c_4 < 0.1$), the lowest n-order resonant frequency ω_{n1} is close to that given by the single-beam model (3.10). This relative error is less than 4% for n=1, and less than 9% for n=3. In this case, the lowest n-order resonant frequency ω_{n1} can be estimated satisfactorily by the single-beam model (3.10).

2) However, as k/c_4 increases and approaches 100, the lowest n-order resonant frequency ω_{n1} tends to 2.93 THz for n=1, to 3.03 THz for n=2, and to 3.31 THz for n=3 with the fixed end condition, and to 2.92 THz for n=1, to 2.93 THz for n=2, and to 3.03 THz for n=3 with the cantilever end condition. In particular, the lowest resonant frequency ω_{n1} is about one order of magnitude smaller than

the frequency ω_{n0} given by the single-beam model (3.10).

3) When the spring constant k is much smaller than the interaction coefficient c_4 (say, $k/c_4 < 0.1$), the highest n-order intertube resonant frequency ω_{n5} is always above 10 THz, and thus much higher than the lowest n-order resonant frequency ω_{n1}. However, as k/c_4 increases and approaches 100, the ratio of the highest n-order intertube frequency ω_{n5} to the frequency ω_{n0} given by single-beam model tends to 1.74 (for n=1,2,3). It is anticipated that the number 1.74 is determined by the number of the nested tubes and their radii.

4) When the spring constant k is much smaller than the interaction coefficient c_4 (say, $k/c_4 < 0.1$), the amplitude ratio a_j/a_5 (j=1,2,3,4) of the inner to the outermost tubes for the lowest n-order resonant frequency ω_{n1} is found to be very close to unity, which indicates that the associated resonant mode is almost coaxial, see Figs. 3.11. and 3.12. However, as the ratio k/c_4 increases, the amplitude ratios a_1/a_5, a_2/a_5, a_3/a_5, and a_4/a_5 for the lowest n-order resonant frequency ω_{n1} are no longer close to unity. For instance, for a fixed 5-wall CNT of aspect ratio 10 and $k/c_4 = 1$, a_1/a_5, a_2/a_5, a_3/a_5, and a_4/a_5 are 3.87, 3.36, 2.66, and 1.84, respectively, see Figs. 3.13 and 3.14. This means that the deflections of the five tubes are no longer coaxial, although they are of the same sign.

5) On the other hand, the amplitude ratios for the higher n-order intertube resonant frequencies ω_{n2}, ω_{n3}, ω_{n4}, and ω_{n5}, are found to have different signs, which indicates that the deflections of the some tube are opposite to the deflections of the others, and thus the associated vibrational mode is substantially non-coaxial, see Figs. 3.11-3.14. Clearly, such non-coaxial

vibrational modes will inevitably distort concentric internal structure of MWNTs, and thus significantly alter some of their important physical properties.

3.4 Summary

Internal vibration of MWNTs is studied using the multiple-Euler-beam model, which considers the intertube radial displacements and the associated internal degrees of freedom of MWNTs. The first few non-coaxial resonant frequencies are found to be insensitive to vibrational modes, length of MWNTs, and the end conditions, while they decrease with the number of nested layers. When the surrounding elastic medium is very compliant (such as polymers), the lowest resonant frequency predicted by the present model is almost coincident with the lowest natural frequency given by the existing single-beam model, while other new intertube resonant frequencies predicted by the present model are much higher than the lowest natural frequency given by the single-beam model. For smaller aspect ratios and radii, these non-coaxial intertube resonant frequencies are found to be comparable to the first few higher natural frequencies given by the single-beam model. This implies that internal non-coaxial resonance will be excited at the higher natural frequencies, and thus MWNTs cannot maintain their concentric structure at ultrahigh frequencies. As a result, non-coaxial intertube vibration will distort the otherwise concentric geometry of MWNTs, and thus crucially alter some of their important physical properties. In particular, because the first few intertube resonant frequencies fall into a very narrow range, their non-coaxial vibrational modes would be excited

simultaneously. These results predicted by a simple linear multiple-Euler-beam model [70, 71] are found to well agree with recent molecular simulations [95, 96] on non-coaxial vibration of MWNTs. Non-coaxial vibration is clearly observed by their molecular structural mechanics simulation (Fig. 3.15, (e)).

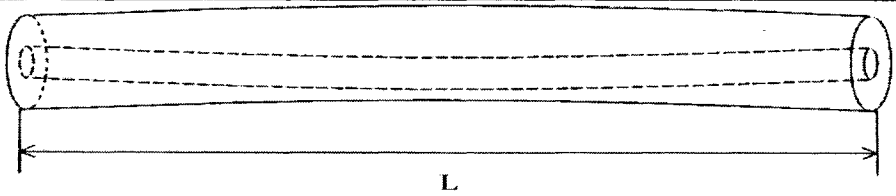

Fig. 3.1. Non-coaxial vibration of a DWNT

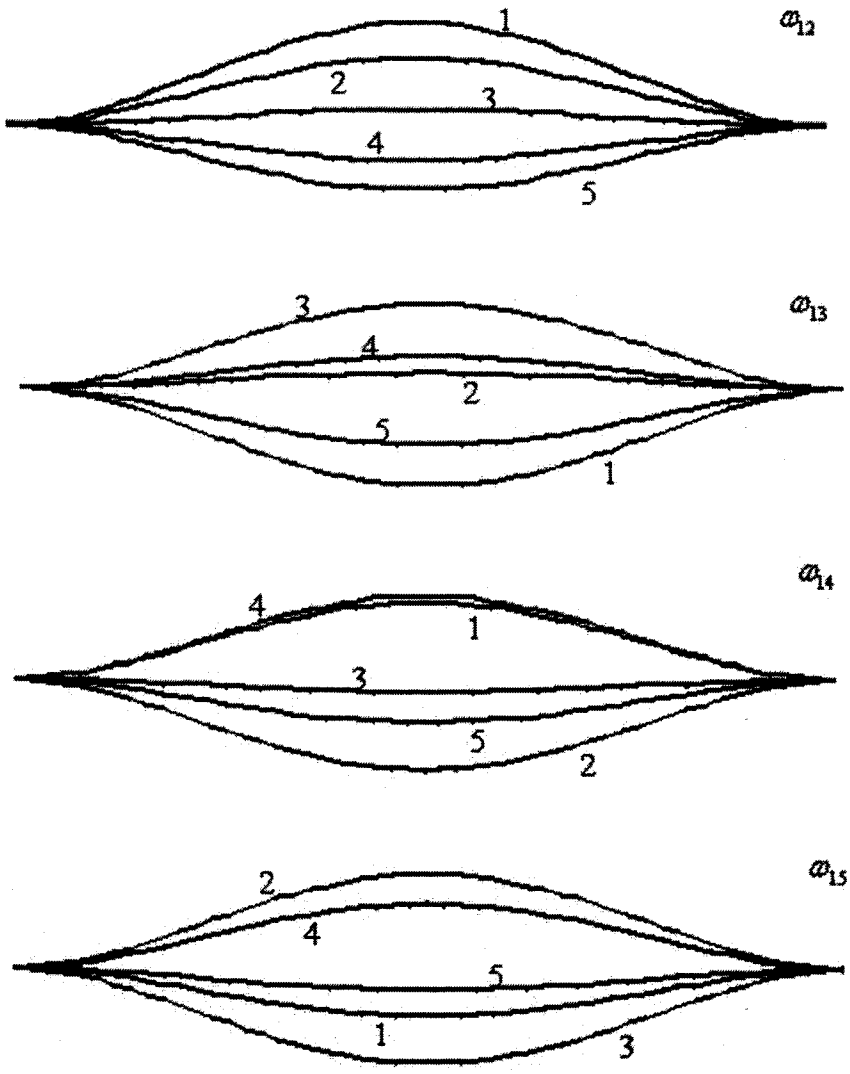

Fig 3.2. Four non-coaxial intertube vibrational modes of a fixed 5-wall CNT

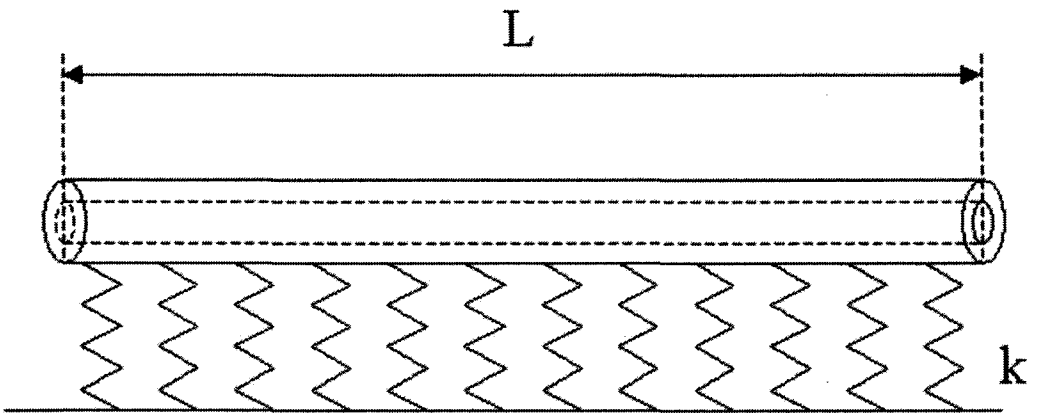

Fig. 3.3. Vibration of a MWNT embedded within an elastic medium characterized by a spring constant k.

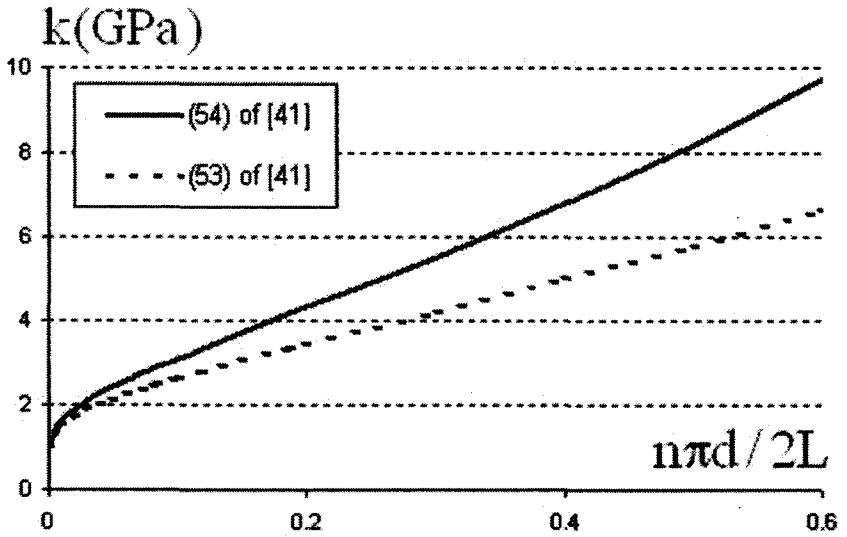

Fig. 3.4. Dependency of the spring constant k on the parameter (nπd/2L) (with Young's modulus E = 2GPa, Poisson ratio ν = 0.35, d = the outermost diameter, n = mode number).

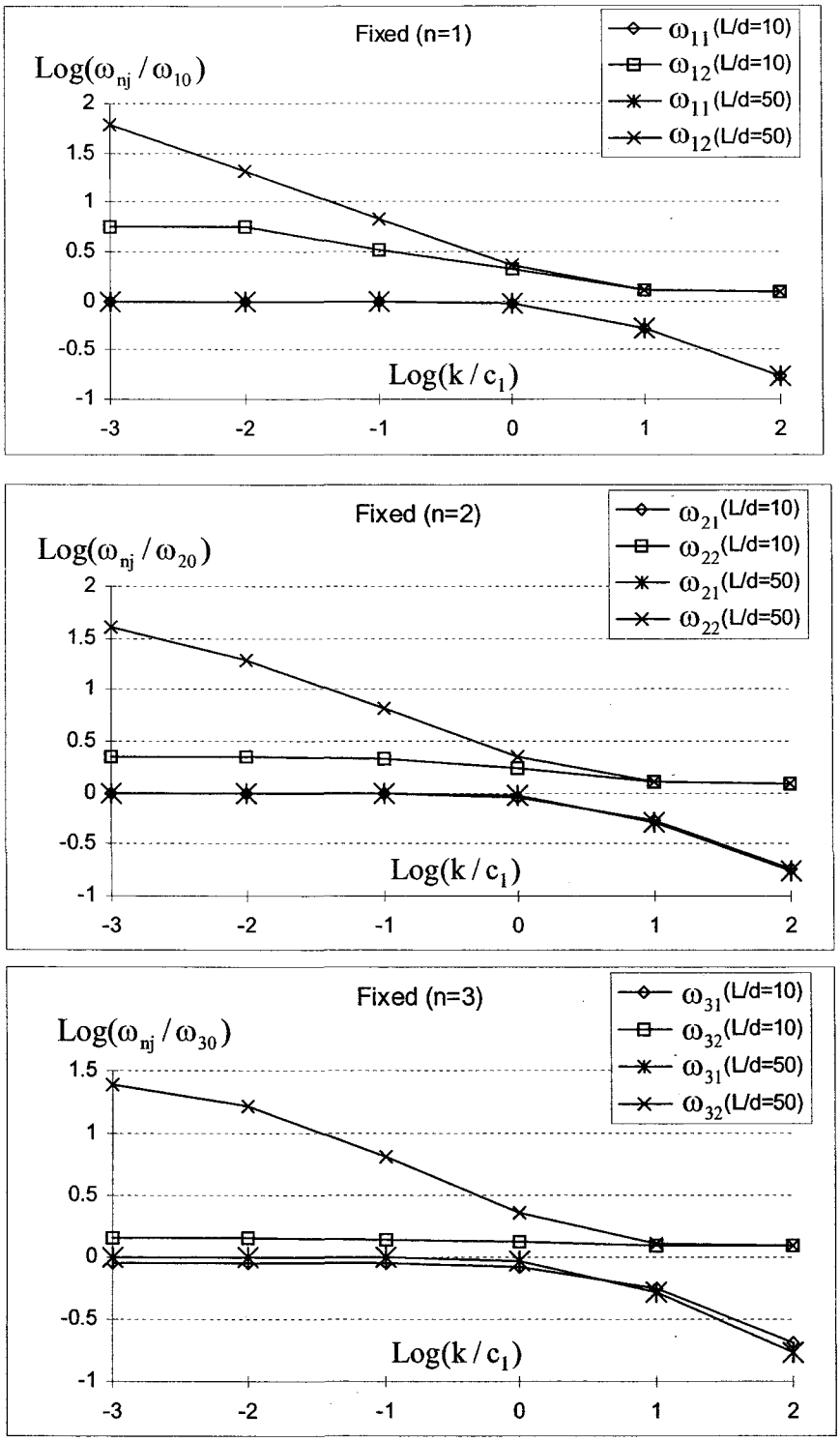

Fig. 3.5. DWNT frequencies against the spring constant k for fixed end condition (with the inner diameter 0.7 nm and the outer diameter 1.4 nm).

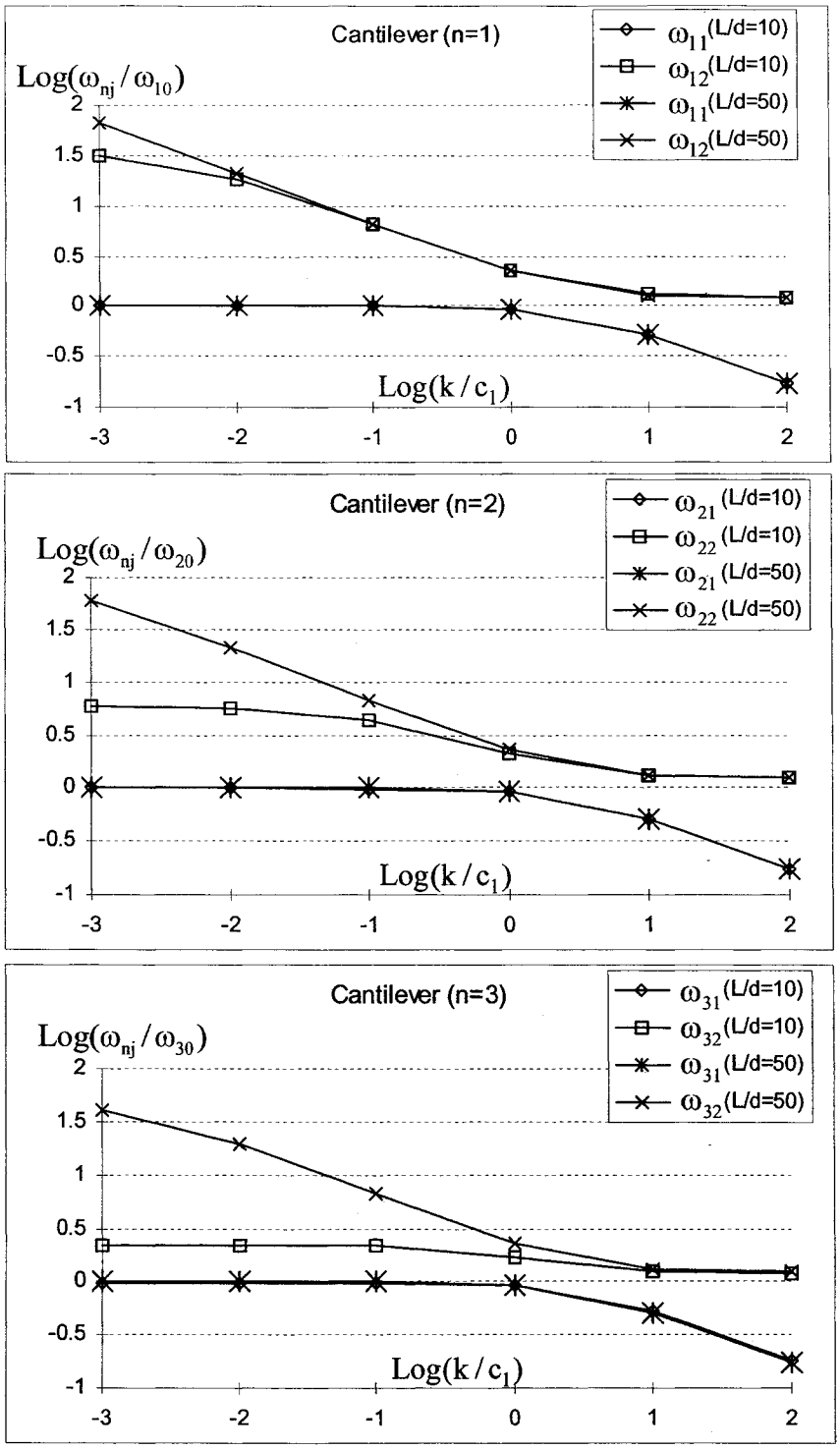

Fig. 3.6. DWNT frequencies against the spring constant k for cantilever end condition (with the inner diameter 0.7 nm and the outer diameter 1.4 nm).

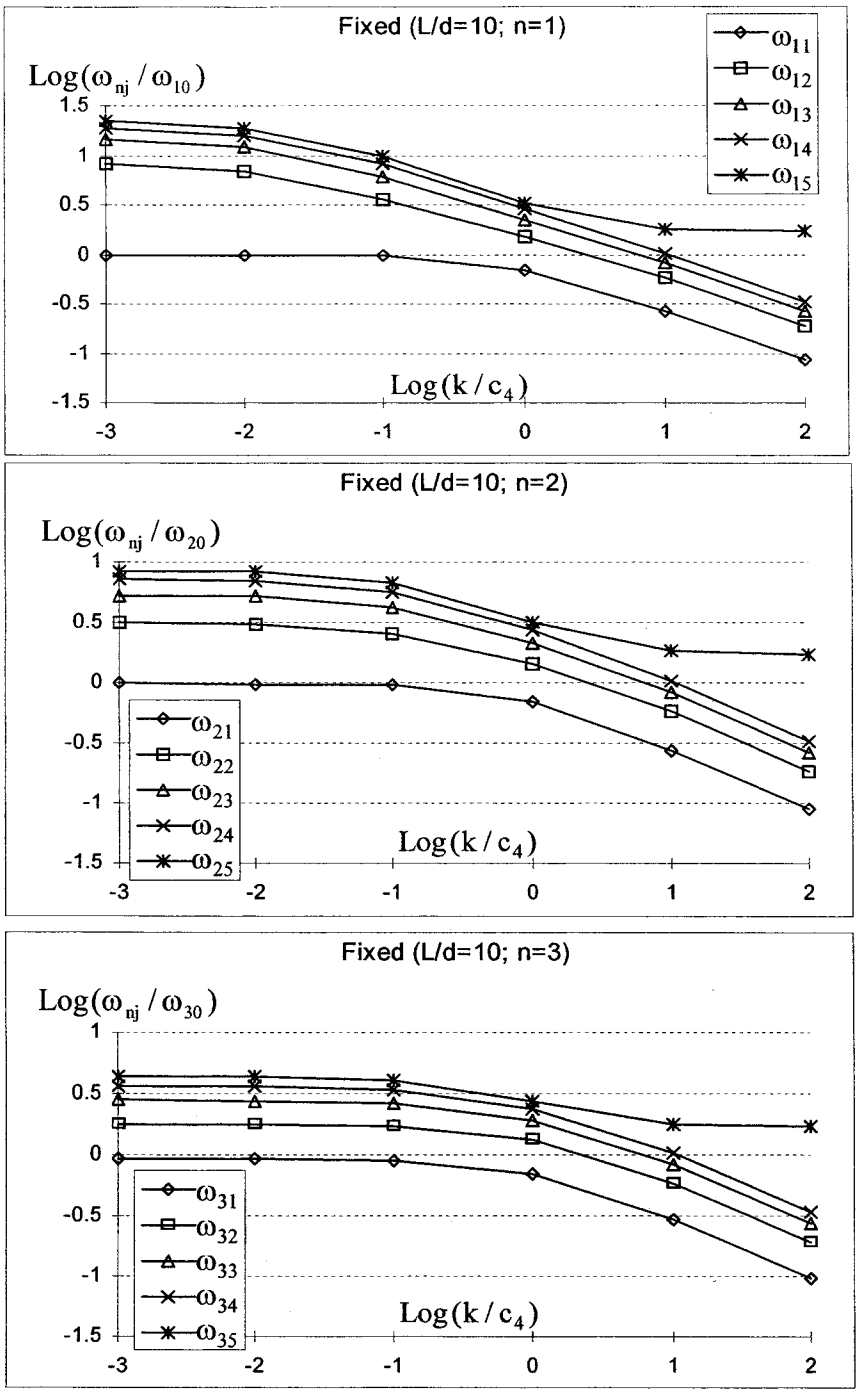

Fig. 3.7. 5-wall CNT frequencies against the spring constant k for fixed end condition (with the innermost diameter 0.7 nm and the outermost diameter 3.5 nm, and L/d = 10).

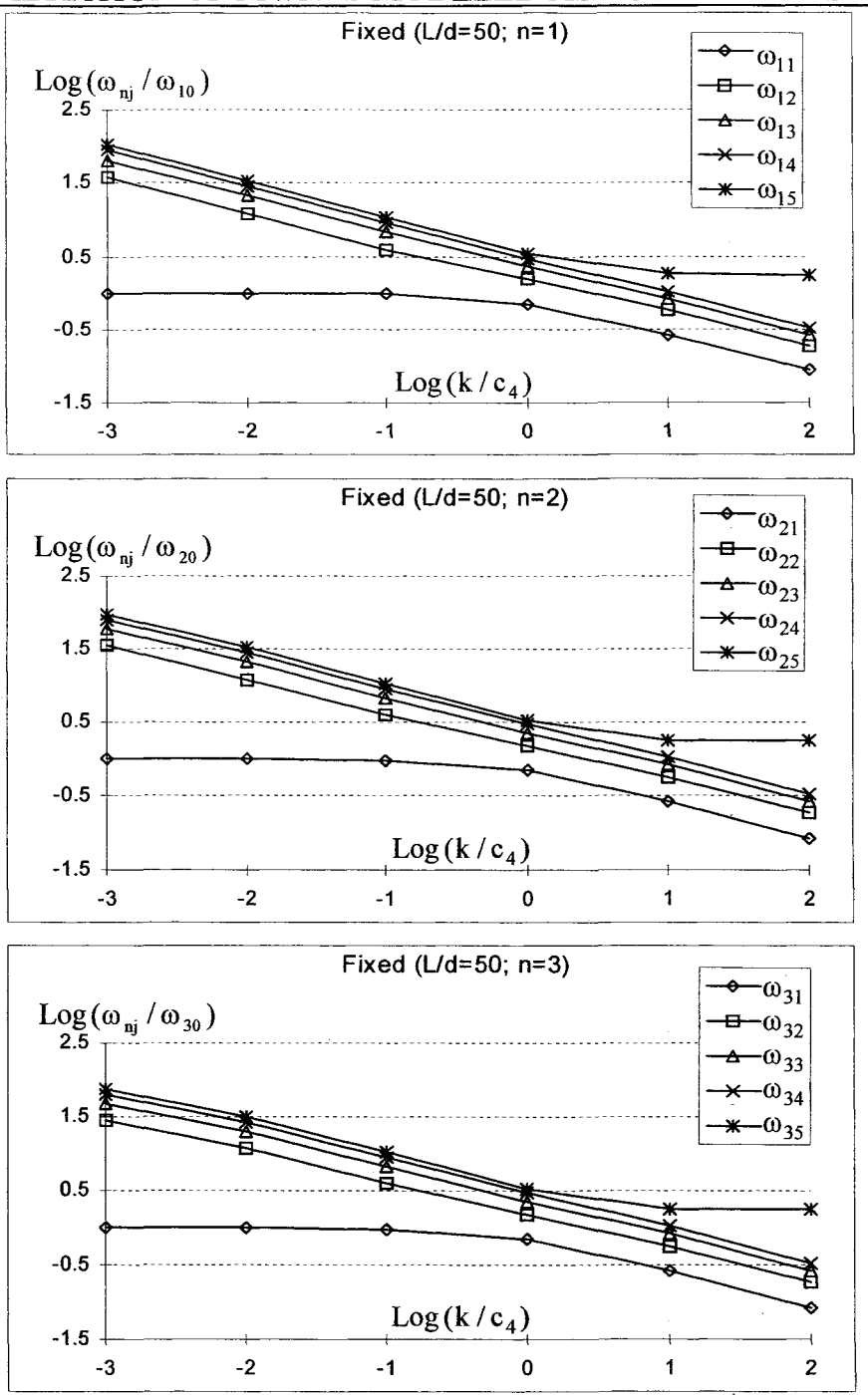

Fig. 3.8. 5-wall CNT frequencies against the spring constant k for fixed end condition (with the innermost diameter 0.7 nm and the outermost diameter 3.5 nm, and L/d = 50).

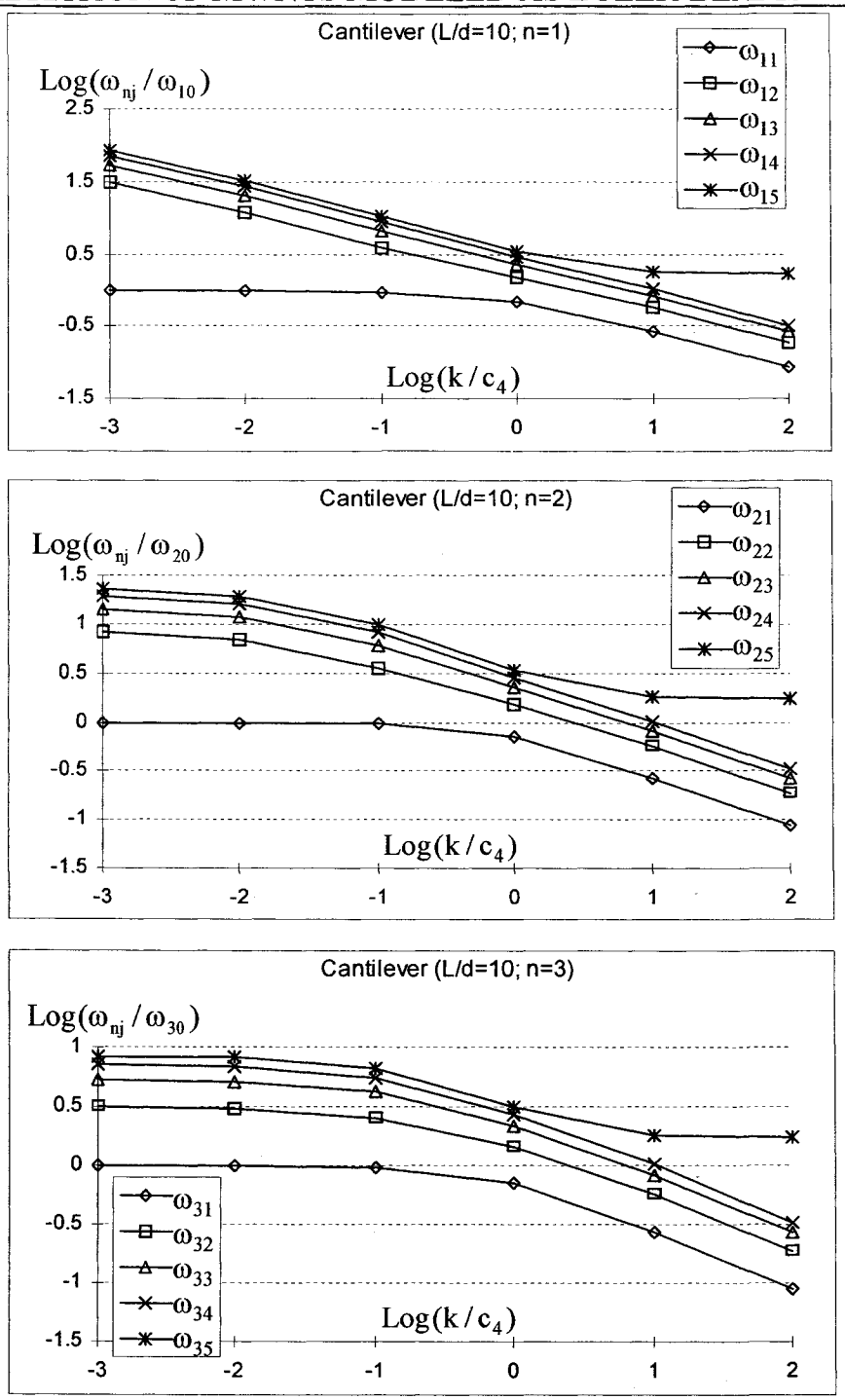

Fig. 3.9. 5-wall CNT frequencies against the spring constant k for cantilever end condition (with the innermost diameter 0.7 nm and the outermost diameter 3.5 nm, and L/d = 10).

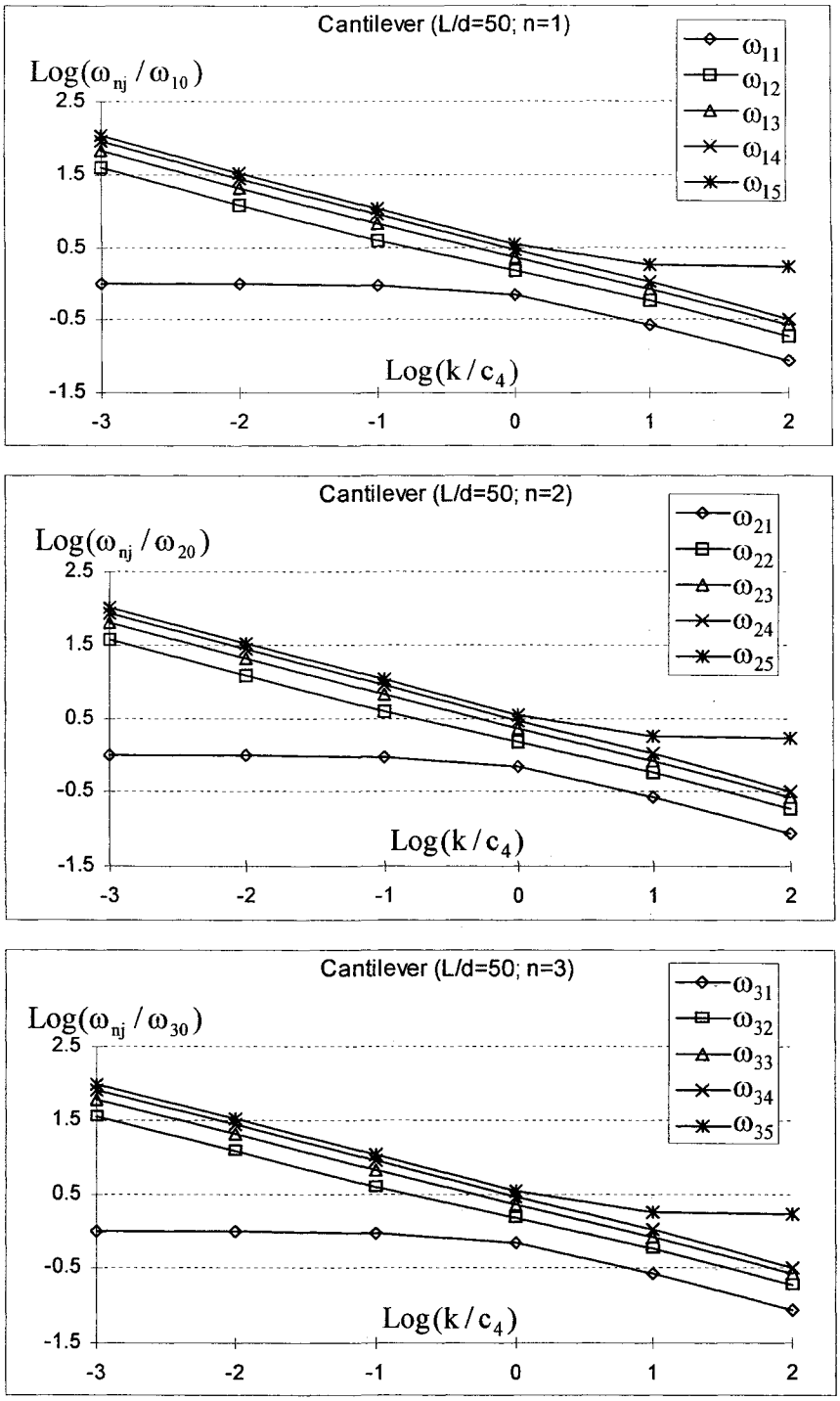

Fig. 3.10. 5-wall CNT frequencies against the spring constant k for cantilever end condition (with the innermost diameter 0.7 nm and the outermost diameter 3.5 nm, and L/d = 50).

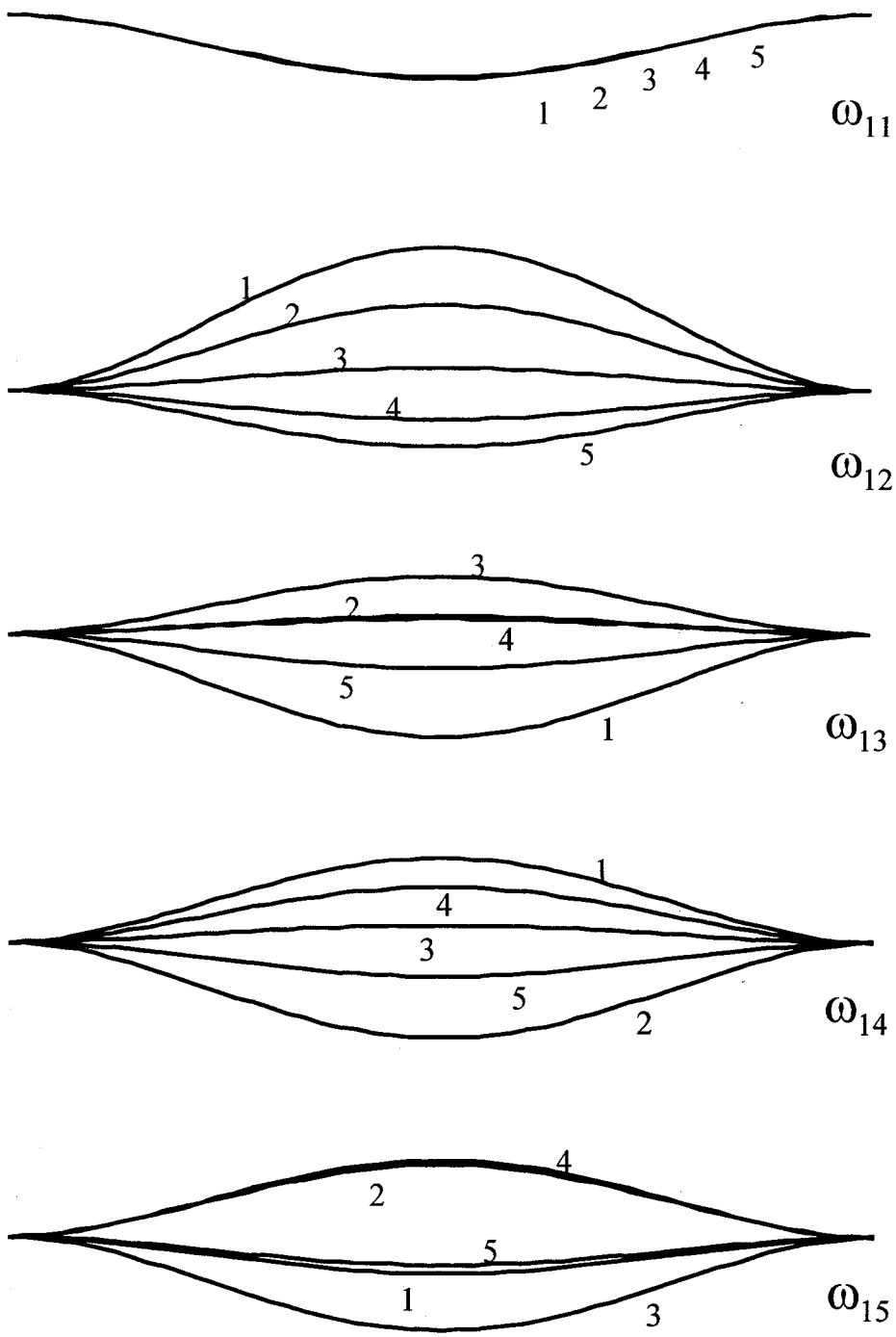

Fig. 3.11. Five intertube vibrational modes of a fixed 5-wall CNT. (with L/d = 10, $k/c_4 = 0.001$, and n=1).

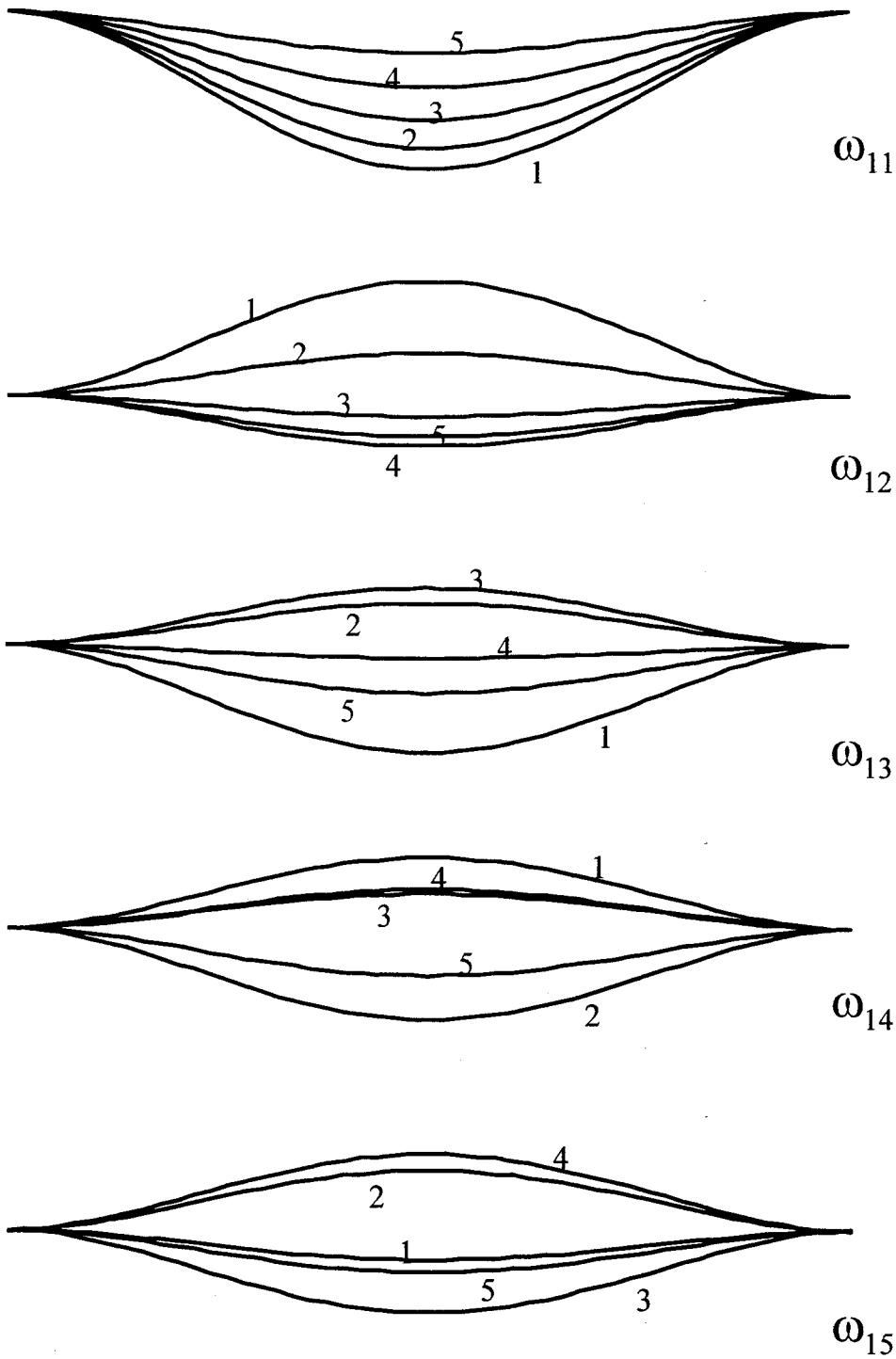

Fig. 3.12. Five intertube vibrational modes of a fixed 5-wall CNT. (with L/d = 10, $k/c_4 = 1$, and n=1).

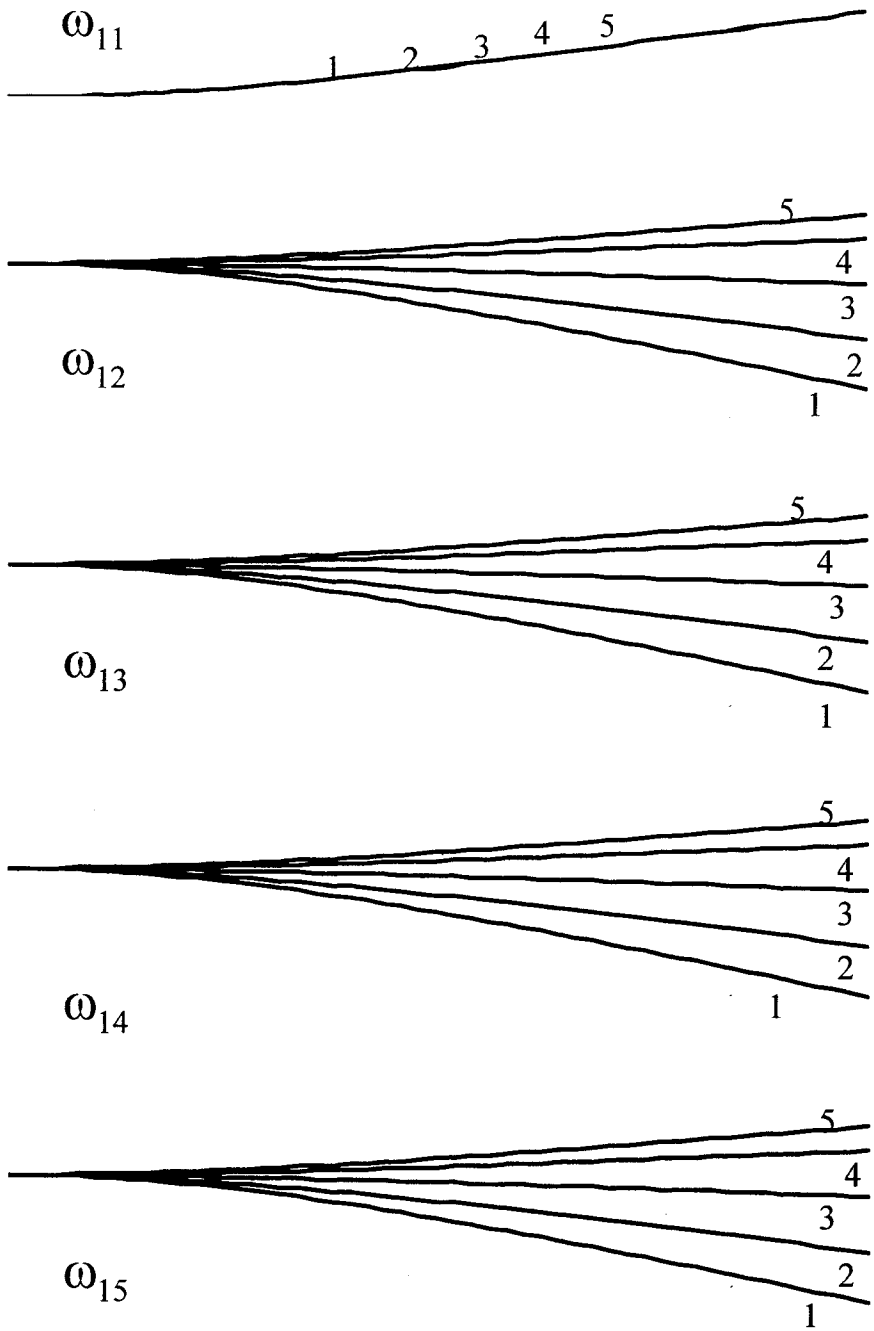

Fig. 3.13. Five intertube vibrational modes of a cantilever 5-wall CNT. (with $L/d = 10$, $k/c_4 = 0.001$, and $n=1$).

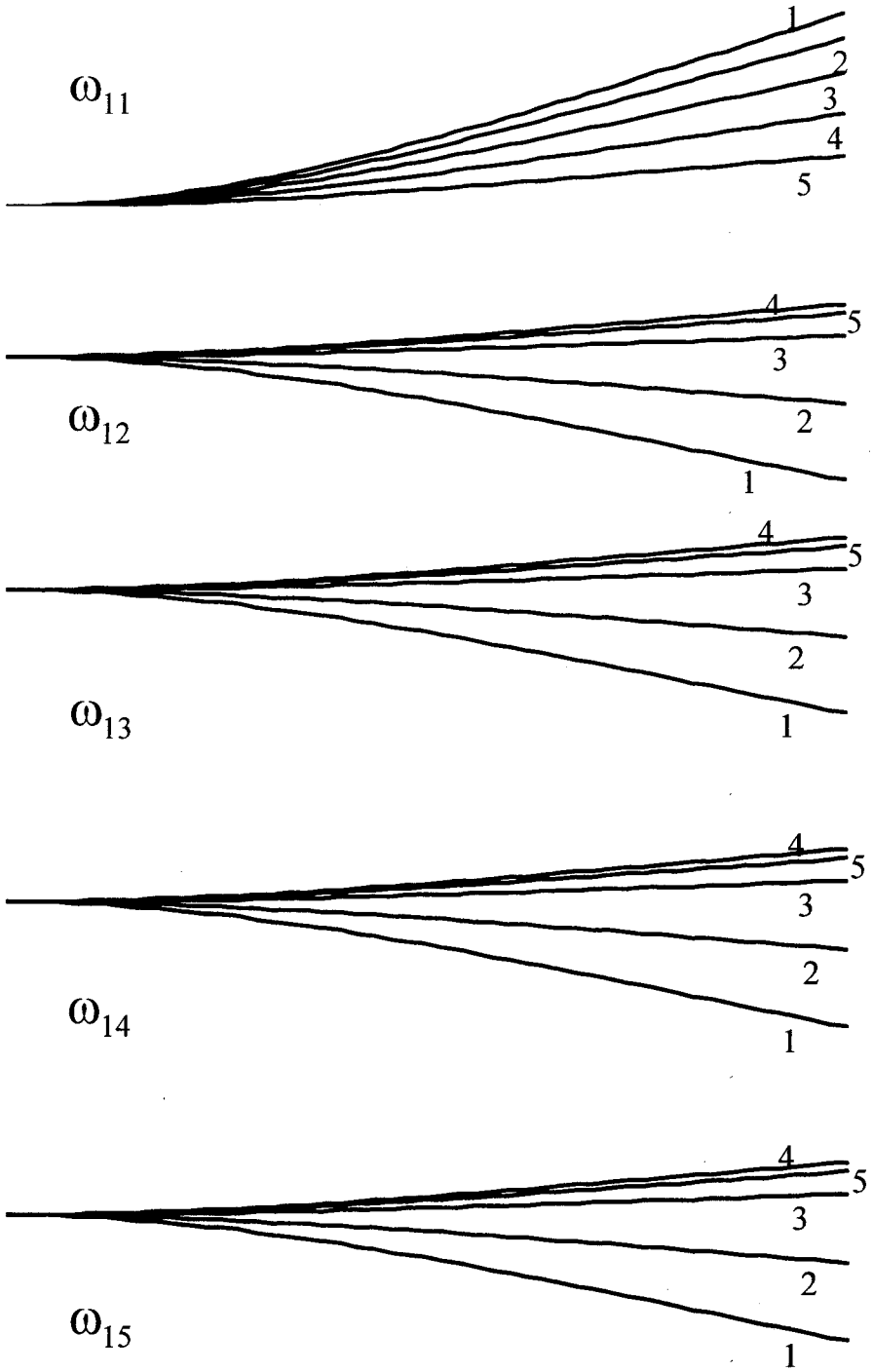

Fig. 3.14. Five intertube vibrational modes of a cantilever 5-wall CNT. (with $L/d = 10$, $k/c_4 = 1$, and $n=1$).

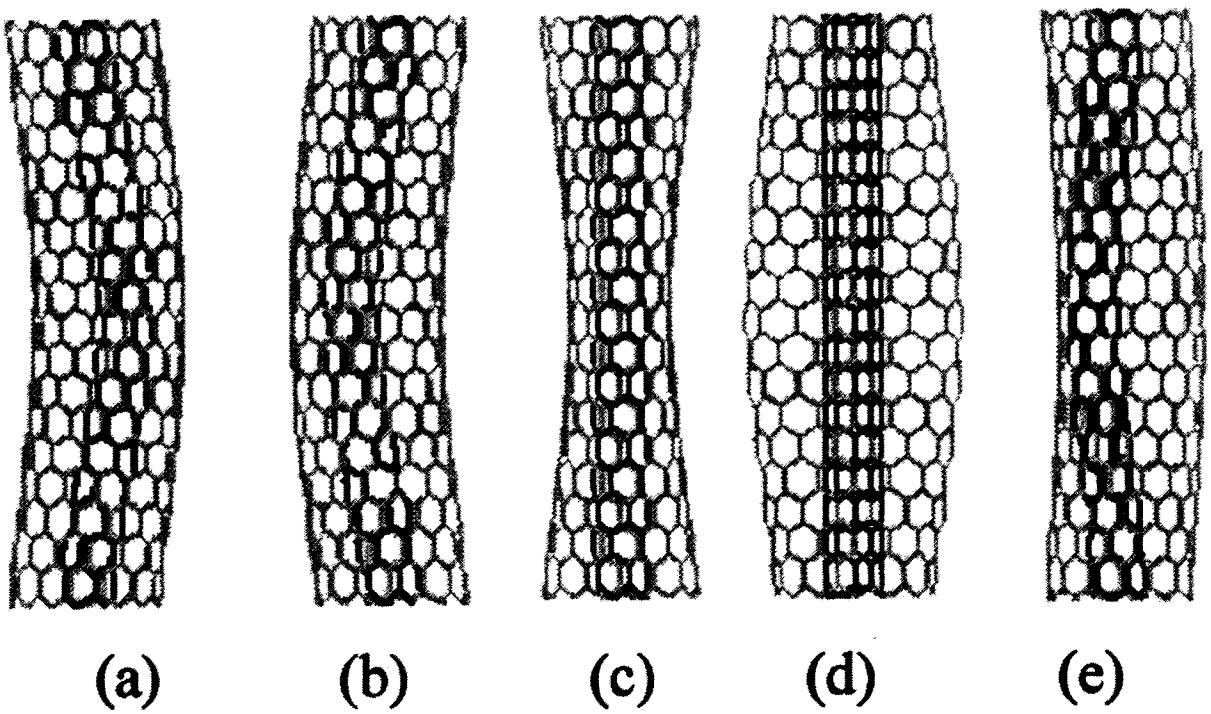

Fig. 3.15. First five vibration modes for a DWNT given by atomistic simulation: Non-coaxial mode is clearly shown in (e) [96]

Chapter 4

Wave Propagation in MWNTs Modeled as Euler-Beams

4.1 Introduction

In the previous Chapter, we have studied the role of interlayer radial displacements and the related internal degrees of freedom in transverse vibration of MWNTs. Our results reveal that the intertube radial displacements, which are ignored by the single-elastic beam model, come to play a crucial role at ultrahigh frequencies. In view of rapidly growing interest in terahertz physics of nanoscale materials and devices [131-135], a relevant open problem is terahertz sound wave propagation in MWNTs. Since prior studies of sound wave propagation in CNTs have been largely limited to SWNTs [78, 93, 136], for MWNT-based electronics, nanodevices and nanocomposites [11, 12, 17-19, 27, 28, 137], it is crucial to understand sound wave propagation in individual MWNTs within terahertz range.

This chapter aims to study sound wave propagation in individual MWNTs. The analysis is based on a multiple-Euler-beam model [72]. The multiple-Euler-beam model predicts that there exist (N-1) critical frequencies (above terahertz) for an N-wall CNT. When the frequency is below all critical frequencies, vibrational mode is almost coaxial, and the associated sound speed

is predicted satisfactorily by the existing single-elastic beam model. When the frequency exceeds at least one of the critical frequencies, however, non-coaxial vibrational modes emerge and propagate at various speeds considerably different than the speed predicted by the single-beam model. Hence, the single-beam model, which has been effectively used to study sound wave propagation in SWNTs [78, 136], fails for MWNTs at ultrahigh frequencies, and non-coaxial sound wave propagation comes to play a dominant role.

4.2 Non-Unique Sound Wave Speeds and the Critical Frequencies

4.2.1 Two Sound Wave Speeds in DWNT

To clearly demonstrate essential ideas of non-coaxial sound wave propagation in MWNTs, let us first consider a DWNT with the innermost diameter 0.7nm. For a sinusoid propagating in an infinite DWNT, the transverse sound wave speed can be studied by substituting $w_1=a_1e^{i(qx-\omega t)}$, $w_2=a_2e^{i(qx-\omega t)}$ to (3.1), which gives [80, 138]

$$\begin{aligned} c_1[a_2-a_1] &= [EI_1q^4-\rho A_1\omega^2]a_1, \\ -c_1[a_2-a_1] &= [EI_2q^4-\rho A_2\omega^2]a_2 \end{aligned} \tag{4.1}$$

where, a_1 and a_2 represent the amplitudes of the inner and the outer tubes, respectively, and q and ω are the wave number and the (circular) frequency. It

turns out that DWNT can have two sound speeds, in contrast to the only sound speed of DWNT given by the single-beam model [78, 136]. The two sound speeds and the amplitude ratio of the inner tube to the outer tube of the associated vibrational modes are given by

$$\begin{aligned} v_1 &= \frac{\sqrt[4]{2}\omega}{\sqrt[4]{\alpha+\sqrt{\alpha^2-4\beta}}}, \\ v_2 &= \frac{\sqrt[4]{2}\omega}{\sqrt[4]{\alpha-\sqrt{\alpha^2-4\beta}}}, \\ \frac{a_1}{a_2} &= 1+\frac{EI_2q^4}{c_1}-\frac{\rho\omega^2 A_2}{c_1} \end{aligned} \tag{4.2}$$

where ($\alpha^2 \geq 4\beta$)

$$\begin{aligned} \alpha &= (\frac{\rho A_1}{EI_1}+\frac{\rho A_2}{EI_2})\omega^2-(\frac{1}{EI_1}+\frac{1}{EI_2})c_1, \\ \beta &= \frac{\rho^2 A_1 A_2}{EI_1 EI_2}\omega^4-c_1\omega^2\frac{\rho(A_1+A_2)}{EI_1 EI_2} \end{aligned} \tag{4.3}$$

In particular, it can be verified that if the van der Waals interaction coefficient is so large that the jump of the deflections between any two tubes is negligible, the speed v_1 given by (4.2) is reduced to that given by (2.7) based on the single elastic beam, while the other speed v_2 given by (4.2) is not real.

It can be verified that v_1 given by (4.2) is always positive, while v_2 is not real for sufficiently low frequency. Thus, there is a critical frequency above

which both v_1 and v_2 given by (4.2) are positive. This critical (circular) frequency is sometime called "cut-off frequency" [80], given by

$$\omega_1 = \sqrt{\frac{(A_1 + A_2)c_1}{\rho A_1 A_2}} \tag{4.4}$$

When the frequency is below the critical frequency (4.4), only one speed exists which is v_1 given by (4.2). On the other hand, when the frequency is higher than the critical frequency (4.4), there are two different sound speeds v_1 and v_2 given by (4.2). The two sound speeds and the respective amplitude ratios of the inner tube to the outer tube are given in Fig. 4.1.

It is seen from Fig. 4.1 that when the frequency is below the critical frequency (4.4), only one sound speed exists, and the associated vibrational mode of the DWNT is almost coaxial (with the amplitude ratio close to unity) except when the frequency is very close to the critical one. In this case, the unique sound speed is very close to that given by the single-beam model (2.7). However, once the frequency exceeds the critical frequency, a new non-coaxial vibrational mode emerges which propagates at a speed v_2 much higher than the speed (2.7) given by the single-beam model. In particular, this non-coaxial mode is characterized by negative amplitude ratio, which indicates that the deflection of the outer tube is opposite to the deflection of the inner tube. When the frequency is much higher than the critical frequency, the two speeds (4.2) predicted by the present model are significantly different from that given by the

single-beam model, and their vibrational modes are substantially non-coaxial. Therefore, the single-beam model, which has been effectively applied to sound wave propagation in SWNTs [78, 136], fails for MWNTs at ultrahigh frequencies, and non-coaxial vibration comes to play the dominant role.

Here, it is noticed that the critical frequency (4.4) predicted by the present model is very close to the intertube resonant frequency of DWNTs predicted by [70]. In particular, similar to the latter, the critical frequency (4.4) predicted by the present model is insensitive to the inner radius of DWNTs. For instance, the critical (circular) frequency (4.6) is 8.034THz, 9.063THz, 9.20THz, and 9.26THz, when the inner radii of the DWNT are 0.35nm, 3.5nm, 10nm, and 50nm, respectively.

4.2.2 Five Sound Wave Speeds in 5-wall CNT

Let us now consider a 5-wall CNT with the innermost diameter 0.7 nm, and the outermost diameter 3.5nm. For a sinusoid propagating in an infinite 5-wall CNT, the transverse sound wave speed can be studied by substituting $w_j = a_j e^{i(qx-\omega t)}$ (j=1,2...5) to (3.6), which gives

$$
\begin{aligned}
&c_1[a_2 - a_1] = [EI_1 q^4 - \rho A_1 \omega^2]a_1, \\
&c_2[a_3 - a_2] - c_1[a_2 - a_1] = [EI_2 q^4 - \rho A_2 \omega^2]a_2, \\
&c_3[a_4 - a_3] - c_2[a_3 - a_2] = [EI_3 q^4 - \rho A_3 \omega^2]a_3, \\
&c_4[a_5 - a_4] - c_3[a_4 - a_3] = [EI_4 q^4 - \rho A_4 \omega^2]a_4, \\
&-c_4[a_5 - a_4] = [EI_5 q^4 - \rho A_5 \omega^2]a_5
\end{aligned}
\qquad (4.5)
$$

It turns out that there exist four critical frequencies $\omega_1 < \omega_2 < \omega_3 < \omega_4$. For the present example, the four critical (circular) frequencies are 4.14THz, 7.12THz, 9.56THz, and 11.40THz, respectively. Five sound speeds are given in Fig. 4.2, with comparison to the speed given by the single-beam model (2.7). In addition, the associated amplitude ratios of the four inner tubes to the outermost tube are given in Figs. 4.3-4.7 for each of the five different sound speeds. It is seen that when the frequency is below the lowest critical frequency, only one sound speed is real, and the associated vibrational mode is almost coaxial except when the frequency is very close to the critical one. In this case, the only sound speed is very close to that given by the single-beam model. However, once the frequency exceeds the lowest critical frequency but is still below the second critical frequency, a new non-coaxial vibrational mode emerges (see Fig. 4.4) which propagates at a speed much higher than the speed (2.7) given by the single-beam model (see Fig.4.2). This non-coaxial mode is characterized by negative amplitude ratio a_1/a_5, which indicates that the deflection of the innermost tube is opposite to the deflection of the outermost tube. Furthermore, when the frequency exceeds the second critical frequency but is still below the third critical frequency, two non-coaxial vibrational modes exist (see Figs. 4.4 and 4.5) which propagate at two distinct speeds significantly different than the speed (2.7) given by the single-beam model (see Fig.4.2). Similar phenomena occur when the frequency increases and exceeds the third and the highest critical frequency. Finally, when the frequency is higher than all four critical frequencies, most of the five speeds predicted by the present model are

significantly different from that given by the single-beam model, and their vibrational modes are substantially non-coaxial (see Figs. 4.3-4.7). These results clearly show that the single-beam model fails to predict the sound speed and vibrational mode for MWNTs at ultrahigh frequencies, and sound wave propagation in MWNTs exhibits complex new phenomena and is highly non-coaxial. Therefore, sound wave propagation in MWNTs at ultrahigh frequency has to be described by new model (such as the present model), which accounts for the intertube radial displacements and the associated internal degrees of freedom.

4.3 The Effect of a Surrounding Elastic Medium on Wave Propagation

It has been seen that the critical frequencies play a crucial role in terahertz sound wave propagation in MWNTs. Here, let us examine the effect of a surrounding elastic medium on the critical frequencies of an isolated MWNT. For the sake of simplicity, let us consider a DWNT embedded within an elastic medium. In this case, the pressure p per unit axial length, acting on the outer tube of the DWNT due to the surrounding elastic medium, can be described by a Winkler-like model (2.4). By substituting $w_1=a_1e^{i(qx-\omega t)}$, $w_2=a_2e^{i(qx-\omega t)}$ to (3.7), one can find that there are two different critical frequencies. Below the lower critical frequency ω_0, no real sound speed exists. When the frequency is between the lower critical frequency (ω_0) and the higher critical frequency (ω_1), only one real sound speed exists. Finally, above the two critical frequencies,

two real sound speeds exist. These critical frequencies ω_0 and ω_1 can be determined by

$$\omega_0 = \sqrt{\frac{1}{2}\{(\frac{c_1}{\rho A_1}+\frac{c_1+k}{\rho A_2}) - \sqrt{(\frac{c_1}{\rho A_1}+\frac{c_1+k}{\rho A_2})^2 - \frac{4c_1 k}{\rho^2 A_1 A_2}}\}}$$
$$\omega_1 = \sqrt{\frac{1}{2}\{(\frac{c_1}{\rho A_1}+\frac{c_1+k}{\rho A_2}) + \sqrt{(\frac{c_1}{\rho A_1}+\frac{c_1+k}{\rho A_2})^2 - \frac{4c_1 k}{\rho^2 A_1 A_2}}\}} \quad (4.6)$$

The dependency of the critical frequencies on the spring constant is shown in Fig. 4.8. It is seen that the lower critical frequency ω_0 increases with the increasing spring constant, and is determined essentially by the surrounding elastic medium [80]. On the other hand, the higher critical frequency ω_1 is insensitive to the spring constant. In particular, ω_0 given by (4.6) is very close to the critical frequency given by [80] for a single-beam surrounded by an elastic medium. For example, when inner radius R_1 is 0.35nm, the lower critical frequency given by (4.6) is 0.12THz (k/c=0.001), 3.55THz (k/c=1), while that given by the single-beam model [80] is 0.12THz (k/c=0.001), 3.79THz (k/c=1). It is also seen from Fig. 4.9 that when the frequency is between the lower critical frequency ω_0 and higher critical frequency ω_1, the unique sound speed is very close to that given by the single-beam model [80] in the presence of an elastic medium. However, above the higher critical frequency ω_1, the two speeds predicted by the present model are significantly different from that given by the single-beam model.

4.4 Summary

In summary, sound wave propagation in MWNTs is studied based on a multiple-Euler-beam model. It is found that there are (N-1) critical frequencies for an N-wall CNT. Sound wave propagation in MWNTs is essentially coaxial only when the frequency is much below all critical frequencies, and becomes substantially non-coaxial when the frequency is higher than at least one of the (N-1) critical frequencies. In the latter case, the sound speeds predicted by the present model are significantly higher or lower than that given by the existing single-beam model, depending not only on the frequency but also on the vibrational modes. In particular, when the frequency is higher than all (N-1) critical frequencies, N different sound speeds will exist simultaneously with their respective non-coaxial vibrational modes. In view of the fact that non-coaxial vibration would crucially alter some important physical properties of MWNTs, it is anticipated that new physical phenomena will occur in ultrahigh-frequency sound wave propagation in MWNTs. Here, we would like to mention that recent progress in nanodevices has made it feasible or more practical to generate and detect vibration and wave propagation in terahertz range [131-134].

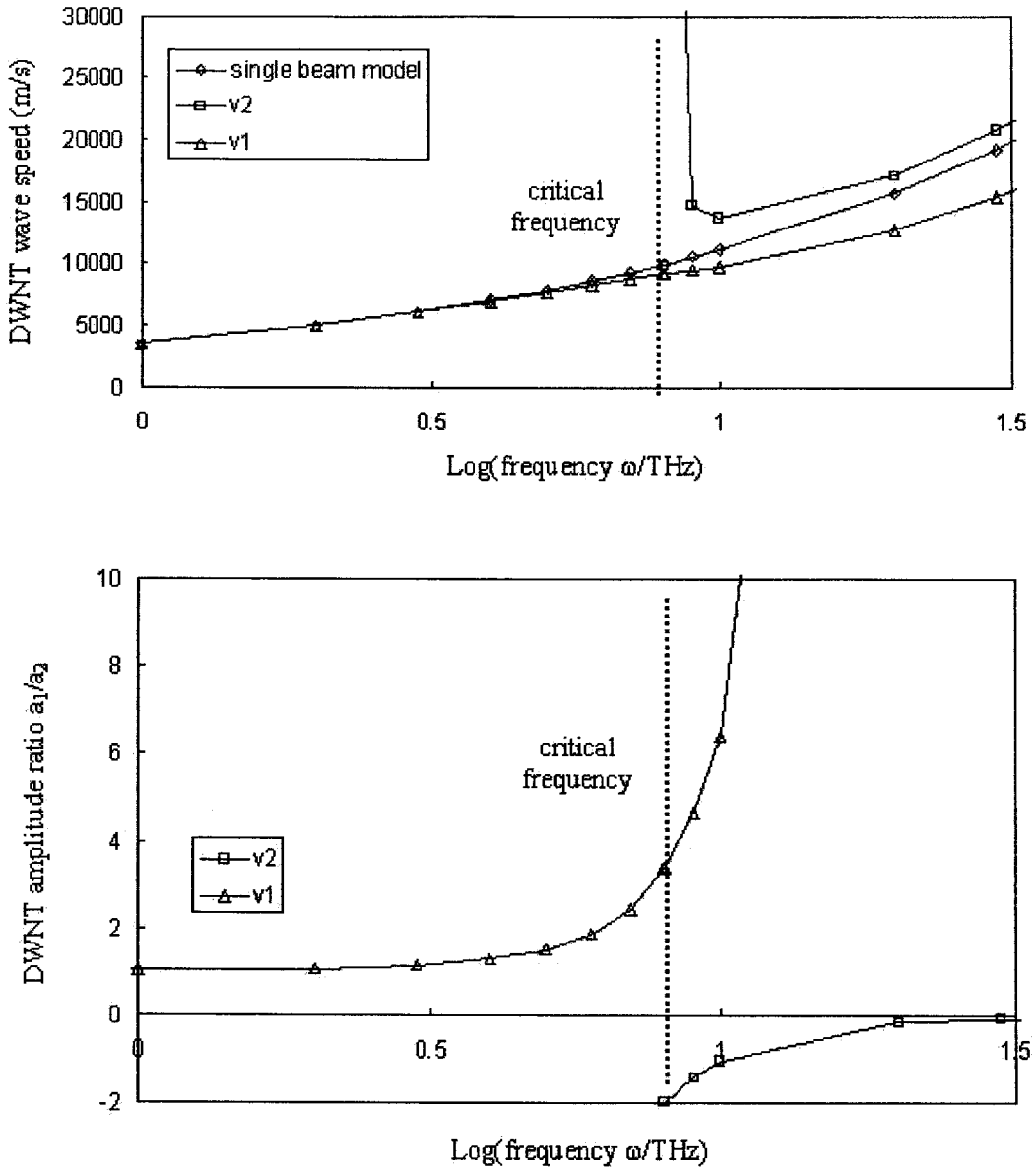

Fig.4.1. DWNT wave speeds and the associated amplitude ratios

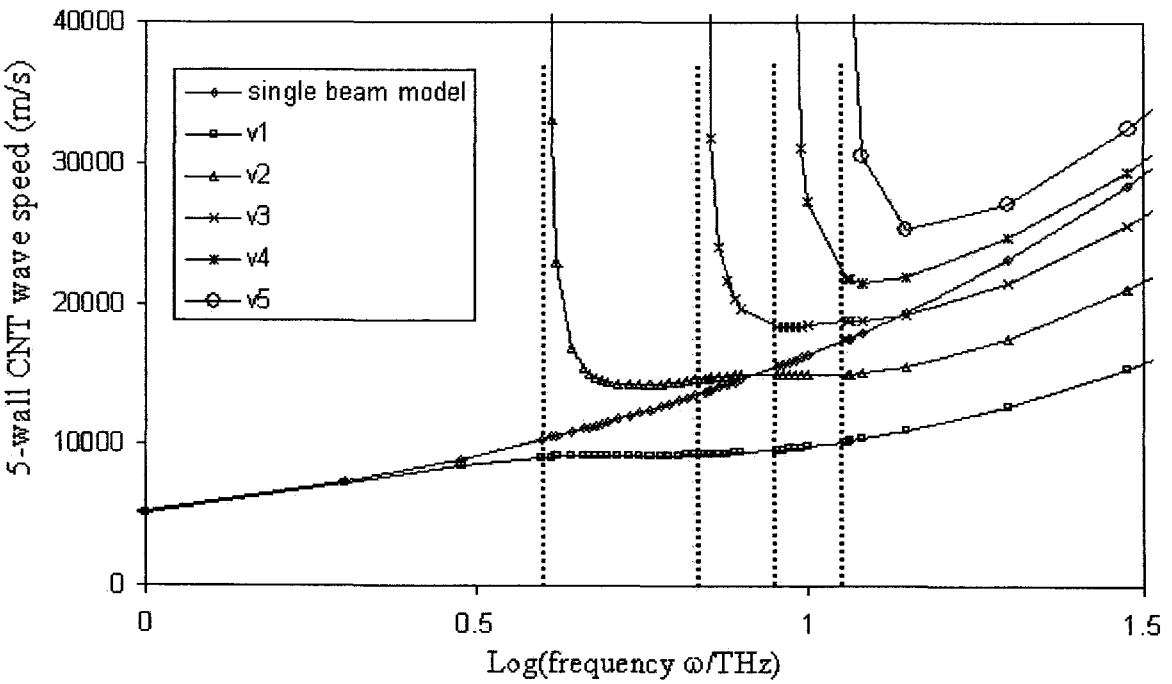

Fig.4.2. The wave speeds as function of frequency in 5-wall CNT

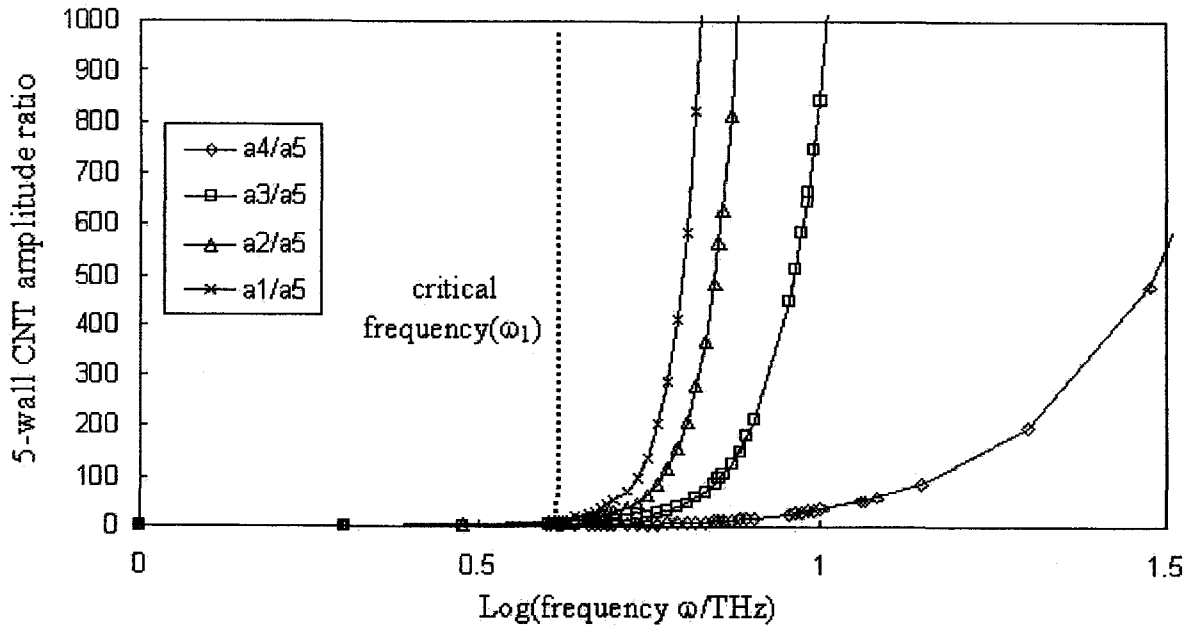

Fig. 4.3. 5-wall CNT amplitude ratios for the speed v_1

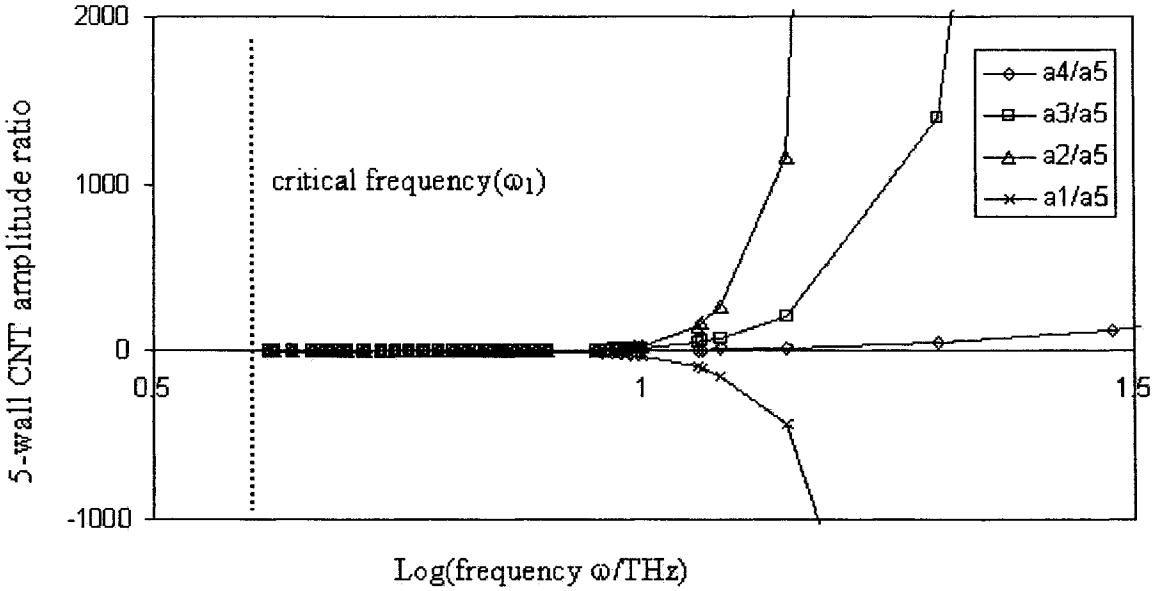

Fig. 4.4. 5-wall CNT amplitude ratios for the speed v_2

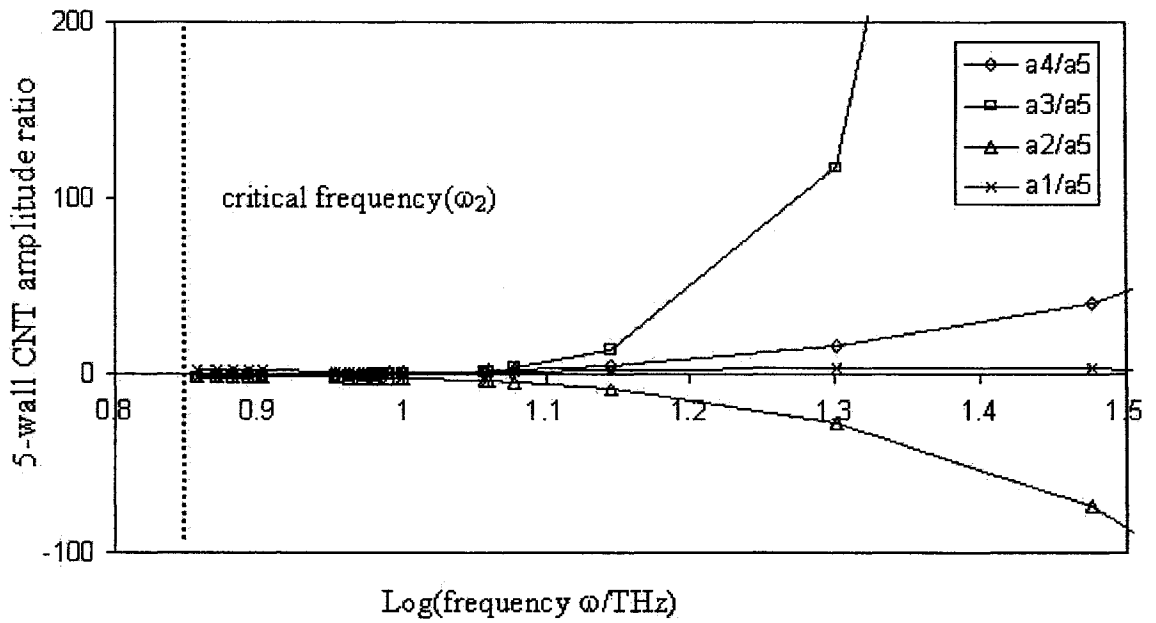

Fig. 4.5. 5-wall CNT amplitude ratios for the speed v_3

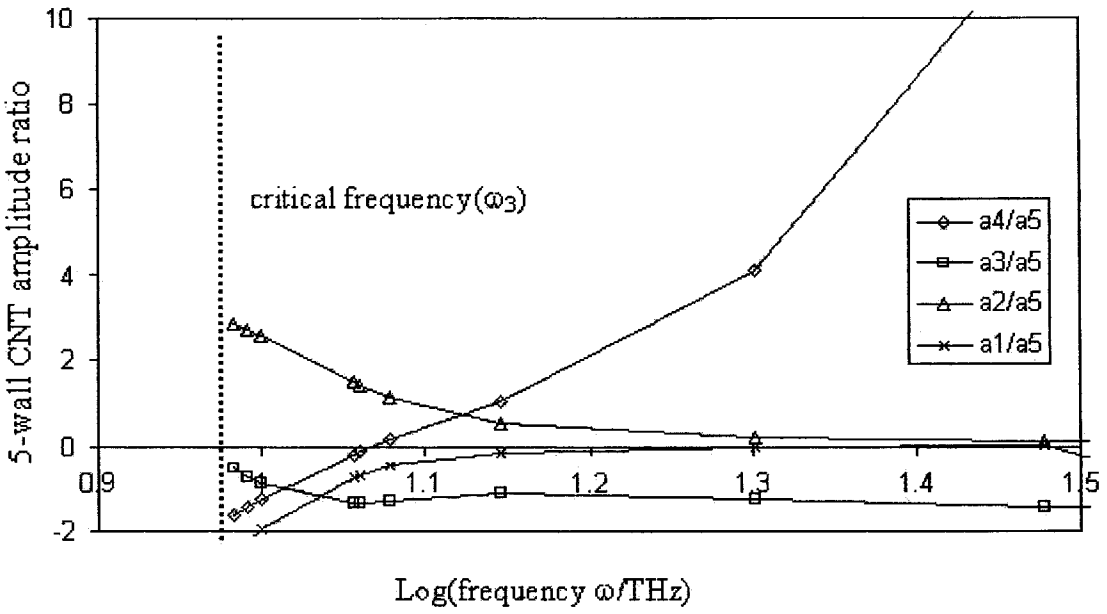

Fig. 4.6. 5-wall CNT amplitude ratios for the speed v_4

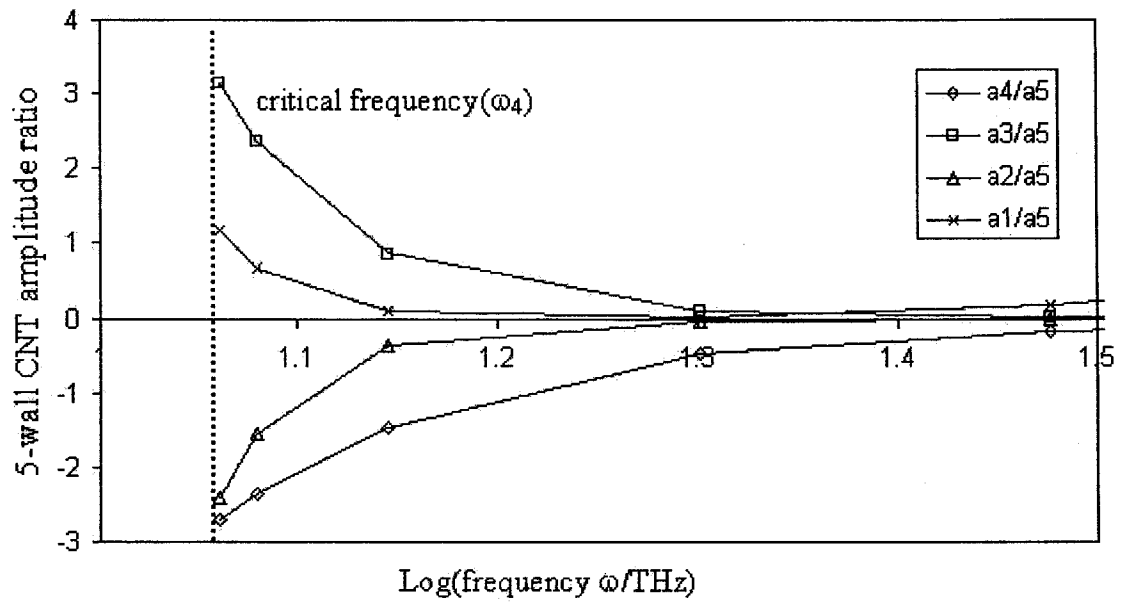

Fig. 4.7. 5-wall CNT amplitude ratios for the speed v_5

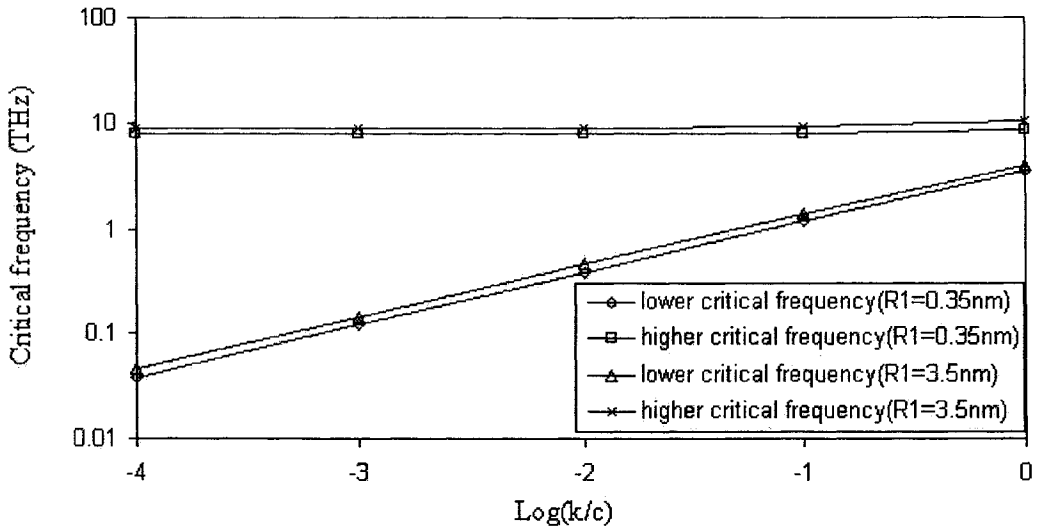

Fig. 4.8. Dependency of the critical frequencies on the spring constant

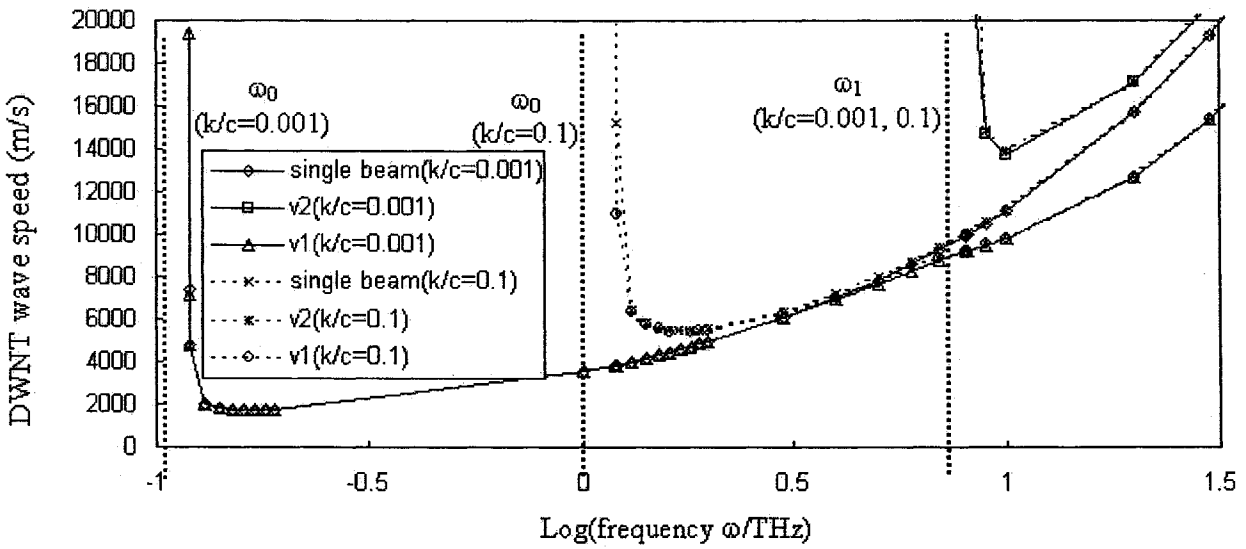

Fig. 4.9. DWNT wave speed in the presence of a surrounding elastic medium

Chapter 5

Vibration of MWNTs Modeled as Timoshenko-Beams

5.1 Introduction

Many proposed applications and designs of CNTs are involved with short CNTs of aspect ratio down to 10, or periodically supported CNTs with finite spans. Such examples include suspended crossing CNTs with spans about 20 nm [10], CNTs as single-electron transistors of length down to 20 nm [22], MWNTs of aspect ratio around 20 (about 300 nm long and 10-20 nm in diameter) as electrometers [33] or building blocks in nanoelectronics [19], CNT-nanomechanical switches of aspect ratio around 10 [21], and CNTs of aspect ratio about 10-25 as AFM tip [20, 34]. Owing to the hollow structure of CNTs, short CNTs are preferred in many cases to prevent undesirable kinking and buckling. Therefore, vibrational behavior of short CNTs, say, of aspect ratio between 10 and 50, is of practical significance. In this case, intertube radial displacements of MWNTs, which are ignored by the existing single-elastic beam model [37, 38, 55, 90], could come to play a significant role.

In Chapter 3, we have studied the role of interlayer radial displacements in transverse vibration of MWNTs [70, 71] based on a simple linear model of multiple-Euler-beams. Our results show that non-coaxial intertube vibration of

short MWNTs will be excited at ultrahigh frequencies (above 1 THz) at which the characteristic wavelength of vibrational modes is just a few times the outermost diameter of MWNTs. In this case, the existing single-beam model of coaxial vibration fails, and a more relevant model that considers non-coaxial intertube radial displacements of MWNTs is required.

Another relevant issue to be clarified is the effects of rotary inertia and shear deformation in terahertz vibrations of short CNTs. It is well-known that rotary inertia and shear deformation, which are ignored in the classical Euler-beam model, would become substantial for vibration of elastic beams when the characteristic wavelength is just a few times the diameter of their cross-section [79, 109-111]. For this reason, the relevance of the classical Euler-beam model to short CNTs is questionable. To clarify this issue, vibration of short DWNTs is studied in this Chapter based on the multiple-Timoshenko-beam model developed in [73, 74], instead of multiple-Euler-beams.

The major goal of this study is to identify the cases in which the Euler-beam model leads to substantial errors and thus the more relevant Timoshenko-beam model is required, and also to compare the Timoshenko-beam effects with the Multiple-beam effects studied in [70, 71]. To this end, detailed results are demonstrated based on the Timoshenko-beam model, as well as the Euler-beam-model. As will be shown below, the results show that the rotary inertia and shear deformation have a substantial effect on higher-order resonant frequencies (within terahertz range) of DWNTs of smaller aspect ratio (between 10 and 20). Therefore, the Timoshenko-beam model, rather than the Euler-beam

model, should be used for terahertz vibrations of short CNTs [74].

5.2 Double-Timoshenko-Beam Model for Vibration

So far, all elastic beam models used for CNTs are based on the classical Euler-beam model. This chapter studies vibration of short DWNTs [108, 123, 124], based on the Timoshenko-beam model. Let us apply equations (2.13) to each of the inner and outer tubes of a DWNT. Thus, transverse vibration of a DWNT, of length L and outer diameter d, is described by the following four coupled equations for four unknowns $w_j(x, t)$ and $\varphi_j(x, t)$ (j=1,2)

$$\begin{aligned}
&-KA_1G(\frac{\partial\varphi_1}{\partial x}-\frac{\partial^2 w_1}{\partial x^2})+c_1(w_2-w_1)=\rho A_1\frac{\partial^2 w_1}{\partial t^2}\\
&EI_1\frac{\partial^2\varphi_1}{\partial x^2}-KA_1G(\varphi_1-\frac{\partial w_1}{\partial x})=\rho I_1\frac{\partial^2\varphi_1}{\partial t^2}\\
&-KA_2G(\frac{\partial\varphi_2}{\partial x}-\frac{\partial^2 w_2}{\partial x^2})-c_1(w_2-w_1)=\rho A_2\frac{\partial^2 w_2}{\partial t^2}\\
&EI_2\frac{\partial^2\varphi_2}{\partial x^2}-KA_2G(\varphi_2-\frac{\partial w_2}{\partial x})=\rho I_2\frac{\partial^2\varphi_2}{\partial t^2}
\end{aligned} \tag{5.1}$$

where, the two tubes have the same Young's modulus E=1TPa and shear modulus G=0.4Tpa (with Poisson ratio v=0.25), with the effective thickness of SWNTs, 0.35nm. In addition, the dependence of the shear coefficient k on the radius is neglected for DWNTs, and we take k=0.8. Here, it should be mentioned that a mass density $\rho=1.3g/cm^3$, based on a slightly different definition ([94] p724), has been used in our previous Chapters 2 and 3. To be consistent with the definitions of the effective thickness and the Young's

modulus listed above, the mass density of graphite is used in this chapter. Therefore, from this chapter, we shall use the mass density $\rho=2.3 g/cm^3$.

5.2.1 Resonant Frequencies of DWNTs

Here, to isolate the effects of shear deformation and rotary inertia on resonant frequencies (rather than resonant modes), we consider the case in which the inner and outer tubes of the DWNT are simply supported. In this case, vibrational modes of the DWNT are of the form [79, 109]

$$\begin{aligned} Y_j &= a_j e^{i\omega t}\sin\frac{n\pi x}{L} \\ \varphi_j &= b_j e^{i\omega t}\cos\frac{n\pi x}{L} \end{aligned} \qquad (j=1,2) \qquad (5.2)$$

where a_1 and a_2 represent the amplitudes of deflections of the inner and the outer tubes, and b_1 and b_2 represent the amplitudes of the slopes of the inner and outer tubes due to bending deformation alone, respectively. In addition, integer n is the mode-number, and ω is the circular frequency. Substitution of (5.2) into (5.1), one has

$$\begin{bmatrix} \rho A_1\omega^2 - kA_1G(\frac{n\pi}{L})^2 - c & kA_1G(\frac{n\pi}{L}) & c & 0 \\ kA_1G(\frac{n\pi}{L}) & \rho I_1\omega^2 - EI_1(\frac{n\pi}{L})^2 - kA_1G & 0 & 0 \\ c & 0 & \rho A_2\omega^2 - kA_2G(\frac{n\pi}{L})^2 - c & kA_2G(\frac{n\pi}{L}) \\ 0 & 0 & kA_2G(\frac{n\pi}{L}) & \rho I_2\omega^2 - EI_2(\frac{n\pi}{L})^2 - kA_2G \end{bmatrix} \begin{bmatrix} a_1 \\ b_1 \\ a_2 \\ b_2 \end{bmatrix}$$

$$=0 \qquad (5.3)$$

Thus, the resonant frequencies are determined by the eigen-equation obtained by setting the determinant of the coefficient matrix of (5.3) to zero. It is readily seen that for given order-number n, the present double-Timoshenko-beam model gives four n-order resonance frequencies, in contrast to two n-order resonant frequencies given by the single-Timoshenko-beam model [79], two n-order resonant frequencies given by the double-Euler-beam model [70, 71], and the single n-order resonance frequency given by the single-Euler-beam model. In particular, the single n-order resonant frequency given by the single-Euler-beam model is

$$f_{n1} = \frac{\omega_{n1}}{2\pi}, \qquad \omega_{n1}^2 = \frac{\lambda_n^4 EI}{(\rho A)}, \tag{5.4}$$

where $\lambda_n = (n\pi/L)$ for simply supported beams

where I and A are the total moment of inertia and the total cross-sectional area of MWNT. Thus, $I=I_1+I_2$ and $A=A_1+A_2$ for a DWNT.

In what follows, the resonant frequency $f=\omega/(2\pi)$ of simply supported DWNTs is calculated based on four different elastic beam models:

(DT): the double-Timoshenko-beam (DT) model described by (5.1) which gives four n-order frequencies, $f_{n1} < f_{n2} < f_{n3} < f_{n4}$;

(DE): the double-Euler-beam (DE) model described in [70, 71] which treats each of the inner and outer tubes of the DWNT as a single-Euler-beam and gives two n-order frequencies, $f_{n1} < f_{n2}$;

(ST): the single-Timoshenko-beam (ST) model which treats the DWNT as a single-Timoshenko-beam described by (2.12), with $I=I_1+I_2$ and $A=A_1+A_2$, and gives two n-order frequencies, $f_{n1} < f_{n2}$;

(SE): the single-Euler-beam (SE) model, which gives the single n-order frequency f_{n1} (5.4).

The n-order frequencies given by the different models are distinguished by (DT1<DT2<DT3<DT4), (DE1<DE2), (ST1<ST2) or (SE), when necessary. All nine n-order frequencies given by the four different models are shown in Figs. 5.1-5.6 for a DWNT of the inner diameter 0.7nm or 7nm and aspect ratio 10, 20 or 50, respectively. All frequencies are shown as a function of the mode-number n, from n=1 to n=10, where L/d_{out} is the aspect ratio. It is found from Figs. 5.1- 5.6 that:

1) The lowest n-order frequency f_{n1} increases quickly with increasing mode-number n, while other higher n-order frequencies f_{nk} (k>1) are not sensitive to the number n especially for n smaller than 3 or 4.

2) For all examples considered here, the four lowest first-order frequency (f_{11}) given by the four different models are very close to each other and almost indistinguishable. For example, for DWNT of inner-diameter 0.7 nm and aspect ratio 10, the lowest first-order frequencies (f_{11}) given by the four models (DT, DE, ST, SE) are 0.0728THz, 0.0745THz, 0.0731THz, and 0.0746THz,

respectively. On the other hand, for DWNT of inner-diameter 7 nm and aspect ratio 10, the lowest first-order frequency (f_{11}) given by the four models are 0.141THz, 0.144THz, 0.141THz, and 0.144THz, respectively. In addition, the small differences of the lowest first-order frequencies given by the four different models further diminish with increasing aspect ratio of DWNTs.

3) For the mode-number n=1, beside the lowest first-order frequency, the DT-model gives three higher frequencies, while the ST-model and the DE-model give another higher frequency, respectively. It is seen that the 2nd first-order frequency (f_{12}) given by the DT-model corresponds to the second first-order frequency given by the DE-model for smaller radii (Figs.5.1-5.3), and the 3rd first-order frequency (f_{13}) given by the DT model is close to the second first-order frequency given by the ST-model for larger radii (Figs.5.4-5.6). These higher first-order frequencies (n=1) are characterized by substantial shear deformation or non-coaxial deflections of the inner and outer tubes (as will be demonstrated below) and are at least one order of magnitude higher than the lowest first-order frequency. Hence, if only the single lowest resonant frequency (f_{11}) is concerned, the lowest first-order frequency given by the SE model (5.4) for n=1 is accurate enough, and any double-beam model or Timoshenko-beam model is not needed.

4) This conclusion remains qualitatively true even for the first few higher-order frequencies (n=3, 4, 5 or even higher) when the aspect ratio is larger (say, equal to or larger than 50). Indeed, when L/d=50, it is seen from Fig. 5.3 and Fig. 5.6 that the four lowest n-order frequencies given by the four different models for

the mode-number n up to 10 are very close to each other. Hence, it is concluded that the lowest n-order frequency f_{n1} for n up to 10 can be estimated satisfactorily by the SE-model (5.4) provided that the aspect ratio of DWNTs is sufficiently large (say, equal to or larger than 50).

5) However, when the aspect ratio is relatively small, say between 10 and 20, it is seen from Figs. 5.1, 5.2 and Figs. 5.4, 5.5 that the lowest n-order (such as n=3, 4, or 5) frequencies f_{n1} given by the DT model, the ST model and the DE model are substantially lower than that given by the SE model (5.4). For example, for DWNT of inner-diameter 0.7 nm and aspect ratio 10, the lowest 4^{th}-order frequency (n=4) given by the four models (DT, DE, ST, SE) are 0.861THz, 1.00THz, 0.940THz, and 1.19THz, respectively, and the lowest 5^{th}-order frequency (n=5) given by the four models (DT, DE, ST, SE) are 1.18THz, 1.37THz, 1.34THz, and 1.86THz, respectively. In addition, for DWNT of inner-diameter 7 nm and aspect ratio 10, the lowest 4^{th}-order frequency (n=4) given by the four models (DT, DE, ST, SE) are 0.177THz, 0.231THz, 0.178THz, and 0.231THz, respectively, and the lowest 5^{th}-order frequency (n=5) given by the four models (DT, DE, ST, SE) are 0.252THz, 0.360THz, 0.252THz, and 0.361THz, respectively. Therefore, the single-Euler-beam (SE) model (5.4), used widely in the literature, leads to substantial errors for the lowest n-order resonant frequencies f_{n1} for n>1, (such as n=3, 4 or 5) of short DWNTs of aspect ratio below 20.

6) Finally, because both the Timoshenko-beam model [79, 109-111] and the double-beam model [67, 70, 71] are significant only when the characteristic

wavelength is just a few times the diameter of CNTs, it is interesting to compare the relative importance of the Timoshenko-beam effect and the double-beam effect. It is anticipated that the role of intertube displacements of MWNTs is more significant for small-diameter than for large-diameter CNTs [70, 71] (because the amplitude of the intertube radial displacements is of the order of magnitude of the intertube spacing, they are significant only compared to the deflections of small-diameter CNTs, but not to the deflections of large-diameter CNTs). Indeed, it is seen from Figs 5.1 and 5.2 that the lowest n-order frequencies f_{n1} (for n>1) given by the double-beam models (DT and DE) for small-diameter DWNTs are significantly different from those given by the single-beam models (ST, SE). For larger-diameter DWNTs, however, it is seen from Figs. 5.4 and 5.5 that the double-beam models (DT) and (DE) give almost the same lowest n-order frequencies f_{n1} (for n>1) as those given by the single-beam models (ST, SE). On the other hand, the effects of the Timoshenko-beam are significant for all DWNTs of smaller aspect ratio (Figs. 5.1-5.2 and 5.4-5.5), regardless of their radii. Therefore, it is concluded that both the Timoshenko-beam effects and the double-beam effects are significant for CNTs of smaller aspect ratio (around or below 20), while the double-beam effects are further restricted to small-diameter DWNTs. Despite this, because the radii of DWNTs are usually small (with inner diameter 0.6~0.9nm, and outer diameter 1.3~1.6nm. see [108, 123, 124]), the double-beam effects are significant for short DWNTs.

5.2.2 Shear Deformation and Non-Coaxial Deflections

Let us now discuss the effects of the Timoshenko-beam model, as well as the double-beam model, on the deflection curves of DWNTs. The contribution of shear deformation to the total deflection slope is defined by

$$\theta = \varphi - \frac{dY}{dx} = \gamma e^{i\omega t} \cos\frac{n\pi x}{L} \tag{5.5}$$

where γ represents the amplitude of shear deformation. Obviously, for the single-Euler-beam (SE) model, the deflection curves of the inner and outer tubes are exactly the same and the shear deformation $\theta(x,t)$ is identically zero, thus $a_1=a_2$, $b_1=b_2=a_1(n\pi/L)$ and $\gamma_1=\gamma_2=0$. However, when the Timoshenko-beam model is adopted, shear deformation and rotary inertia are taken into account which give rise to non-zero shear deformation γ. On the other hand, the double-beam model accounts for intertube radial displacement between the inner and outer tubes and thus can quantify the difference between two (non-coaxial) deflection curves ($a_1 \neq a_2$). Therefore, the effects of the Timoshenko-beam and the double-beam can be studied by examining the ratio a_1/a_2, which indicates the degree of the non-coincidence of the deflections of the two tubes, and the ratio γ_2/b_2 which indicates the relative amplitude of the shear deformation of the outer tube of DWNTs (the result for the inner tube is qualitatively similar and thus not included here). It follows from (5.1, 5.2, 5.5) that the deflection amplitude ratio of the inner to the outer tubes, and the ratio of the outer tube's

shear deformation to its deflection slope due to bending deformation are given by

$$\frac{a_1}{a_2} = \frac{(kA_2G\lambda)^2 - (\rho A_2\omega^2 - kA_2G\lambda^2 - c)(\rho I_2\omega^2 - EI_2\lambda^2 - kA_2G)}{c(\rho I_2\omega^2 - EI_2\lambda^2 - kA_2G)}$$

$$\frac{\gamma_2}{\varphi_2} = \frac{I_2(\rho\omega^2 - E\lambda^2)}{kA_2G} \quad , \qquad (\lambda=n\pi/L)$$

(5.6)

In what follows, the ratio a_1/a_2 given by the DT model and the DE-model for the lower two n-order frequencies are shown in Figs. 5.7-5.8 and Figs. 5.9-5.10, respectively, for the examples considered in Figs. 5.1-5.6. Here, because the second n-order frequency (f_{n2}) given by the DT-model corresponds to the second n-order frequency given by DE-model only for smaller radii (see Section 5.2.1), the results for the second n-order frequencies given by the DT-model and the DE-model are demonstrated only for small radius 0.35 nm (Figs 5.8 and 5.10). Related data for the ratio γ_2/b_2 given by the DT model and the ST-model for all n-order frequencies are shown in Figs. 5.11-5.14 and Figs. 5.15-5.16, respectively. It is found from Figs. 5.7-5.16 that:

1) The amplitude ratio a_1/a_2 corresponding to the lowest (first-order) frequency (f_{11}), as shown in Fig. 5.7 for the DT model and Fig. 5.9 for the DE model, are always very close to unity for all examples considered here. This indicates that the deflection curves of the inner and outer tubes for the lowest (first-order) frequency (f_{11}) are almost coincident and thus the vibration of the DWNT is

almost coaxial at the lowest (first-order) frequency f_{11}.

2) For the lowest n-order frequencies f_{n1} with n>3, it is seen from Fig. 5.7 and Fig. 5.9 that the associated amplitude ratio a_1/a_2 is no longer close to unity for small-diameter DWNTs of aspect ratio 10 or 20, which indicates that the deflection curves of the inner and outer tubes are no longer coincident in these cases. However, for larger aspect ratio (50) or larger inner radius (3.5 nm), it is seen from Figs. 5.7 and 5.9 that the amplitude ratio a_1/a_2 for the lowest n-order frequencies f_{n1} with n>3 is still very close to unity and thus the deflection curves of the inner and outer tubes are still almost coincident. Consistent with Section 3, these results also confirm that the effect of the double-beam model is significant only for small-diameter CNTs of smaller aspect ratio. Here, it is noticed from Figs. 5.7 and 5.9 that the ratio a_1/a_2 for the lowest n-order frequency with n>1 of small-diameter DWNTs given by the DT model and the DE model are qualitatively similar, but quantitatively different.

3) On the other hand, the amplitude ratio a_1/a_2 of other higher n-order frequency (f_{nk} with k>1) is not close to unity. For example, for small-diameter DWNTs, it is seen from Figs. 5.8 and 5.10 that the amplitude ratio a_1/a_2 of the second n-order frequency (f_{n2}) is always negative, which indicates that the deflection of the inner tube is simply opposite to the deflection of the outer tube, and thus vibration of the DWNT is substantially non-coaxial. It is seen that from Figs. 5.1-5.6 that the second n-order frequency (f_{n2}) for all examples discussed here is always within terahertz range. Hence, this also indicates that the effects of the double-beam model are essential for terahertz vibration of MWNTs.

4) Now, let us discuss the relative amplitude of shear deformation. For the lowest n-order frequency (f_{n1}), the ratio γ_2/b_2, which represents the relative amplitude of shear deformation of the outer tube, is negligible only for n=1, or for n>1 with larger aspect ratio 50. This indicates that the shear deformation is significant provided that the wavelength is sufficiently short, consistent with the common concepts of the Timoshenko-beam. For example, it is seen from Figs. 5.11 and 5.15 that the six curves can almost be classified by the wavelength, only slightly affected by the radius.

5) For small aspect ratio (10 and 20) and higher mode number n>3, it is seen from Figs. 5.11 and 5.15 that the shear deformation has a substantial effect on the deflections even for the lowest n-order frequency f_{n1}. For example, it is seen from Figs. 5.11 and 5.15 that the absolute value of the ratio γ_2/b_2 is larger than unity for small aspect ratio L/d=10, and is about 25% for moderate aspect ratio L/d=20, almost regardless of the radius. In these cases, the shear deformation, which is neglected by the classical Euler-beam model, is significant and cannot be neglected.

6) It is seen from Figs. 5.12-5.14 and Fig. 5.16 that almost all higher n-order frequencies (f_{nk} with k>1) are characterized by substantial shear deformation, with the only exception described in Fig. 5.12 for the second n-order frequency (f_{n2}) given by the DT-model for small diameter 0.35 nm and smaller order-number n (up to n=4 or 5). In the latter case, as mentioned before, the second n-order frequency (f_{n2}) given by the DT-model corresponds to the second n-order frequency (f_{n2}) given by the DE-model in which shear deformation is neglected.

This explains why the shear deformation is negligible in this case.

7) Except for the above case, all other cases described in Figs. 5.12-5.14 and Fig. 5.16 exhibit substantial shear deformation characterized by large absolute values of the ratio γ_2/b_2. In particular, it is seen from Figs. 5.12-5.14 and Fig. 5.16 that the six curves shown there can almost be classified by the radius, only moderately affected by the wavelength. This indicates that, unlike the vibration of the lowest n-order frequency f_{n1} which largely depends on the wavelength, the vibration of the higher n-order frequencies f_{nk} (with $k>1$) is not sensitive to the wavelength. This conclusion is consistent to similar results obtained in the analysis of resonant frequencies given in section 5.2.1.

5.3 Summary

Free vibration of short DWNTs is studied using a double-Timoshenko-beam model, which considers intertube radial displacements between the inner and outer tubes and treats the inner and outer tubes as two individual Timoshenko-beams. The results indicate that both the Timoshenko-beam effect and the double-beam effect are significant when the wavelength of DWNTs is just a few times larger than the outer diameter of DWNTs. In particular, it is the case when the higher-order frequencies (within the terahertz range) of short DWNTs (of smaller aspect ratio around or below 20) are considered. Furthermore, the results show that the effects of the double-beam are more significant for small-diameter than for large-diameter DWNTs, while the Timoshenko-beam effects are significant for both large-diameter and small-

diameter DWNTs. This is attributed to the fact that the double-beam effects become significant only when the amplitude of interlayer radial displacements (which are of the order of the interlayer spacing) is comparable to the overall deflections of MWNTs (which are of the order of the radius). Because the radii of DWNTs are usually small, the double-beam effects play a significant role in free vibration of short DWNTs. Hence, the effects of the Timoshenko-beam and the double-beam are relevant for terahertz vibration of short MWNTs of aspect ratio below or around 20. On the other hand, if only the single lowest (first-order) resonant frequency is concerned, the classical single-Euler-beam model is accurate enough, any double-beam model or Timoshenko-beam model is not needed even for short MWNTs.

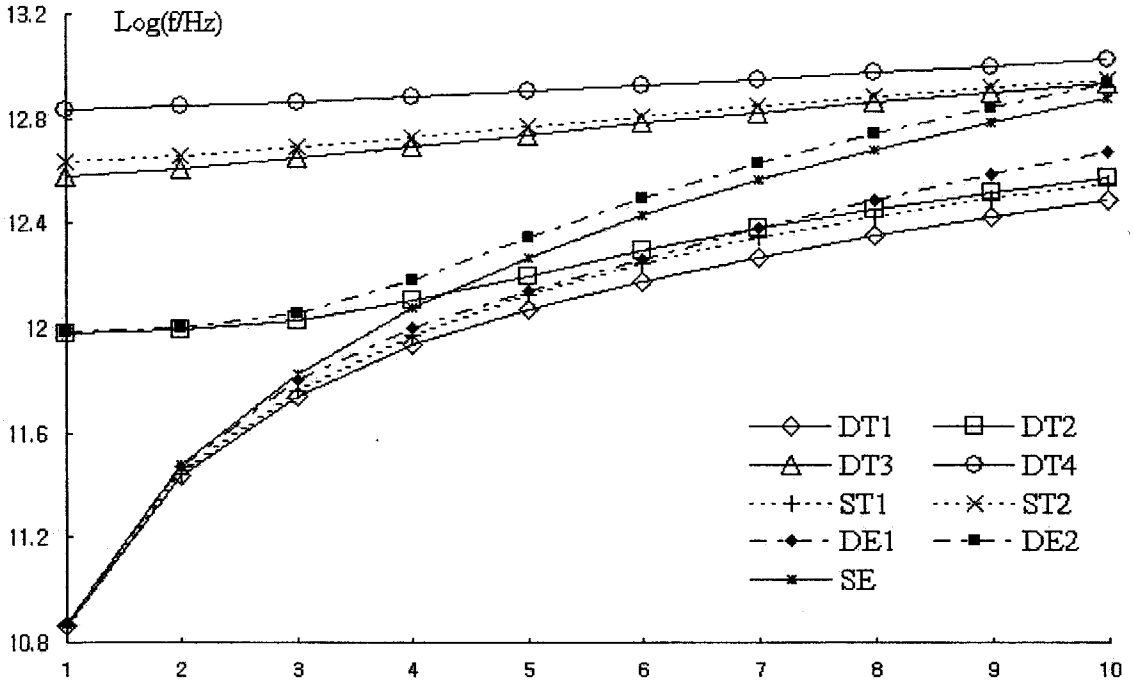

Fig. 5.1. DWNT frequencies for the inner radius 0.35nm and L/d=10

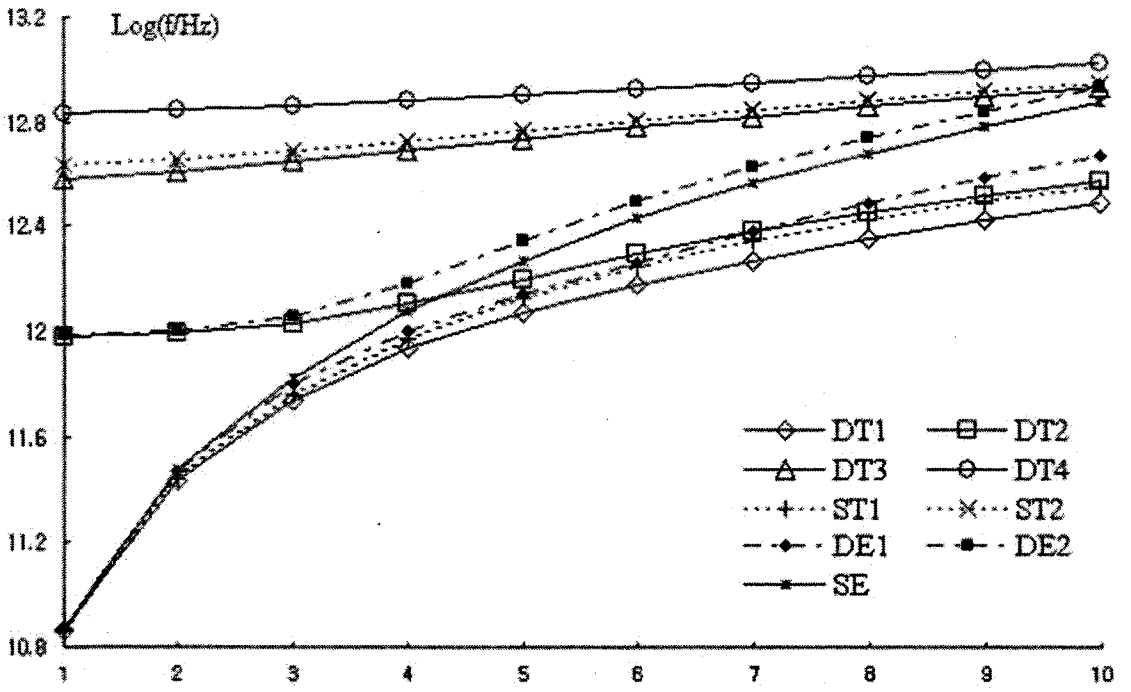

Fig. 5.2. DWNT frequencies for the inner radius 0.35nm and L/d=20

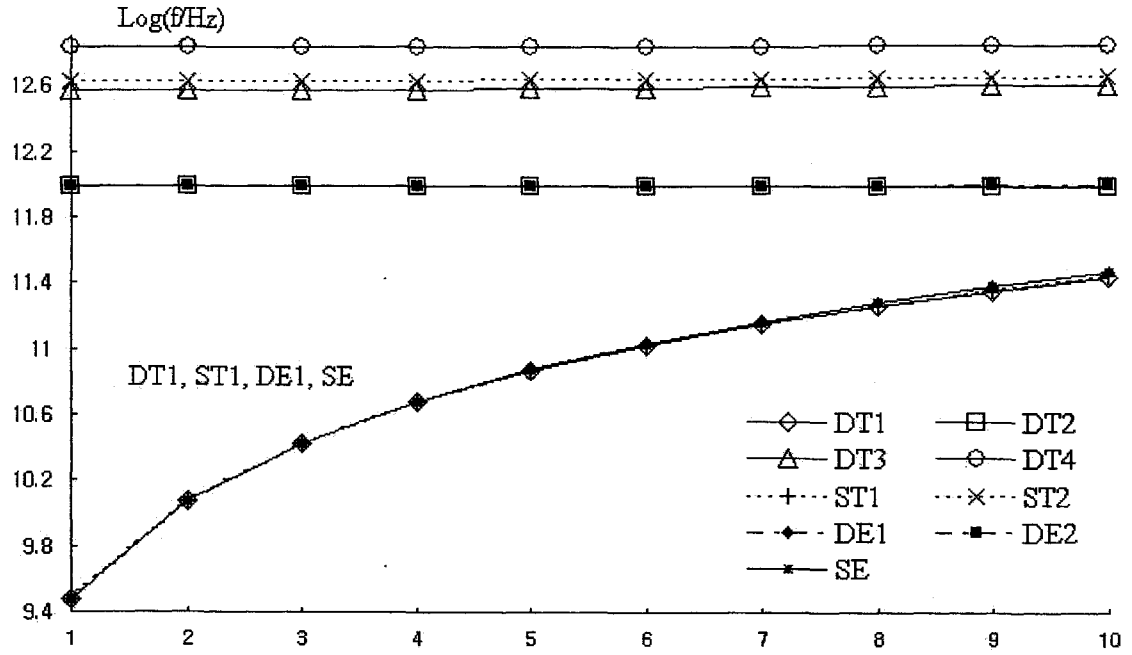

Fig. 5.3. DWNT frequencies for the inner radius 0.35nm and L/d=50

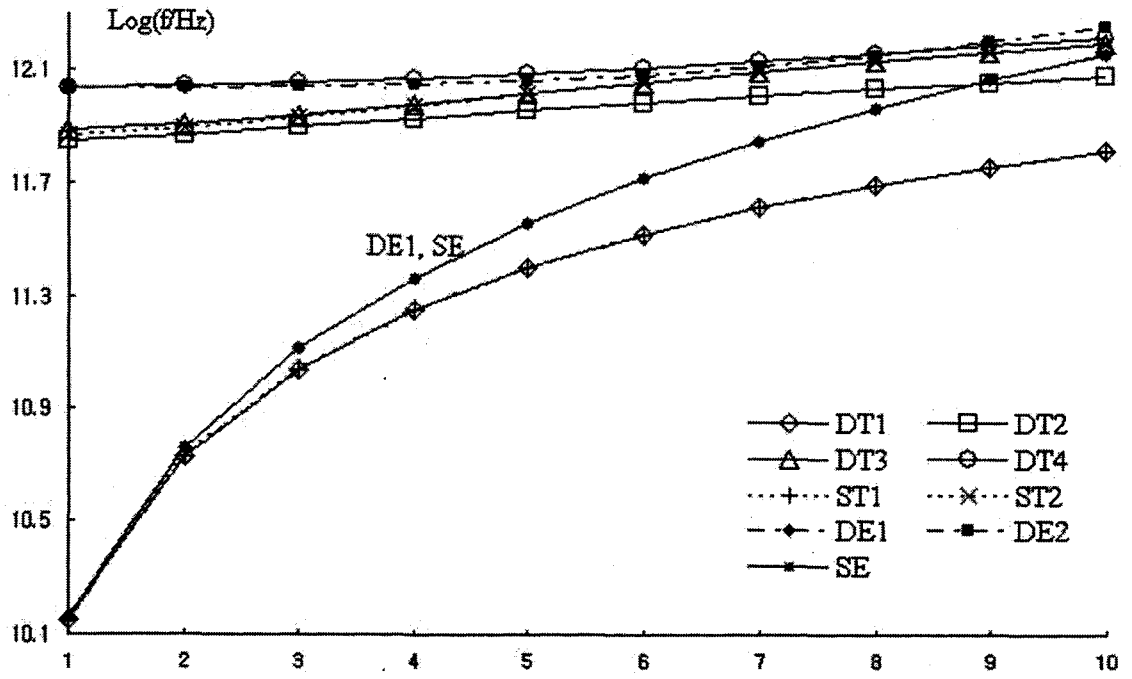

Fig. 5.4. DWNT frequencies for the inner radius 3.5nm and L/d=10

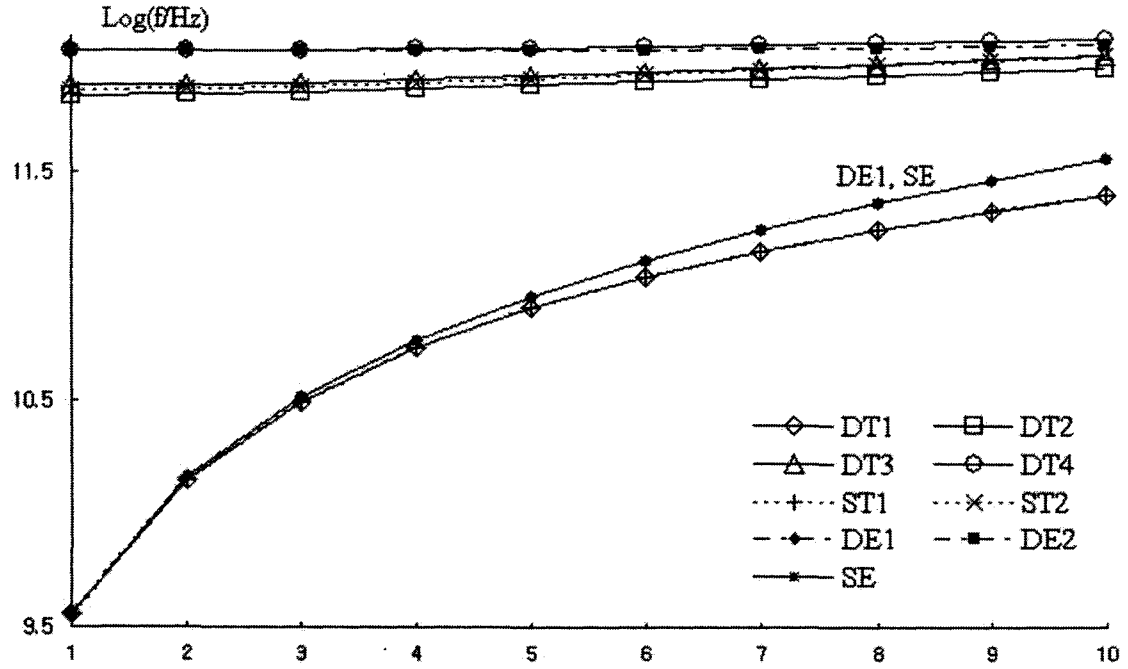

Fig. 5.5. DWNT frequencies for the inner radius 3.5nm and L/d=20

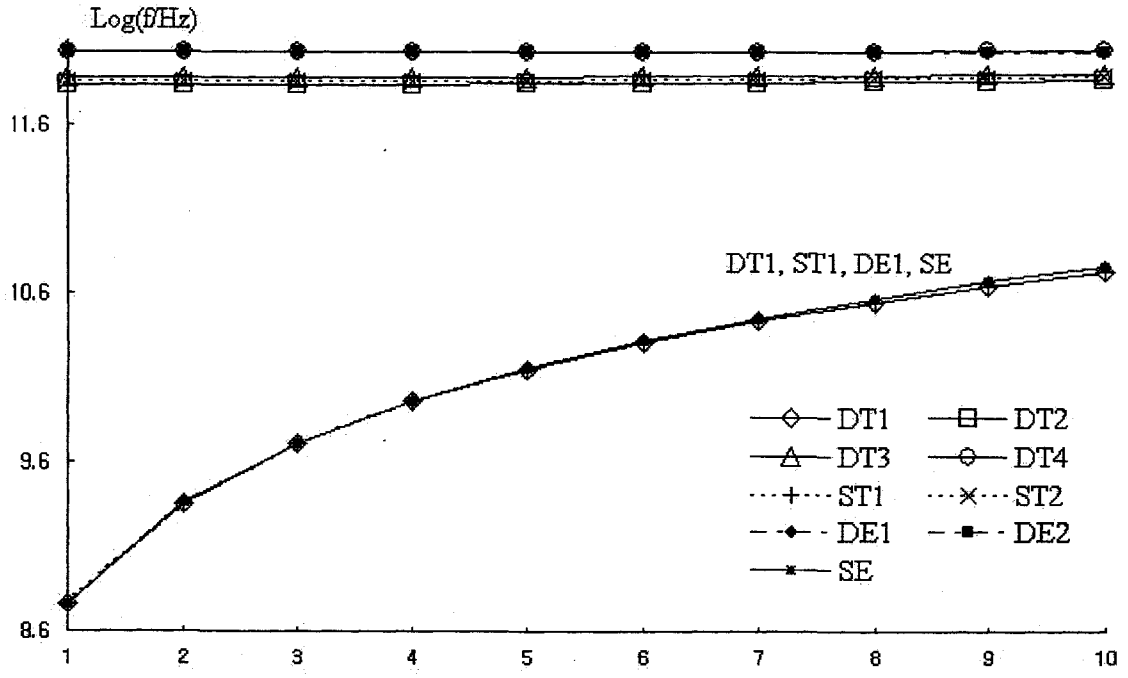

Fig. 5.6. DWNT frequencies for the inner radius 3.5nm and L/d=50

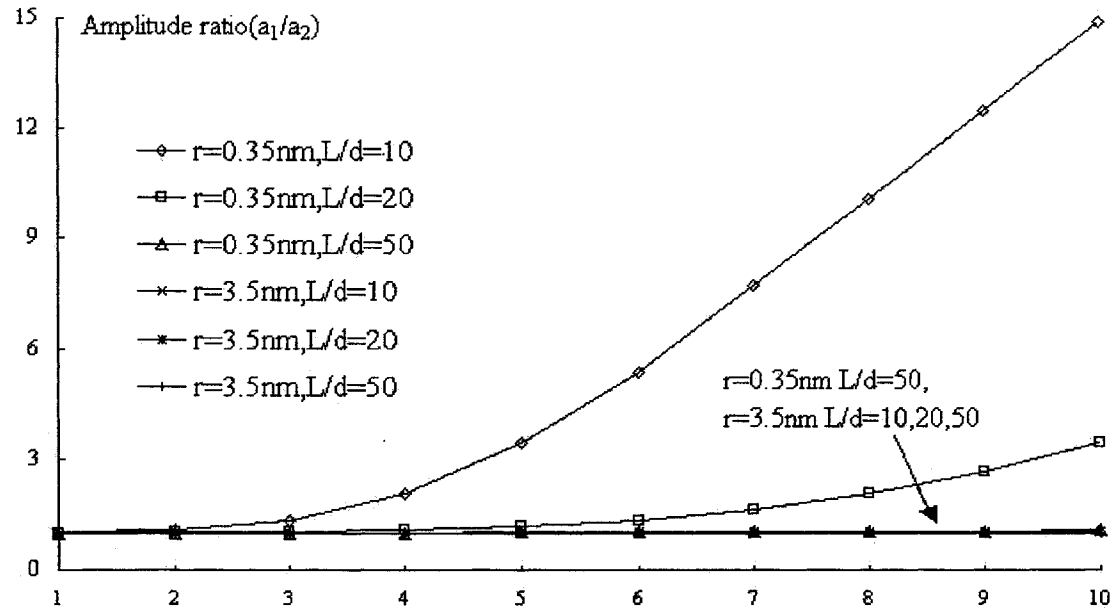

Fig. 5.7. DWNT amplitude ratio (a_1/a_2) for f_{n1} using a double-Timoshenko-beam model

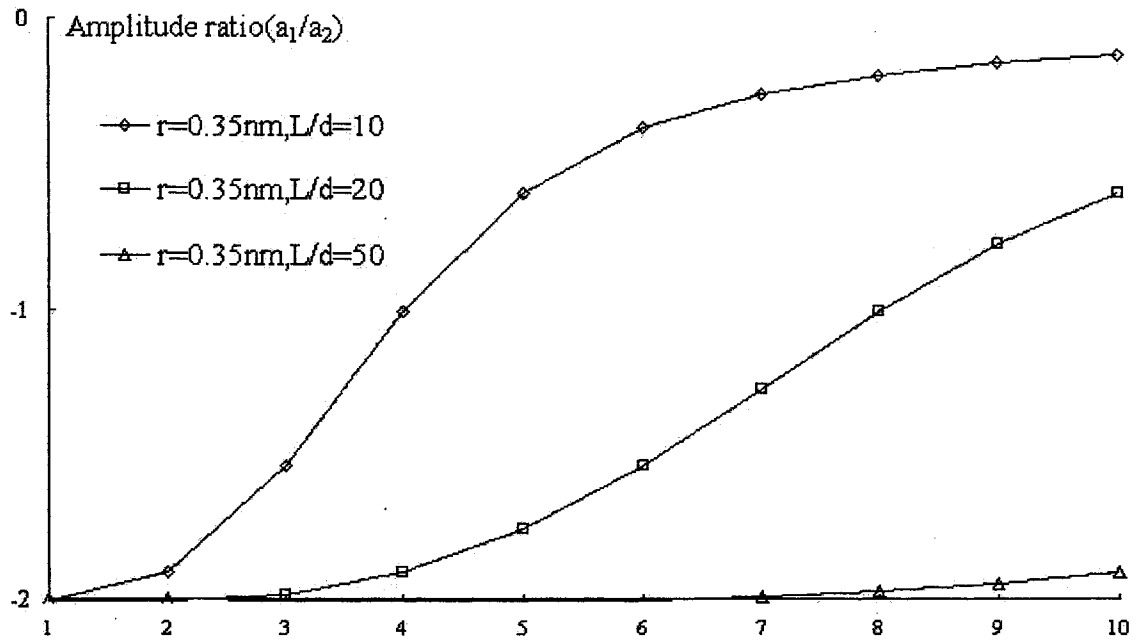

Fig. 5.8. DWNT amplitude ratio (a_1/a_2) for f_{n2} using a double-Timoshenko-beam model

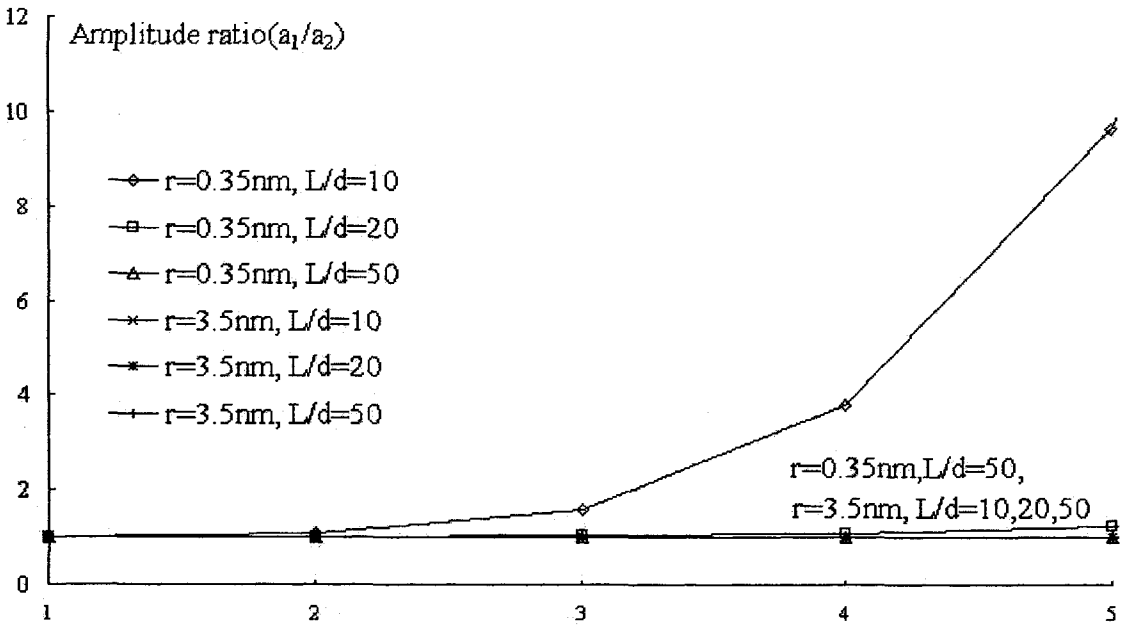

Fig. 5.9. DWNT amplitude ratio (a_1/a_2) for f_{n1} using a double-Euler-beam model

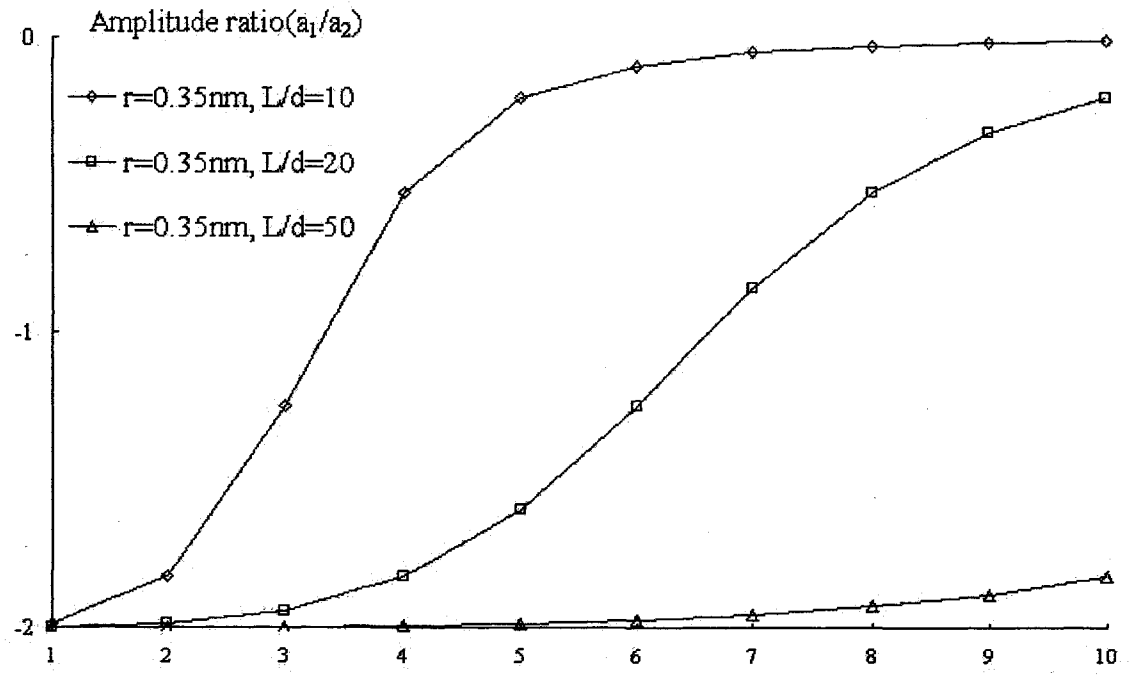

Fig. 5.10. DWNT amplitude ratio (a_1/a_2) for f_{n2} using a double-Euler-beam model

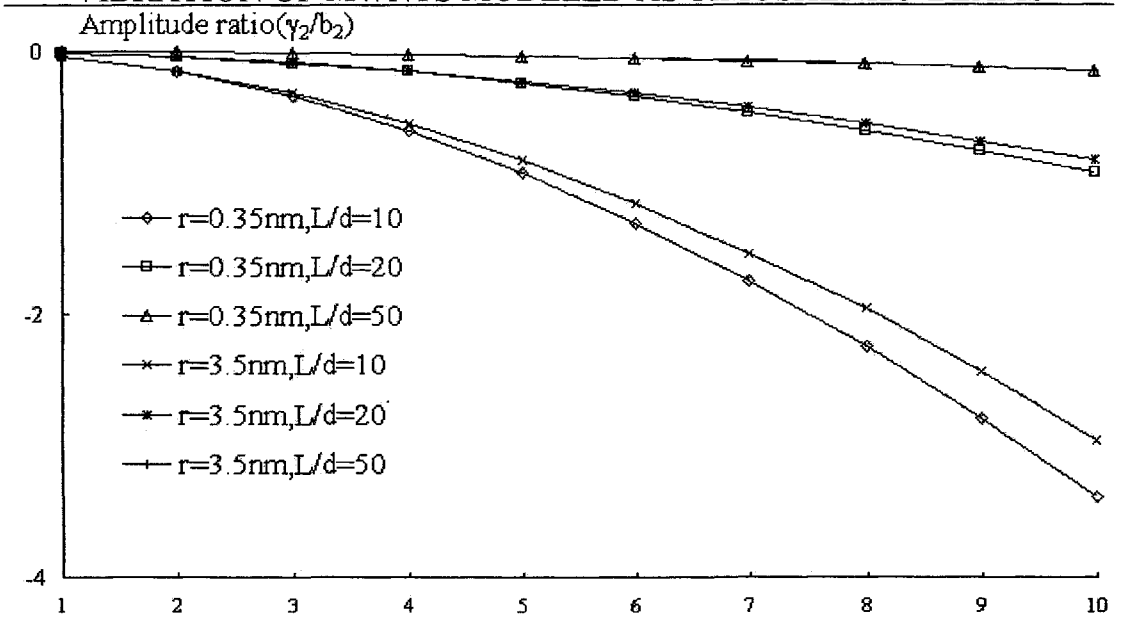

Fig. 5.11. DWNT amplitude ratio (γ_2/b_2) for f_{n1} using a double-Timoshenko-beam model

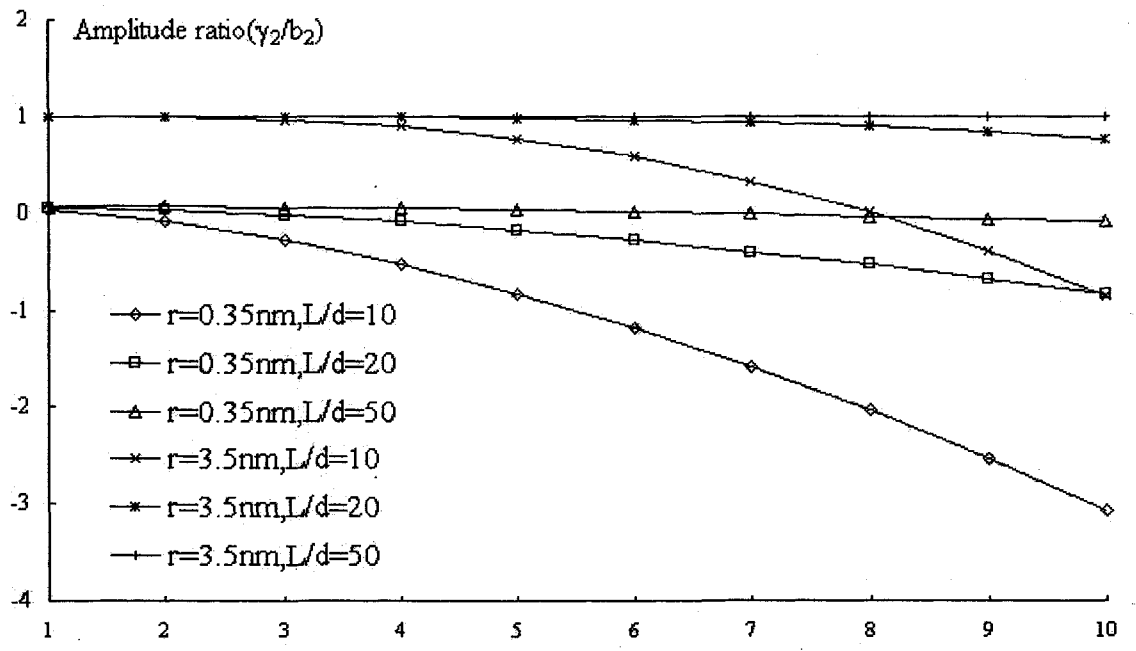

Fig. 5.12. DWNT amplitude ratio (γ_2/b_2) for f_{n2} using a double-Timoshenko-beam model

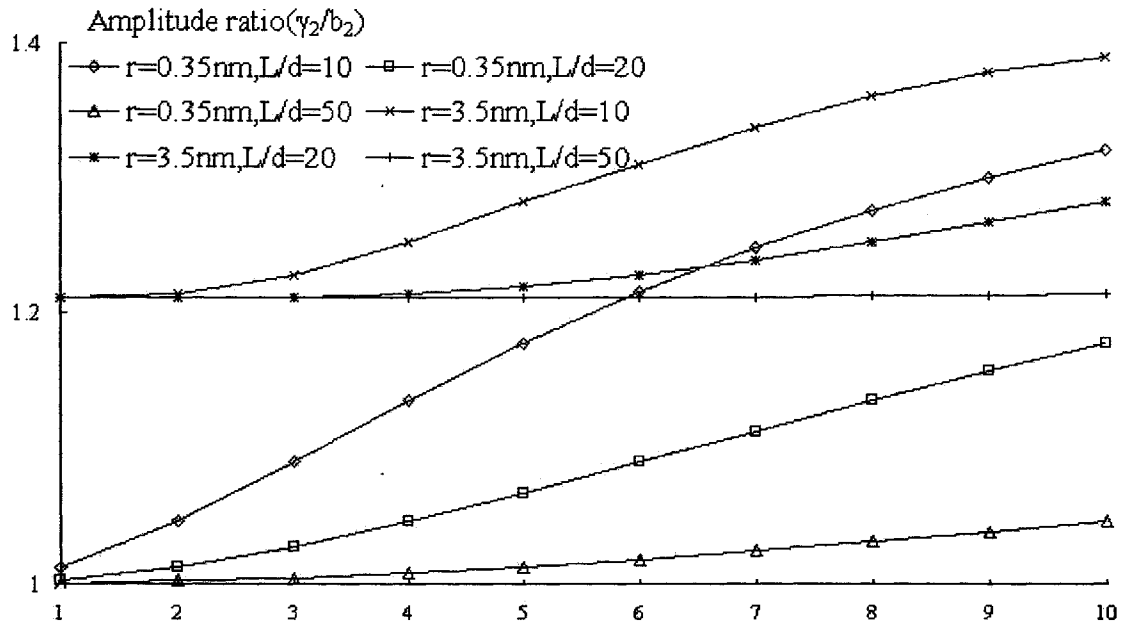

Fig. 5.13. DWNT amplitude ratio (γ_2/b_2) for f_{n3} using a double-Timoshenko-beam model

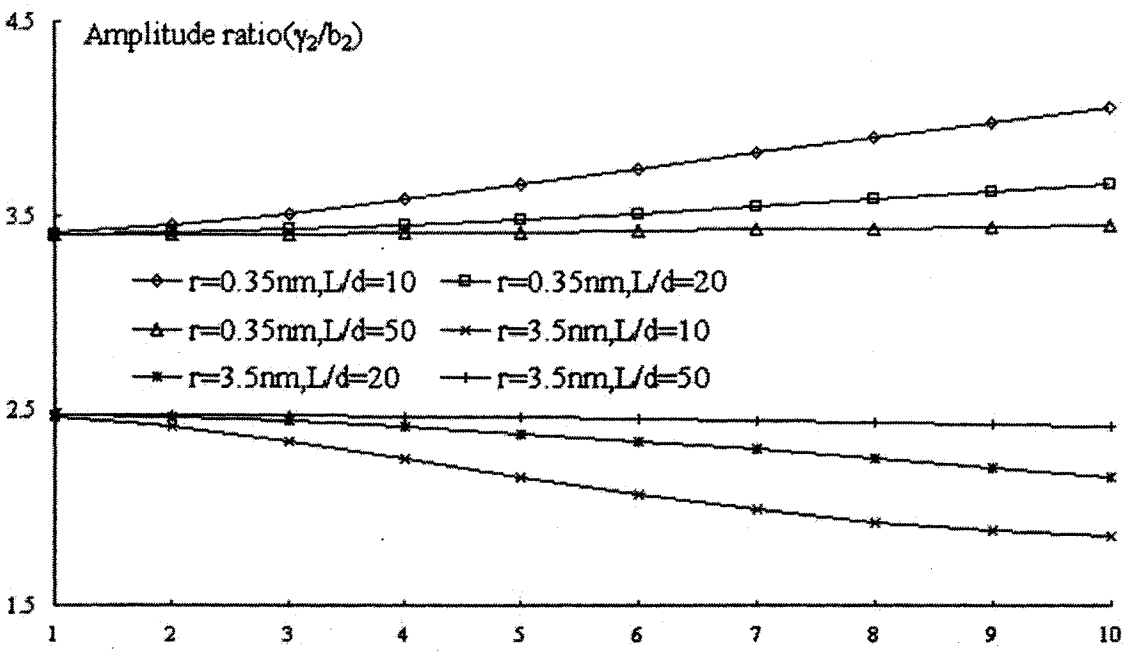

Fig. 5.14. DWNT amplitude ratio (γ_2/b_2) for f_{n4} using a double-Timoshenko-beam model

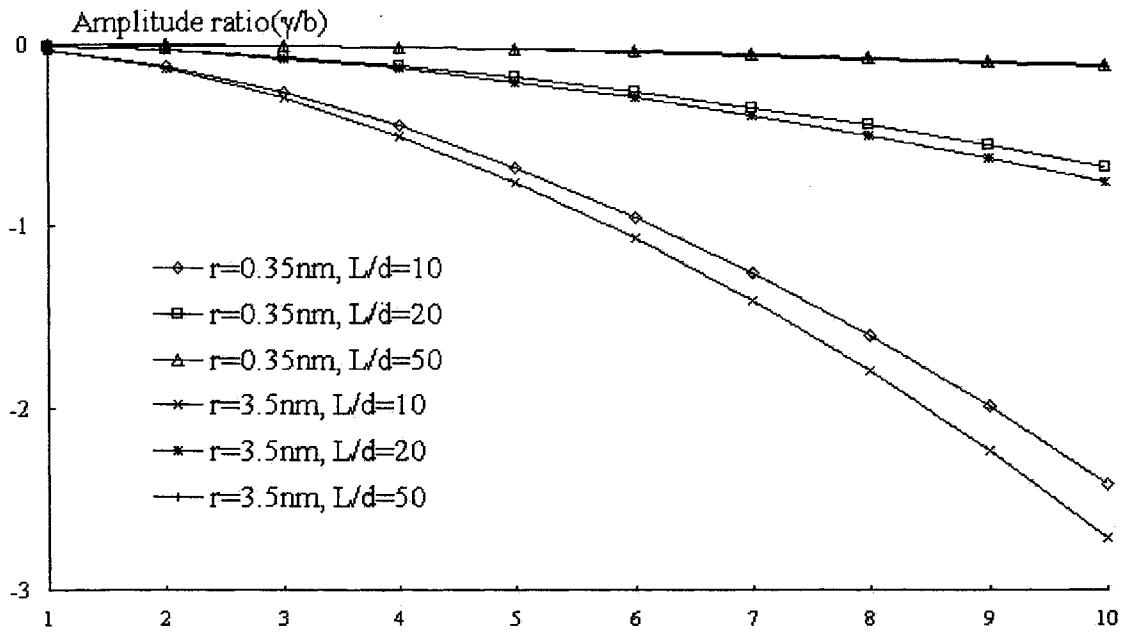

Fig. 5.15. DWNT amplitude ratio (γ/b) for f_{n1} using a single-Timoshenko-beam model

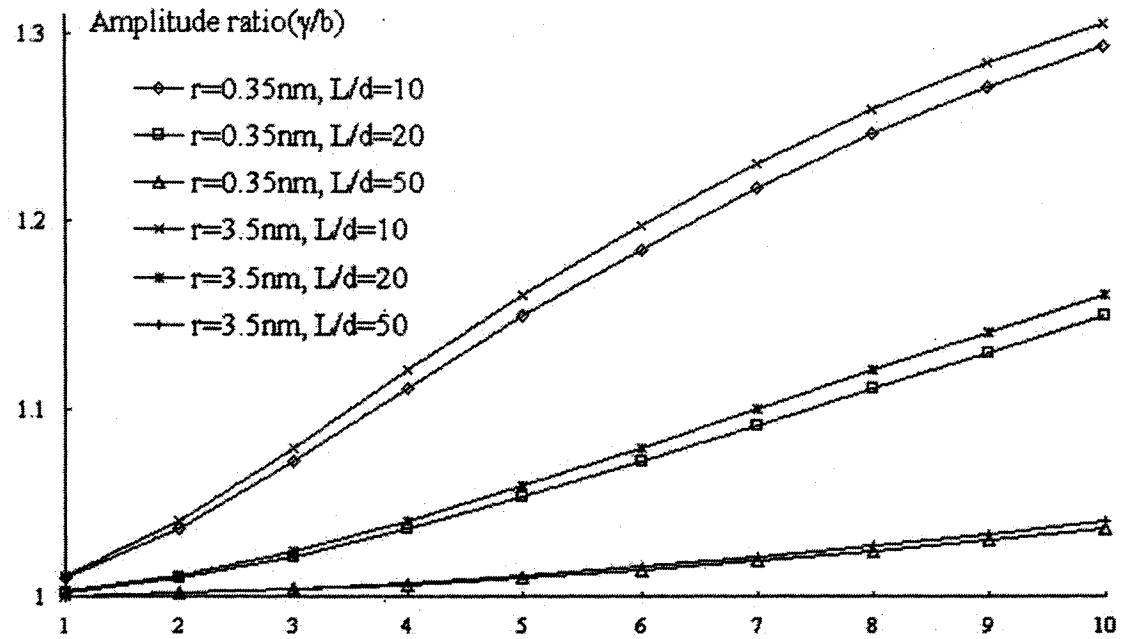

Fig. 5.16. DWNT amplitude ratio (γ/b) for f_{n2} using a single-Timoshenko-beam model

Chapter 6

Wave Propagation in MWNTs Modeled as Timoshenko-Beams

6.1 Introduction

The role of non-coaxial interlayer radial displacements in transverse vibration and wave propagation in MWNTs are studied. These results shows that non-coaxial intertube vibration and transverse waves of MWNTs will be excited at ultrahigh frequencies (above 1 THz), which would have substantial effects on both the natural frequencies and the wave speed of MWNTs. As discussed above, in the terahertz range, the characteristic wavelength of transverse waves in MWNTs would be just a few times the outermost diameter of MWNTs [72]. In this case, a relevant issue to be clarified is the effects of rotary inertia and shear deformation on transverse wave propagation of MWNTs. It is well-known that rotary inertia and shear deformation, which are ignored in the classic Euler-beam model, would become essential for transverse wave propagation of elastic beams at ultrahigh frequencies when the characteristic wavelength downs to just few times the diameter of the cross-section [79, 80, 109-111]. For this reason, the relevance of classic Euler-beam model to terahertz wave propagation in CNTs is questionable. In this Chapter, transverse wave propagation of individual DWNTs is studied based on the

double-Timoshenko-beam model developed in [74]. Unlike chapter 4, however, CNTs are modeled as Timoshenko-beams, instead of the classic Euler-beams. As will be shown below, the rotary inertia and shear deformation, incorporated by Timoshenko-beam model, do have a substantial effect on terahertz transverse wave propagation in CNTs. Therefore, Timoshenko-beam model, rather than the Euler-beam model, is more relevant for terahertz wave propagation in CNTs [73].

6.2 Double-Timoshenko-Beam Model for Wave Propagation

6.2.1 Determination of the Wave Speeds

To study transverse wave propagation, let us consider the deflection and the slope given by [80, 138]

$$\begin{aligned} Y_j &= a_j e^{i(qx-\omega t)} \\ \phi_j &= b_j e^{i(qx-\omega t)} \end{aligned} \quad , (j=1,2) \tag{6.1}$$

where a_1 and a_2 represent the amplitudes of deflections of the inner and the outer tubes, respectively, and b_1 and b_2 represent the amplitudes of the slopes of the inner and outer tubes due to bending deformation alone, respectively. In addition, q is the wave number, and ω is the (circular) frequency. The equation to determine the wave speeds can be obtained by substituting (6.1) to (5.1), with the result

$$\begin{bmatrix} KGA_1q^2+c-\rho A_1\omega^2 & iKGA_1q & -c & 0 \\ -iKGA_1q & EI_1q^2+KGA_1-\rho I_1\omega^2 & 0 & 0 \\ -c & 0 & KGA_2q^2+c-\rho A_2\omega^2 & iKGA_1q \\ 0 & 0 & -iKGA_1q & EI_2q^2+KGA_2-\rho I_2\omega^2 \end{bmatrix} \begin{bmatrix} a_1 \\ b_1 \\ a_2 \\ b_2 \end{bmatrix}$$

$$=0 \qquad (6.2)$$

The wave speeds are determined by the condition for existence of non-zero solution which gives

$$F(q^2, \omega) \equiv$$

$$\begin{aligned} &(EI_2q^2+KGA_2-\rho I_2\omega^2)\{-c^2(EI_1q^2+KGA_1-\rho I_1\omega^2) \\ &+(KGA_2q^2+c-\rho A_2\omega^2)[(KGA_1q^2+c-\rho A_1\omega^2)(EI_1q^2+KGA_1-\rho I_1\omega^2)-(KGA_1q)^2]\} \\ &-(KGA_2q)^2\{(KGA_1q^2+c-\rho A_1\omega^2)(EI_1q^2+KGA_1-\rho I_1\omega^2)-(KGA_1q)^2\} \\ &=0 \end{aligned} \qquad (6.3)$$

It is noticed that equation (6.3) is a fourth-order algebraic equation for q^2. It is anticipated that the present double-Timoshenko-beam model could give as many as four different wave speeds for a given frequency, in contrast to at most two wave speeds given by the single-Timoshenko-beam model [79, 80, 109-111], at most two wave speeds given by the double-Euler-beam model [72], and the single wave speed given by the single-Euler-beam model [80]. In particular, for the sake of comparison, the single transverse wave speed of a MWNT based on single-Euler-beam model is given by Eq. (2.7), where I and A are the total moment of inertia and the cross-sectional area of MWNT. Thus, $I=I_1+I_2$ and $A=A_1+A_2$ for a DWNT.

WAVE PROPAGATION IN MWNTS MODELED AS TIMOSHENKO-BEAMS

In what follows, the wave speed (phase velocity=ω/q) is calculated based on four different elastic beam models:

(DT): the double-Timoshenko-beam (DT) model described by (6.3) which gives at most four wave speeds for given frequency, $v_1<v_2<v_3<v_4$;

(DE): the double-Euler-beam (DE) model described in [72] which treats each of the inner and outer tubes of the DWNT as a single-Euler-beam and gives at most two wave speeds for given frequency, $v_1<v_2$;

(ST): the single-Timoshenko-beam (ST) model which treats the DWNT as a single Timoshenko-beam, with $I=I_1+I_2$ and $A=A_1+A_2$, and gives at most two wave speeds for given frequency, $v_1<v_2$;

(SE): the single-Euler-beam (SE) model, which gives the single wave speed (v_0) for given frequency (2.7).

The wave speeds given by different models are distinguished by (DT), (DE), (ST) or (SE), when necessary. Obviously, the number of the wave speeds, which are defined by ω/k, is equal to the number of positive roots of equation (6.3). The function $F(p^2, \omega)$ is illustrated in Figs. 6.1 and 6.2 for DWNTs of diameter 0.7 nm and 7 nm respectively. It is seen from Figs. 6.1 and 6.2 that for very low frequency, $F(q^2, \omega)$ has only one positive root for q^2, which implies that there is only one transverse wave speed for very low frequency. On the other hand, when frequency is extremely high, there are four different positive roots for q^2, and thus four distinct transverse wave speeds exist for extremely high frequency. When the frequency is between the two extreme cases, the number of wave speeds varies between one and four, depending on the

frequency and the diameter of DWNTs.

6.2.2 Transverse Wave Speeds and associated amplitude ratios

All different wave speeds given by the four different models are shown in Figs. 6.3 and 6.4 for a DWNT of the inner diameter 0.7nm or 7nm, respectively. It is found from Figs. 6.3 and 6.4 that there exist several critical frequencies for any given DWNT. In contrast to the SE, ST, DE model, which has a fixed number of wave speeds, the number of the critical frequencies based on DT model may depend on the diameters of DWNTs. For example, there are 3 critical frequencies for DWNT of diameter 7nm, and 4 critical frequencies for DWNT of diameter 0.7 nm. When the frequency is far below the lowest critical frequency, only one speed exists which is quite close to the single wave speed given by the single-Euler-beam model (2.7). The effect of Timoshenko-beam on the wave speed becomes significant even when the frequency is below but close to the lowest critical frequency. For example, it is seen from Fig. 6.4 that the wave speeds given by SE and DE models are about 50% higher than that given by ST and DT models around the lowest critical frequency. When the frequency is higher than at least one of the critical frequencies, there are at least two different sound speeds, which are significantly different from the wave speed (2.7) given by the single-Euler-beam model. Therefore, the single-Euler-beam model, which has been successfully applied to sound wave propagation in SWNTs [72], is applicable for DWNTs only at relatively low frequencies, but fails at ultrahigh frequencies.

Inner radius (nm)	Model	Critical frequency (THz)
0.35	DT	$\omega^* = 6.0307$ $\omega_1 = 6.0396$ $\omega_2 = 23.11$ $\omega_3 = 42.63$
	ST	$\omega_{ST} = 26.43$
	DE	$\omega_{DE} = 6.0396$
3.5	DT	$\omega_1 = 4.325$ $\omega_2 = 4.763$ $\omega_3 = 6.813$
	ST	$\omega_{ST} = 4.518$
	DE	$\omega_{DE} = 6.813$

Table 6.1 Critical frequencies given by different models in a DWNT.

The critical frequencies and the number of different wave speeds are shown in Table 6.1 and Table 6.2, respectively, for DWNTs of diameter 0.7 nm or 7 nm. For instance, the lowest critical (circular) frequency is 6.0307 THz or 4.325 THz, when the inner diameter of the DWNT is 0.7nm or 7nm, respectively. In particular, the Timoshenko-beam model has a crucial effect on the lowest critical frequency for large-radius MWNTs. Indeed, it is seen from Table 6.1 that the lowest critical (circular) frequency given by DT model for inner radius 3.5nm, 4.325 THz, is much lower than that given by DE model, which is 6.813

THz. Here, we would mention that the real frequency f (=$\omega/2\pi$) is about 6 times lower than the circular frequency ω.

Inner radius (nm)	Frequency (ω)	Number of sound wave speeds
0.35	$\omega < \omega^*$	1
	$\omega = \omega^*$	2
	$\omega^* < \omega < \omega_1$	3
	$\omega_1 \leq \omega < \omega_2$	2
	$\omega_2 \leq \omega < \omega_3$	3
	$\omega_3 \leq \omega$	4
3.5	$\omega < \omega_1$	1
	$\omega_1 \leq \omega < \omega_2$	2
	$\omega_2 \leq \omega < \omega_3$	3
	$\omega_3 \leq \omega$	4

Table 6.2 The number of sound wave speeds given by the double-Timoshenko-beam model in a DWNT.

In particular, when the frequency is extremely high, the present double-Timoshenko-beam model predicts four different wave speeds, $v_1<v_2<v_3<v_4$. However, v_1 is very close to v_2, while v_3 is very close to v_4. In addition, the two asymptotic wave speeds for extremely high frequencies are very close to the two wave speeds given by the single-Timoshenko-beam model for extremely high frequencies as follows [80]

$$v_{a1} = \sqrt{\frac{GK}{\rho}}, \quad v_{a2} = \sqrt{\frac{E}{\rho}} \tag{6.4}$$

Inner radius (nm)	Model	Asymptotic transverse wave speeds (m/s)
0.35	DT	v_1=11790 v_2=11794 v_3=20860 v_4=20880
	ST	v_1=11795 v_2=20851
3.5	DT	v_1=11795 v_2=11795 v_3=20851 v_4=20851
	ST	v_1=11795 v_2=20851

Table 6.3 Asymptotic transverse wave speeds for extremely high frequencies.

All these wave speeds are shown in Table 6.3. Since the two asymptotic speeds (6.4) are independent of the geometry of the cross-section, the four speeds given by DT model for extremely high frequencies are independent of the inner radius and the outer radius, and approach the two speeds (6.4), respectively.

Finally, the amplitude ratio of the inner tube deflection to the outer tube

deflection, given by the DT and DE models, is shown in Figs. 6.5 and 6.6, for diameter 0.7 nm and 7 nm, respectively. It is seen from Figs. 6.5 and 6.6 that when the frequency is far lower than the lowest critical frequency, the amplitude ratio a_1/a_2 is very close to unity, indicating that the vibrational mode is almost coaxial. However, the amplitude ratio a_1/a_2 could significantly deviate from unity when the frequency is below but close to the lowest critical frequency. This phenomenon is substantial especially for small radius DWNTs. Indeed, it is seen from Fig. 6.5 that the amplitude ratio a_1/a_2 is as large as 3 or 5 around the lowest critical frequency for DWNT of inner radius 0.35nm. This indicates that, in contrast to the Timoshenko-beam effects which are more significant for large-radius than small-radius CNTs, non-coaxial modes incorporated by double-beam (DT, DE) models are more relevant for small-radius than large-radius CNTs. On the other hand, when the frequency exceeds at one of the critical frequencies, the amplitude ratio a_1/a_2 is no longer close to unity, or even becomes negative, which indicates that the vibrational modes are substantially non-coaxial. In these cases, the existing single-beam model fails, and the double-beam models (DT, DE) are required to account for the role of intertube radial displacements.

6.3 Summary

In summary, sound wave propagation in DWNTs is studied based on a double-Timoshenko-beam model. It is found that there are a few (say, 3 or 4, depending on the diameters) terahertz critical frequencies for a DWNT at which

the number of wave speeds changes. Sound wave propagation in DWNTs is essentially coaxial and Timoshenko-beam effects are negligible only when the frequency is far below all critical frequencies. When the frequency is close to or higher than the lowest critical frequencies, rotary inertia and shear deformation, incorporated by Timoshenko-beam model, have a substantial effect on the wave speeds especially for MWNTs of larger radii. In this case, the sound speeds predicted by the present model are significantly higher or lower than that given by the existing single-Euler-beam model, and depend not only on the frequency but also on the vibrational modes. In particular, Timoshenko-beam effects significantly lower the value of the lowest critical frequency especially for MWNTs of larger radii. More recently, atomistic simulation [97] shows that Timoshenko-beam model would be effective even for wavelengths down to about 1 nm, which confirms the effectiveness of the elastic beam model. Hence, Timoshenko-beam model is more relevant for terahertz wave propagation in CNTs.

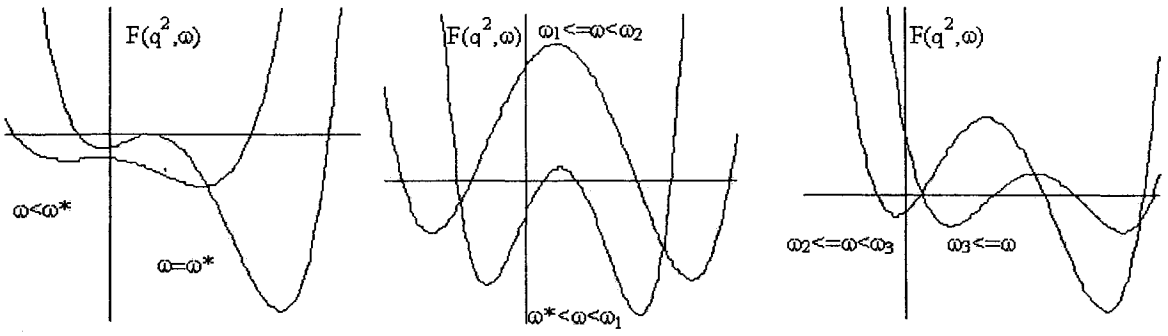

Fig. 6.1. The function $F(q^2, \omega)$ which determines the number of the wave speeds for given frequency in a DWNT (inner radius 0.35nm).

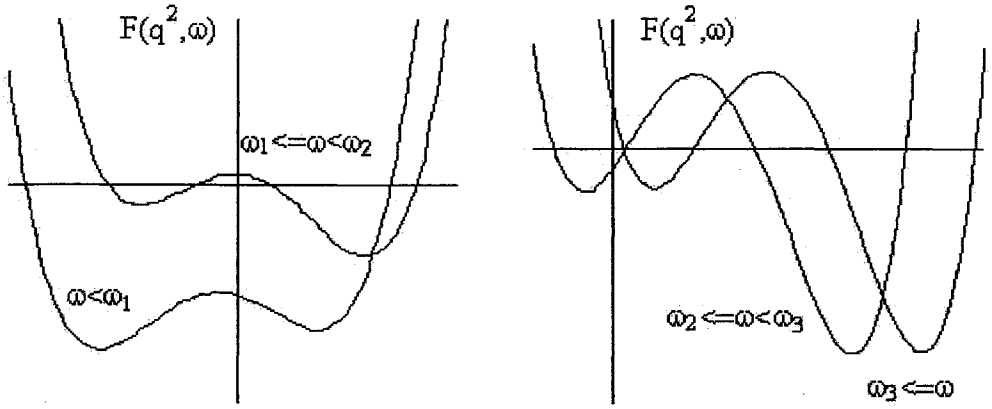

Fig. 6.2. The function $F(q^2, \omega)$ which determines the number of the wave speeds for given frequency in a DWNT (inner radius 3.5nm).

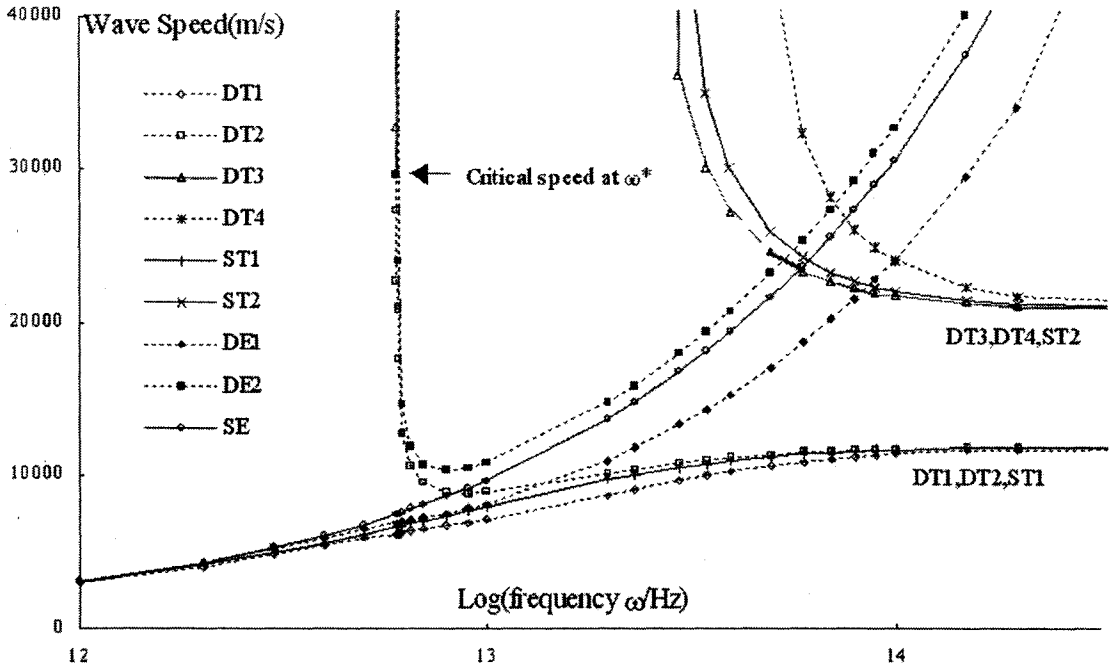

Fig.6.3. The wave speeds as function of frequency in a DWNT (inner radius 0.35nm)

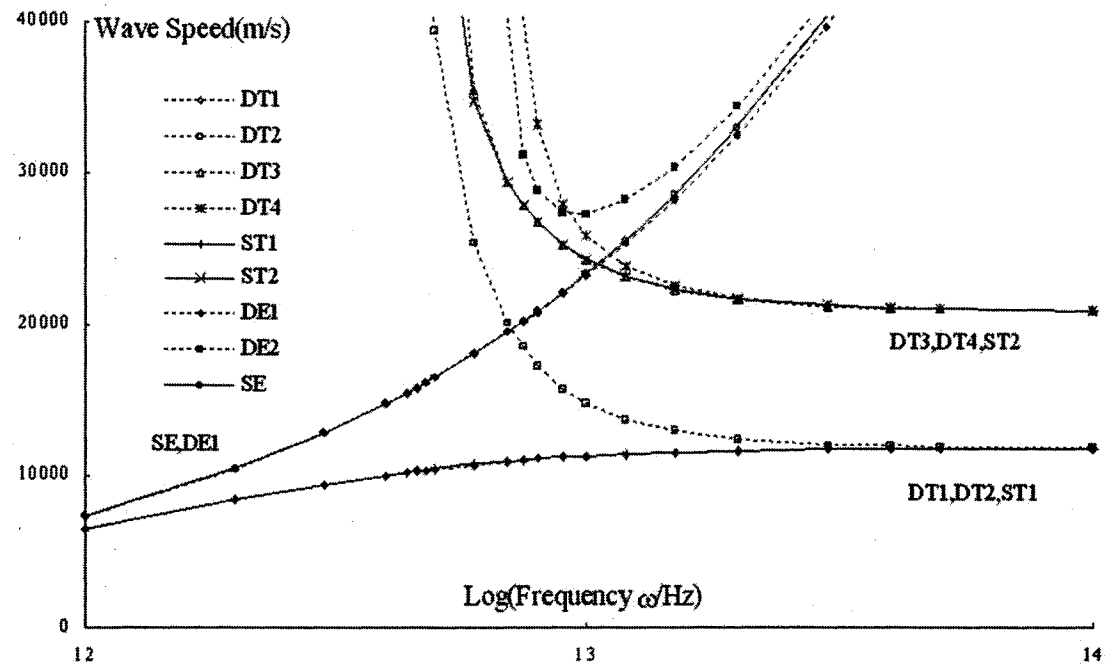

Fig.6.4. The wave speeds as function of frequency in a DWNT (inner radius 3.5nm)

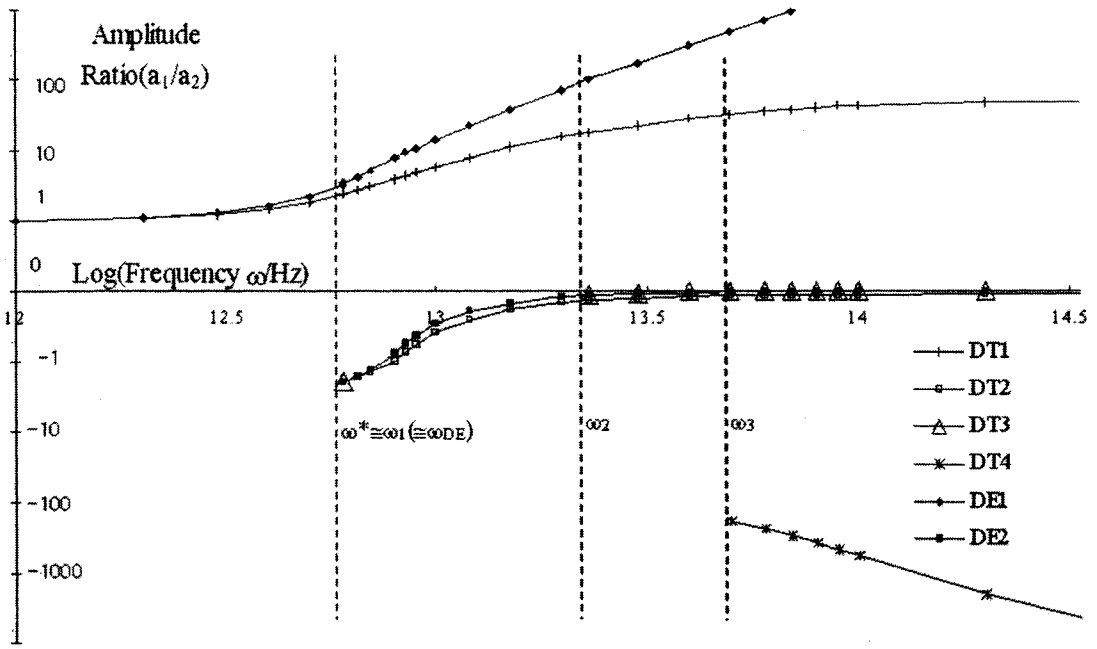

Fig.6.5. The amplitude ratio of the inner-tube deflection to the outer-tube deflection of a DWNT (inner radius 0.35nm)

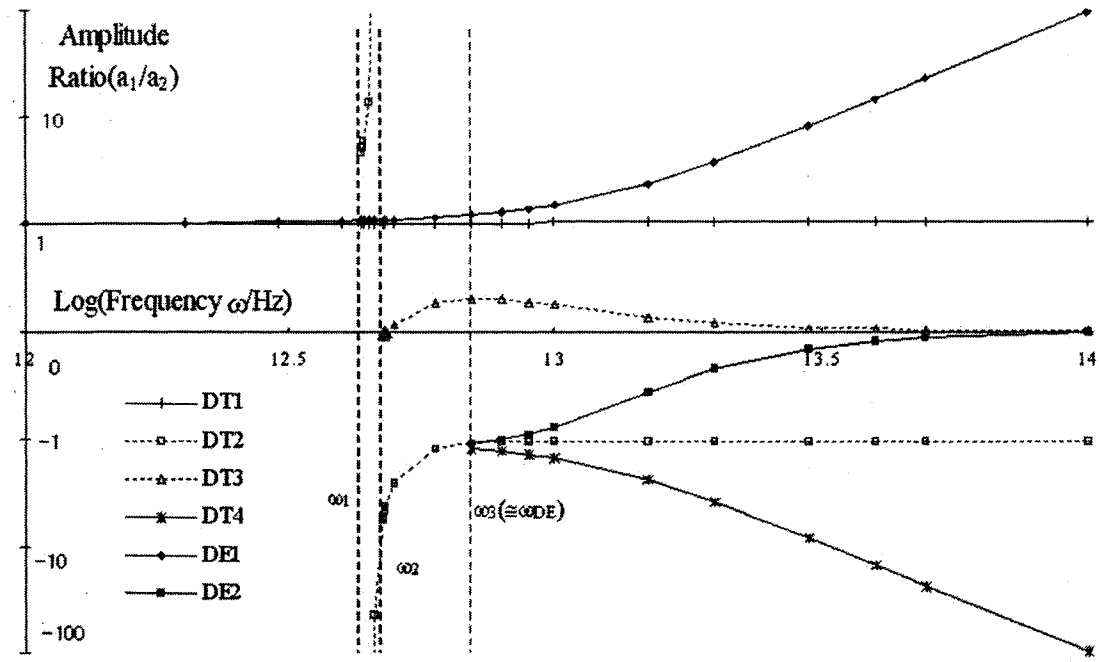

Fig.6.6. The amplitude ratio of the inner-tube deflection to the outer-tube deflection of a DWNT (inner radius 3.5nm)

Chapter 7

Vibration and Instability of CNTs Conveying Fluid

7.1 Introduction

Because of perfect hollow cylindrical geometry and superior mechanical strength, CNTs hold substantial promise as nanocontainers for gas storage, and nanopipes for conveying fluid (such as gas or water) [52, 53, 139-143]. Fluid flow inside CNTs raises a significant and challenging research topic [144-151]. On the other hand, the influence of internal moving fluid on overall mechanical behavior of CNTs is another topic of major concern. The present chapter examines the effects of internal moving fluid on free vibration and structural instability of CNTs conveying fluid. These interesting issues remain unexplored in the literature.

Fluid mechanics of flow within CNTs aims to study how the wall-fluid interaction and the viscosity of fluid affect velocity distribution, and how the velocity distribution depends on the applied pressure gradient in a non-classic way [144-151]. Since our goal is not to study fluid mechanics inside CNTs, we shall assume, instead, that a uniform steady-state flow is achieved throughout a straight CNT, with a constant and uniform (mean) flow velocity defined by the flow flux divided by the innermost cross-sectional area (Here, it is noted that

the uniformity of flow velocity throughout the entire CNT is a simple consequence of the uniform cross-section, if the fluid is assumed to be incompressible). Thus, the role of the internal fluid in the present study is characterized by two parameters, the (mean) flow velocity V and the mass density of fluid M (per unit axial length), and the wall-fluid interaction and the viscosity of fluid, which affect the velocity distribution and the mean flow velocity V, will not explicitly appear in the present study. In other words, the role of the wall-fluid interaction and the viscosity of fluid is the wall-fluid interaction and the viscosity of fluid is considered here only implicitly through their influence on the mean flow velocity. Therefore, we shall focus on the effects of internal flow of the mean flow velocity V on vibration and structural instability of CNTs, without concerning how the wall-fluid interaction and the viscosity of fluid affect the mean flow velocity and what external pressure gradient is needed to achieve such a flow within CNTs.

In addition, as discussed in previous Chapters, continuum elastic beam models [37, 38, 55, 64-78] have been effectively used to study static and dynamic structural behavior of CNTs, such as static deflection [38], column buckling [77], resonant frequencies and modes [37, 55], and sound wave propagation [78]. Since the elastic beam models enjoy very simple mathematical formulas, they have the potential to identify the key parameters affecting basic mechanical behavior of CNTs (and thus rule out other less important parameters), explain or predict new physical phenomena, and stimulate and guide further experiments and molecular dynamics simulations.

Based on these ideas, the present chapter studies the effects of internal moving fluid on free vibration and structural instability of CNTs conveying fluid[75]. Here, the structural behavior of CNTs is described by the classic Euler-beam model, and the role of internal moving fluid is characterized by two parameters, the mean flow velocity V and the mass density of fluid M (per unit axial length), as shown in Fig. 7.1. In addition, CNT is assumed to be simply supported or clamped at both ends, with or without being embedded into an elastic medium such as polymer.

7.2 The Model for CNTs Conveying Fluid

As shown in Fig. 7.1, a CNT conveying fluid will be described as an elastic hollow tube conveying fluid. Here, as usual, we shall neglect gravity effect and assume that the constraint for axial displacement of CNT is absent or negligible. Thus, let the mean flow velocity and the mass density (per unit axial length) of the fluid be V and M, respectively, vibration and structural instability of a CNT conveying fluid can be described by the model [152-154]

$$EI\frac{\partial^4 w}{\partial x^4}+\left(MV^2+p^*A-T^*\right)\frac{\partial^2 w}{\partial x^2}+2MV\frac{\partial^2 w}{\partial x\partial t}+\left(M+m\right)\frac{\partial^2 w}{\partial t^2}+kw=0 \qquad (7.1)$$

where x is the axial coordinate, t is time, w(x,t) is the deflection of the CNT, E and I are Young's modulus and the moment of inertia of the cross-section of the CNT, A is the area of the innermost cross-section of the CNT, m is the mass of CNT per unit axial length (which is equal to the cross-sectional area of CNT

itself multiplied by the mass density of CNTs), k is the Winkler constant of the surrounding elastic medium described as a Winkler-like elastic foundation [71, 153, 154], and T^* and p^* are the externally applied tension (on CNT) and global pressure (exerted on fluid equally at both ends of CNT). As explained in [153, 154] for elastic tubes, regardless of the details of the wall-fluid interaction and the viscosity of fluid, the sum (pA-T), where T and p are the tension (on CNT) and pressure (exerted on fluid) along the tube, remains constant throughout the whole tube even though the tension T and pressure p individually vary along the tube. It follows that (pA-T) in (5.1) can be replaced by its value (p^*A-T^*) at any one of the two ends. In particular, $p^*=T^*=0$ if both the applied external tension and the global pressure are zero at one end of CNT.

Here, it is stressed that the role of internal moving fluid is characterized by two parameters of the fluid, its mass density M and the mean flow velocity V (the latter is defined by the flow flux divided by the area of the innermost cross-section of CNT). The complicated wall-fluid interaction and the viscosity of fluid affect vibration and instability of CNT only through affecting the velocity distribution and the mean flow velocity, but will not explicitly appear in the governing equation (5.1). Hence, the present model focuses on the effects of internal moving fluid on vibration and instability of CNTs, and does not study how the wall-fluid interaction and the viscosity of fluid affect the mean flow velocity V and what applied pressure gradient is required to achieve such a flow inside CNTs.

7.2.1 Vibrational Frequencies

First, we examine the effect of internal flow on vibrational frequencies of CNTs conveying fluid. Let us apply Galerkin procedure [152, 154] and expand the vibrational deflection w(x,t) as

$$w(x,t) = \sum_{r=1}^{N} Y_r(x) q_r(t) \tag{7.2}$$

where N is a chosen sufficiently large integer, $q_r(t)$ are undetermined time-dependent functions, and $Y_r(x)$ are the first N vibrational modes of Eq.(1) with V=0, $p^*A=T^*$, and under the specified BCs. Obviously, expression (7.2) always satisfies the given BCs for any nonzero value of V. Following the standard procedure of the Galerkin method, substitution of (7.2) into Eq. (7.1) leads to N coupled second-order ordinary differential equations for N unknown time-dependent functions $q_r(t)$ (r=1,2,...N)

$$\sum_{r=1}^{N}\left\{\left(\frac{M+m}{EI}\int_0^L Y_s Y_r dx\right)\frac{\partial^2 q_r}{\partial t^2}+\left(2\frac{MV}{EI}\int_0^L Y_s\frac{\partial Y_r}{\partial x}dx\right)\frac{\partial q_r}{\partial t}\right.$$
$$\left.+\left((\lambda_r^4+\frac{k}{EI})\int_0^L Y_s Y_r dx+(\frac{MV^2+p^*A-T^*}{EI})\int_0^L Y_s\frac{\partial^2 Y_r}{\partial x^2}dx\right)q_r\right\}=0 \tag{7.3}$$

(s = 1,2,....N)

where λ_r is eigenvalue associated with $Y_r(x)$ under the given boundary conditions.

The system (7.3) has N conjugate pairs of eigen-values, which determine

the first N vibrational frequencies of the CNT described by (7.1). These eigenvalues can be obtained by substituting $q_r(t)=A_r e^{i\omega t}$ into (7.3), where A_r is the amplitude coefficient and ω is the circular frequency. The accuracy of the method usually increases with increasing number N. For our purposes, it is enough to consider N=5. It turns out that this method is sufficiently accurate when the flow velocity is below or up to the critical flow velocity in some cases, or just a fraction of the critical flow velocity in other cases. In this paper, we shall confine ourselves to the effect of internal moving fluid on the two lowest resonant frequencies of the CNT.

Here, we first consider the case in which the CNT are simply supported at both ends. In this case, the vibrational modes of (7.1) when V=0 and under BCs are of the simple form

$$Y_r = \sin\left(\frac{r\pi x}{L}\right) \tag{7.4}$$

where L is the length of CNT. In both cases k=0 (suspended CNTs) and k>0 (embedded CNTs surrounded by an elastic medium), the first N modes of (1) when V=0 are given by (7.4) for r=1,2,...N.

The examples of CNTs considered here include: I) MWNT with R_{out}=50nm and t=10nm; and II) MWNT with R_{out}=40 nm and t=20 nm [144], where R_{out} is the outermost radius, and t is the thickness of CNTs defined as the difference between the outermost and the innermost radii. Here, three different

aspect ratios of CNTs, $(L/2R_{out})$=20, 100 and 500 are considered. On the other hand, to be specific, water will be considered as the fluid moving inside CNTs. The mass density of CNTs is 2.3g/cm^3 with Young's modulus E of 1 TPa, and the mass density of water is 1g/cm^3. In addition, the Winkler-constant is based on polymer matrix [71] and estimated of the value of k=1 GPa. Finally, the available data in the literature for flow velocity inside CNTs range from 400m/s [150] to 2000m/s [151], or even up to 50000m/s [146]. Therefore, to cover a wide range of flow velocity inside CNTs of various innermost diameters, we shall artificially consider the flow velocity V up to 100000m/s, in spite of the fact that the available data for flow velocity of water inside CNTs (of very small innermost diameter) are much lower than this value.

In what follows, the resonant frequencies $f=\omega/(2\pi)$ of simply supported CNTs conveying fluid are calculated and shown in Figs. 7.2-7.7 for the two cases defined above, with or without a surrounding elastic medium. Since we are mainly interested in the effect of internal moving fluid, it is assumed in Figs. 7.2-7.7 that the external global pressure p^* and tension T^* at the ends are zero. It is seen from Figs. 7.2-7.7 that:

1) Resonant frequencies of simply supported CNTs conveying fluid decrease parabolically with the flow velocity of internal moving fluid. This phenomenon is common for examples I and II, especially for suspended CNTs without a surrounding elastic medium, as shown in Figs. 7.2-7.4. As the flow velocity increases, the lowest frequency reduces to zero at a critical flow velocity where a static structural instability characterized by adjacent neutral equilibrium states

occurs. All of these conclusions qualitatively agree with the results of elastic tubes conveying fluid [152-154].

2) In the absence of a surrounding elastic medium, the results of Figs. 7.2-7.4 indicate that the internal moving fluid has a substantial effect on the lowest resonant frequencies of CNTs. This effect is relatively insignificant for CNTs of smaller aspect ratio (such as $L/2R_{out}$=20, as shown in Fig. 7.2) at lower flow velocity, but becomes crucial at higher flow velocity even for CNTs of smaller aspect ratio, and for CNTs of larger aspect ratio (such as $L/2R_{out}$=100 or 500, as shown in Figs. 7.3 and 7.4) even at lower flow velocity. For instance, the lowest frequency of CNTs of aspect ratio 20 for examples I and II decreases by 50% when the flow velocity V is 1020m/s and 2060m/s, respectively, and becomes zero when the flow velocity V reaches the critical value 1190m/s and 2380m/s, respectively. On the other hand, the lowest frequency of CNTs of aspect ratio 500 for examples I and II decreases by 50% when the flow velocity V is 41m/s and 83m/s, respectively, and becomes zero when the flow velocity V reaches the critical value 48m/s and 96m/s, respectively. Therefore, the influence of internal moving fluid on resonant frequencies becomes crucial especially for suspended CNTs of larger aspect ratio at higher flow velocity.

3). However, the results of Figs. 7.5-7.7 indicate that even a compliant surrounding elastic medium (such as polymer) has a significant effect to reduce the sensitivity of resonant frequencies to the internal flow velocity V. The role of a surrounding elastic medium becomes significant especially for CNTs of larger aspect ratio, such as those shown in Figs. 7.6 and 7.7. For example, for

the examples I and II with k=1GPa, the lowest frequency of CNTs of aspect ratio 20 (see Fig. 7.5) decreases by 50% when the flow velocity V is 3630m/s and 7300m/s, respectively. On the other hand, the change of the lowest frequency of embedded CNTs of aspect ratio 100 or 500 (see Figs. 7.6 and 7.7) is smaller than 23% and 1% when the flow velocity V is up to 4000m/s and 1500m/s, respectively. Therefore, even a compliant surrounding elastic medium can significantly reduce the influence of the internal moving fluid on resonant frequencies of CNTs of larger aspect ratio.

Next, let us consider a clamped CNT, which is clamped at both ends without constraint for axial displacement. In this case, the first N vibrational modes of (7.1) with V=0 are not as simple as expression (7.4), and will not be shown here. The resonant frequencies $f=\omega/(2\pi)$ of clamped CNTs conveying fluid are calculated and shown in Figs. 7.8-7.13 for CNTs of various aspect ratios, under the condition $p^*=T^*=0$. Comparison between Figs. 7.2-7.7 and Figs. 7.8-7.13 indicates that all results obtained above for simply supported CNTs remain essentially the same for clamped CNTs. However, the influence of internal flowing fluid on resonant frequencies of clamped CNTs is generally less than that of simply supported CNTs under otherwise identical conditions. For example, Figs 7.2 and 7.8 indicate that the lowest resonant frequency of a simply-supported CNT of aspect ratio 20 decreases 50% for examples I and II when the flow velocity is 1020m/s and 2060m/s, respectively, although the lowest resonant frequency of a clamped CNT of aspect ratio 20 decreases 50% for examples I and II when the flow velocity is 1990m/s and 4130m/s,

respectively. Hence, resonant frequencies of clamped CNTs are less sensitive to the internal moving fluid than those of simply supported CNTs under other identical conditions.

7.2.2 Critical Flow Velocity and Critical Global Pressure

As mentioned above, the lowest frequency of a simply supported or clamped CNT reduces to zero when the flow velocity reaches a critical value. The vanishing frequency implies the existence of adjacent neutral equilibrium states and indicates a static structural instability of CNTs. In other words, a simply supported or clamped CNT undergoes a static structural instability (buckling) when the flow velocity reaches a critical value at which the lowest frequency vanishes. This critical flow velocity depends on the geometry of CNTs, the end conditions and the surrounding elastic medium. The mode of structural instability could be the same as the first vibrational mode of (7.1) with V=0 in some cases (such as suspended CNTs without a surrounding elastic medium), or quite different from any one of the first few vibrational modes of (7.1) with V=0 in other cases (particularly, in the presence of a surrounding elastic medium). In the former case, we have considered the flow velocity up to the critical flow velocity (see Figs. 7.2-7.5, 7.8-7.11). In the latter case, we only considered lower flow velocity (below a fraction of the critical flow velocity) for which the vibrational mode with V>0 can be well described by the first few vibrational modes for V=0 (see Figs. 7.6,7.7, and 7.12,7.13).

Although the dependency of resonant frequencies on the flow velocity

requests numerical calculation, simple general formula is available for the critical flow velocity in some typical cases, which helps to examine the dependency of the critical flow velocity on other parameters such as the aspect ratio of CNTs, the Winkler constant, and the mass density of the fluid. In fact, when the global pressure $p^*=0$, the critical flow velocity can be determined by static buckling analysis of (7.1) [153, 154], which leads to a simple critical flow velocity formula

$$V_c = \frac{r\pi}{L}\sqrt{\frac{EI}{M}\left(1+\frac{kL^4}{EI(r\pi)^4}\right)} \tag{7.5}$$

for simply-supported CNTs, where r is the mode number defined by (7.4) and should be chosen to minimize the critical flow velocity (7.5). The critical flow velocity formula for clamped CNTs is [153]

$$V_c = \frac{2\pi}{L}\sqrt{\frac{EI}{M}\left(1+\frac{3kL^4}{16\pi^4 EI}\right)} \qquad \text{for } k \le \frac{84}{11}\frac{\pi^4}{L^4}EI;$$

$$V_c = \frac{\pi}{L}\sqrt{\frac{EI}{M}\left(\frac{r^4+6r^2+1}{r^2+1}+\frac{kL^4}{(r^2+1)\pi^4 EI}\right)} \qquad \text{for } k \ge \frac{84}{11}\frac{\pi^4}{L^4}EI \tag{7.6}$$

where r is the mode number and should be determined as the smallest integer satisfying (7.7).

$$r^4 + 2r^3 + 3r^2 + 2r + 6 \geq \frac{kL^4}{\pi^4 EI} \tag{7.7}$$

The formulas (7.5) and (7.6) are shown in Figs. 7.14 and 7.15, respectively, for various radii of CNTs and for water and helium (the mass density of the latter is 0.137g/cm^2). Comparing Figs. 7.14, 7.15 with the results of Figs. 7.2-7.4, 7.8-7.10 indicates that the critical flow velocity given by (7.5, 7.6) through static buckling analysis is identical to the critical flow velocity given by vibration analysis at which the lowest frequency vanishes. For example, the CNT of case I ($L/2R_{out}$ = 500) with k=0 will buckle when the internal flow velocity reaches the critical value 48m/s (Fig. 7.14). This value of critical flow velocity is likely of practical significance [146, 151]. On the other hand, it can be verified that even a complaint elastic medium has a substantial effect to raise the critical flow velocity. For example, in the presence of an elastic medium of the Winkler-constant k=1GPa, the critical flow velocity of case I ($L/2R_{out}$ = 500) will increase to 4630m/s (Fig. 7.14).

Another interesting subject is structural instability of CNTs conveying fluid under internal high pressure. It is known in pipeline industries [155] that internally pressured elastic pipeline would buckle at a critical internal pressure. It is expected that similar phenomenon could occur for CNTs in some extreme cases. In fact, the critical global pressure can be determined simply by static buckling analysis of (7.1) [153, 154]. When the flow velocity V=0, this leads to a simple critical global pressure formula

$$p_{cr}^{*} = \frac{(r\pi)^2}{AL^2}\left(EI + k(\frac{L}{r\pi})^4\right) \tag{7.8}$$

for simply-supported CNTs, where the mode number r is determined to minimize the critical global pressure (7.8). Similarly, the critical global pressure for clamped CNTs is [153]

$$p_{cr}^{*} = \frac{(2\pi)^2}{AL^2}\left(EI + \frac{3kL^4}{16\pi^4}\right) \qquad \text{for} \quad k \le \frac{84}{11}\frac{\pi^4}{L^4}EI;$$

$$p_{cr}^{*} = \frac{\pi^2}{AL^2}\left(\frac{r^4 + 6r^2 + 1}{r^2 + 1}EI + \frac{kL^4}{(r^2+1)\pi^4}\right) \qquad \text{for} \quad k \ge \frac{84}{11}\frac{\pi^4}{L^4}EI \tag{7.9}$$

where the mode number r is the smallest integer satisfying (7.7). The formulas (7.8) and (7.9) are shown in Figs. 7.16 and 7.17, respectively, for various radii of CNTs. For example, the CNT of case I ($L/2R_{out}$ = 500) will buckle when the internal global pressure reaches a critical value 2.3GPa (Fig. 7.7-7.16). Although this value of critical pressure is higher than some known data for CNTs (about 100 MPa, [144, 145, 147], it is likely of practical significance in some extreme cases especially for CNTs of larger aspect ratio. On the other hand, even a complaint elastic medium has a substantial effect to raise the critical pressure. For example, in the presence of an elastic medium of the Winkler-constant k=1GPa, the critical pressure of case I ($L/2R_{out}$ = 500) will increase to 21.4 TPa (Fig. 7.16), which is simply beyond the range of practical

interest.

7.3 Summary

The influence of internal moving fluid on free vibration and flow-induced structural instability of CNTs is studied. It is shown that the internal moving fluid could substantially affect vibrational frequencies especially for suspended, longer and larger-innermost-radius CNTs at higher flow velocity. In particular, these results indicate that the critical flow velocity for structural instability of CNTs could fall within the range of practical significance at least in some extreme cases. On the other hand, a simple method to prevent such phenomena is to put CNTs within a surrounding elastic medium. Indeed, even a complaint surrounding elastic medium (such as polymer matrix) can significantly reduce the effect of internal moving fluid on vibrational frequencies, and suppress or eliminates structural instability within the practical range of flow velocity. It is believed that these results could provide useful data for the proposed application of CNTs as nanopipes conveying fluid. Also, the study of the dependence of resonant frequencies of CNTs conveying fluid on the flow velocity could offer a simple method to estimate the internal flow velocity by measuring the change in resonant frequencies.

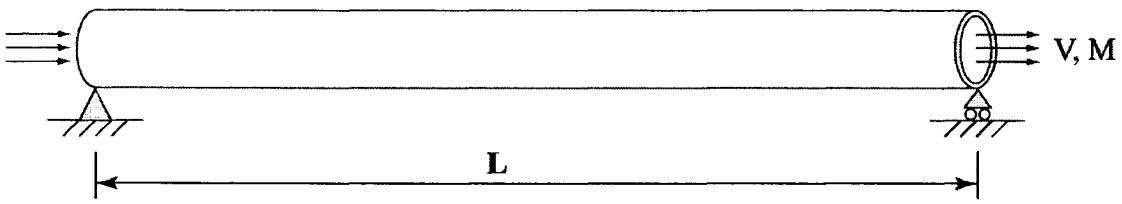

Fig. 7.1. CNT conveying fluid of the mass density M (per unit axial length) and the mean flow velocity

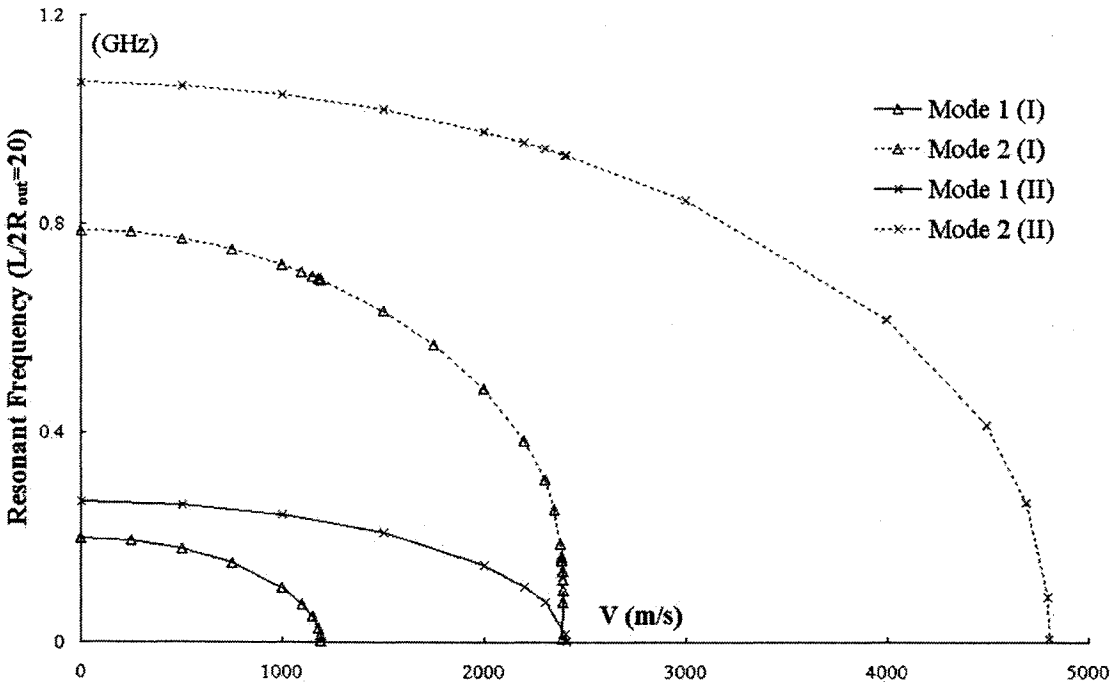

Fig. 7.2. Real frequency as a function of the water flow velocity, for the lowest two modes of a simply supported CNT with $L/2R_{out}=20$.

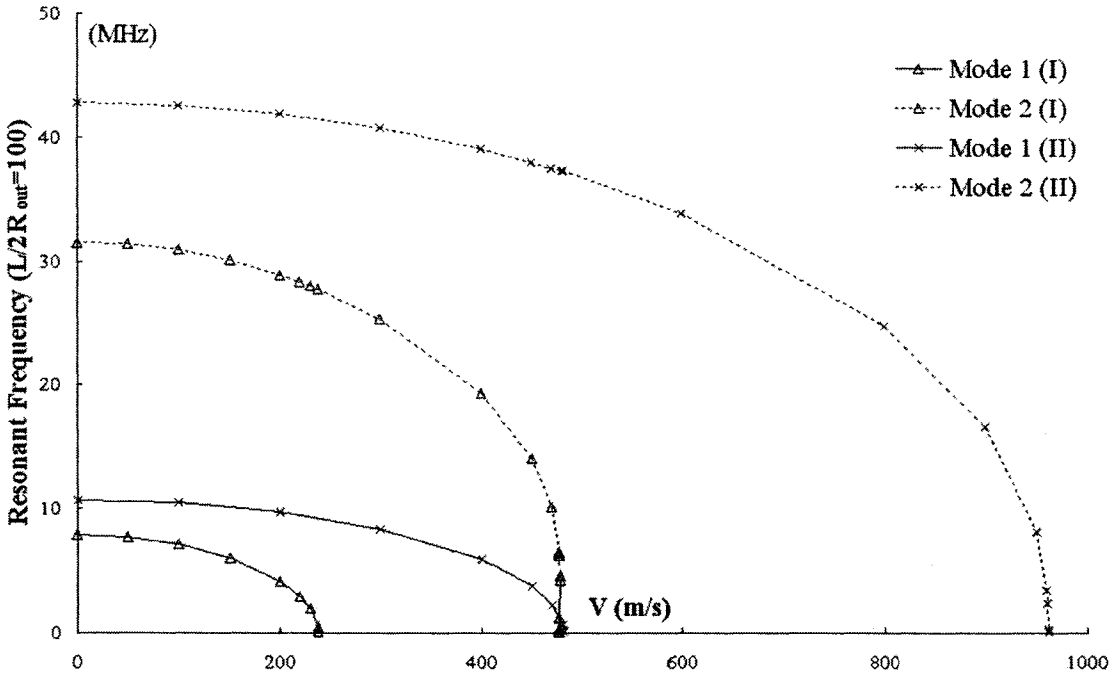

Fig. 7.3. Real frequency as a function of the water flow velocity, for the lowest two modes of a simply supported CNT with $L/2R_{out}=100$.

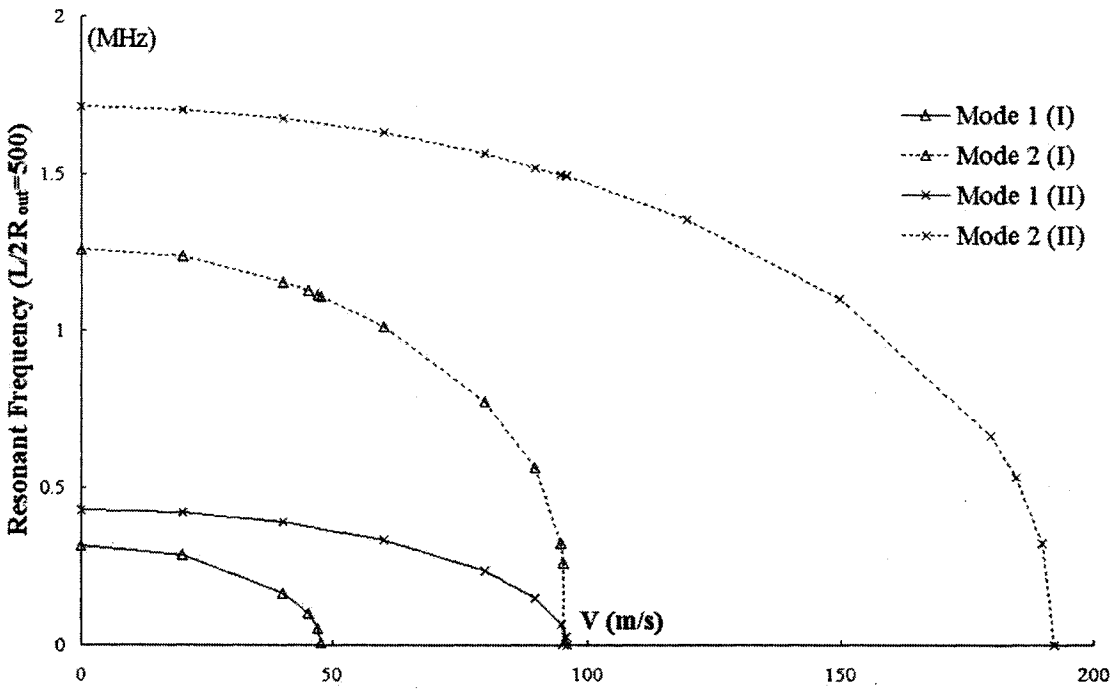

Fig. 7.4. Real frequency as a function of the water flow velocity, for the lowest two modes of a simply supported CNT with $L/2R_{out}=500$.

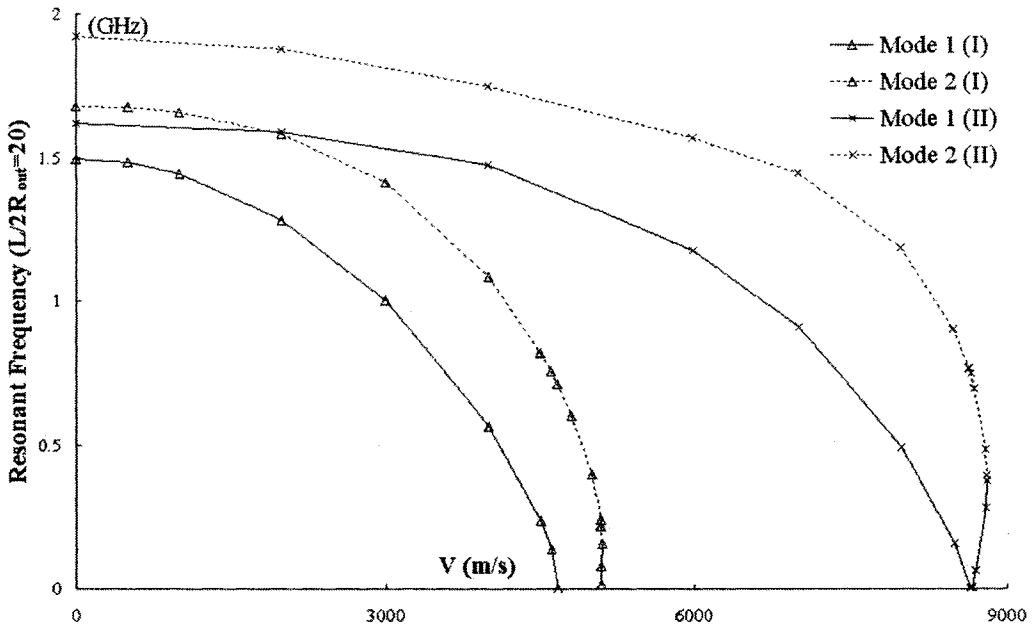

Fig. 7.5. Real frequency as a function of the water flow velocity, for the lowest two modes of a simply supported CNT ($L/2R_{out}=20$) surrounded by an elastic medium of k=1GPa.

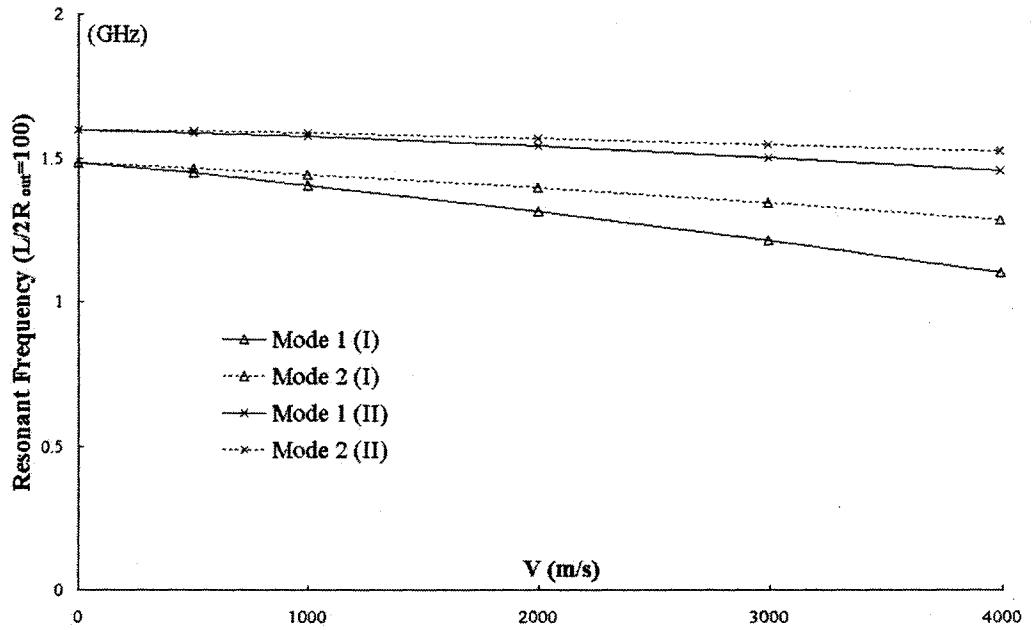

Fig. 7.6. Real frequency as a function of the water flow velocity, for the lowest two modes of a simply supported CNT ($L/2R_{out}=100$) surrounded by an elastic medium of k=1GPa.

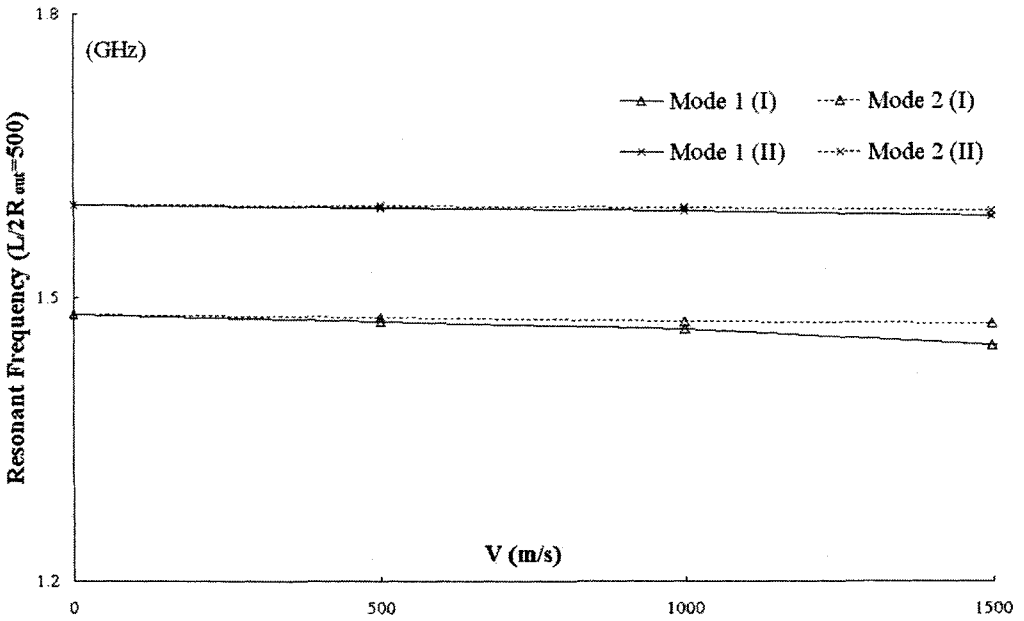

Fig.7.7. Real frequency as a function of the water flow velocity, for the lowest two modes of a simply supported CNT ($L/2R_{out}$=500) surrounded by an elastic medium of k=1GPa.

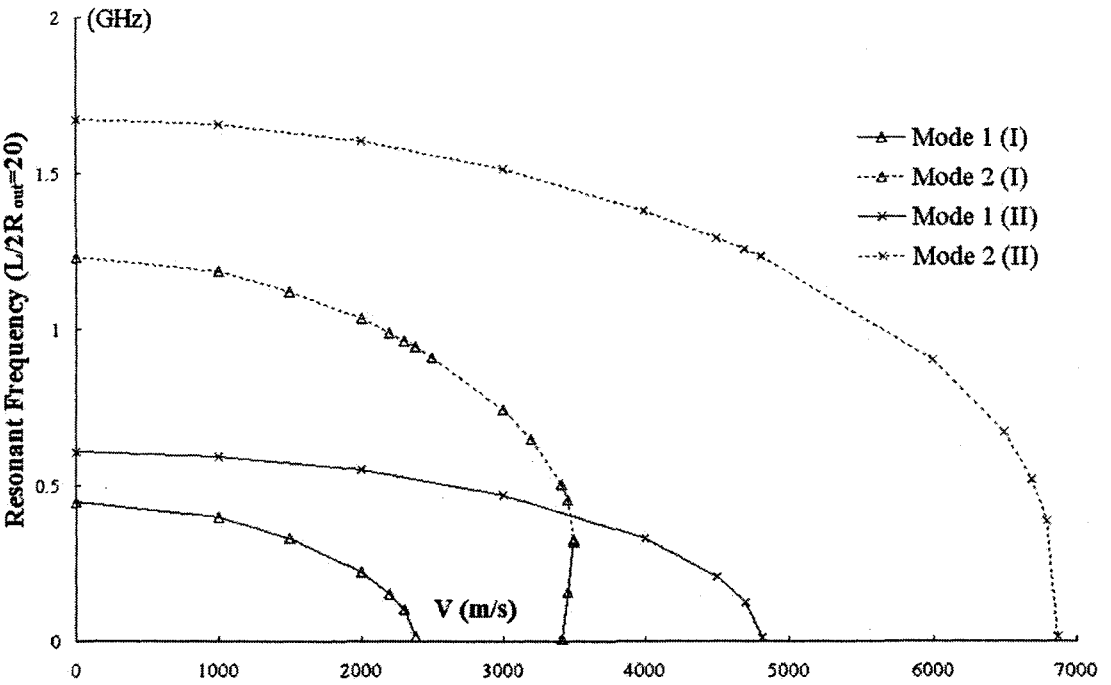

Fig. 7.8. Real frequency as a function of the water flow velocity, for the lowest two modes of a clamped CNT with $L/2R_{out}$=20.

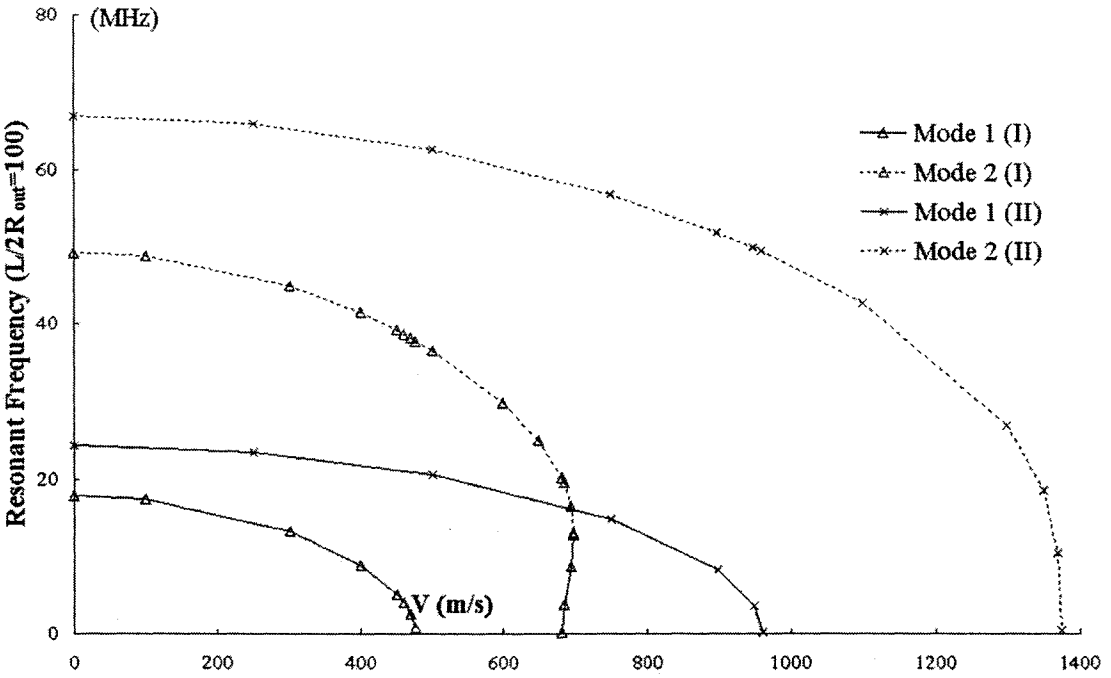

Fig. 7.9. Real frequency as a function of the water flow velocity, for the lowest two modes of a clamped CNT with $L/2R_{out}=100$.

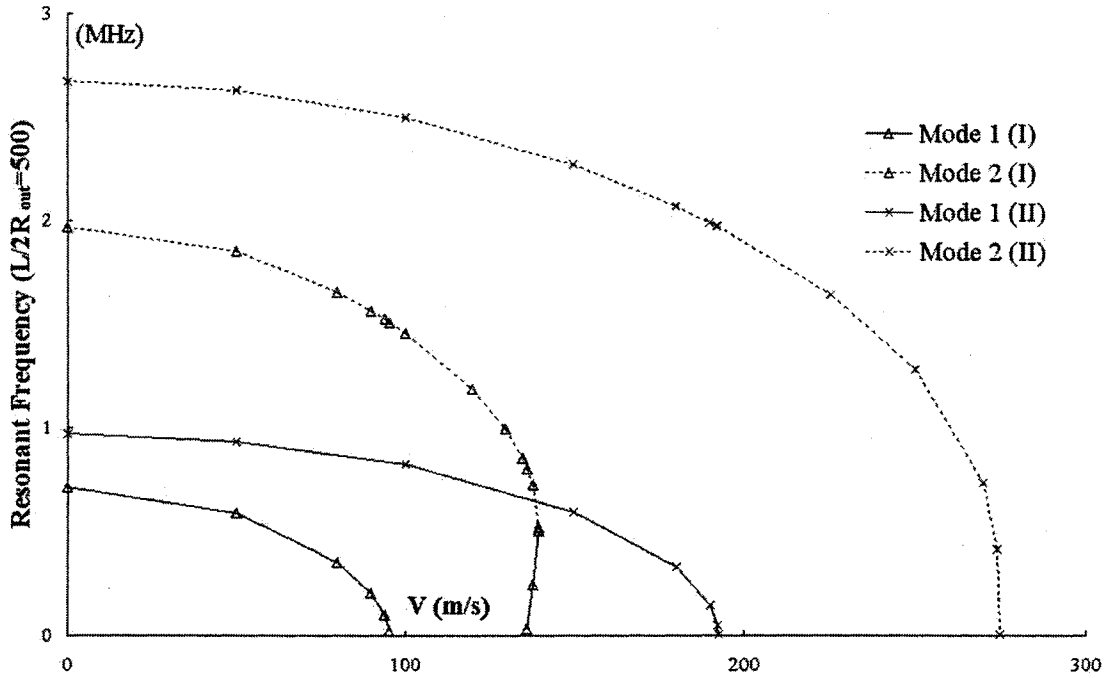

Fig. 7.10. Real frequency as a function of the water flow velocity, for the lowest two modes of a clamped CNT with $L/2R_{out}=500$.

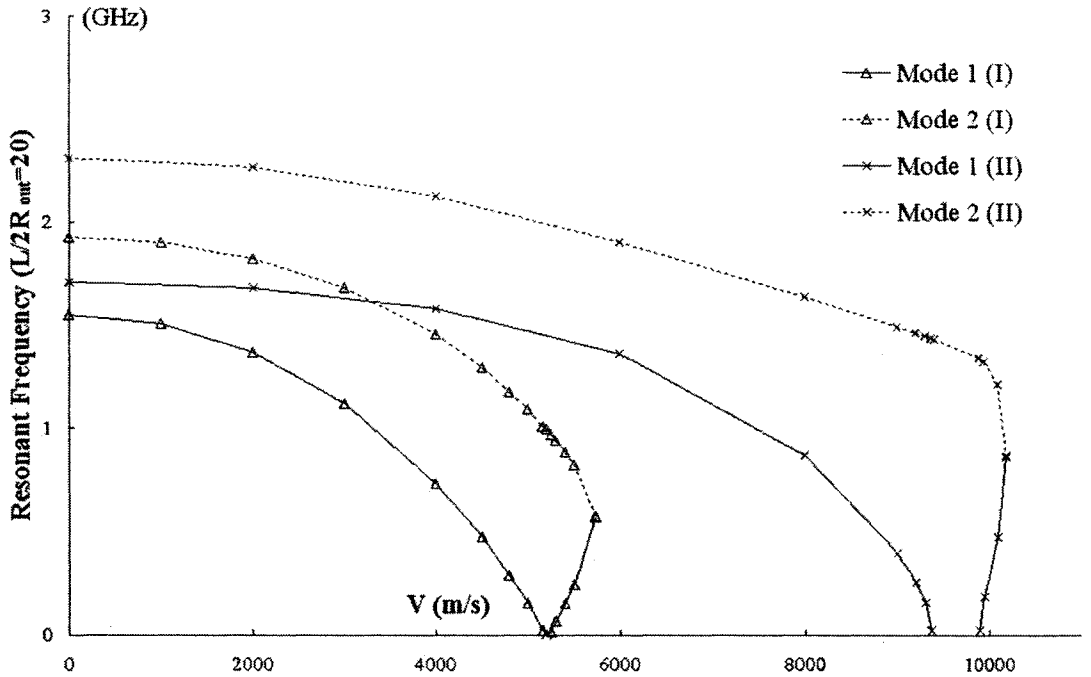

Fig. 7.11. Real frequency as a functions of the water flow velocity, for the lowest two modes of a clamped CNT ($L/2R_{out}$=20) surrounded by an elastic medium of k=1GPa.

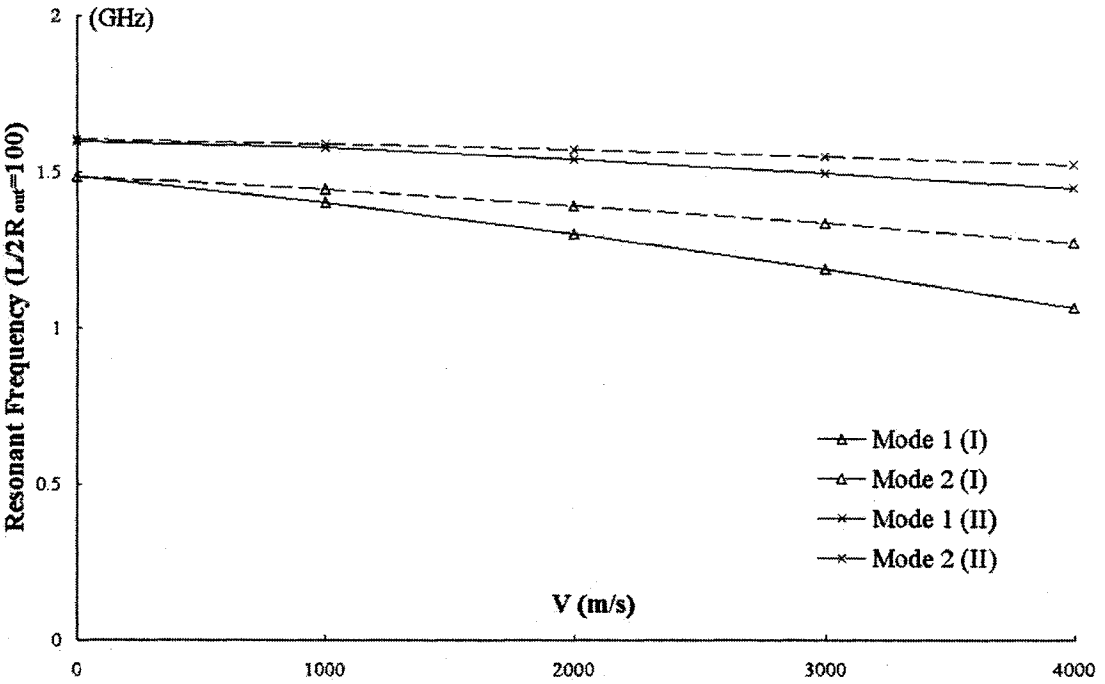

Fig. 7.12. Real frequency as a function of the water flow velocity, for the lowest two modes of a clamped CNT ($L/2R_{out}$=100) surrounded by an elastic medium of k=1GPa.

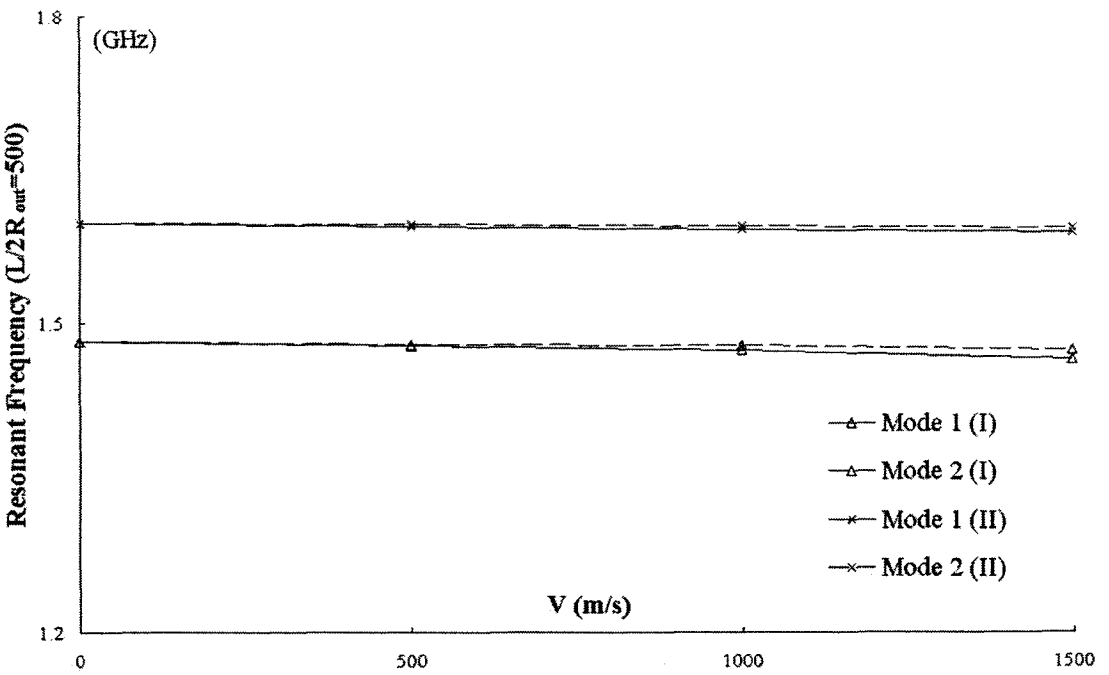

Fig. 7.13. Real frequency as a function of the water flow velocity, for the lowest two modes of a clamped CNT ($L/2R_{out}$=500) surrounded by an elastic medium of k=1GPa.

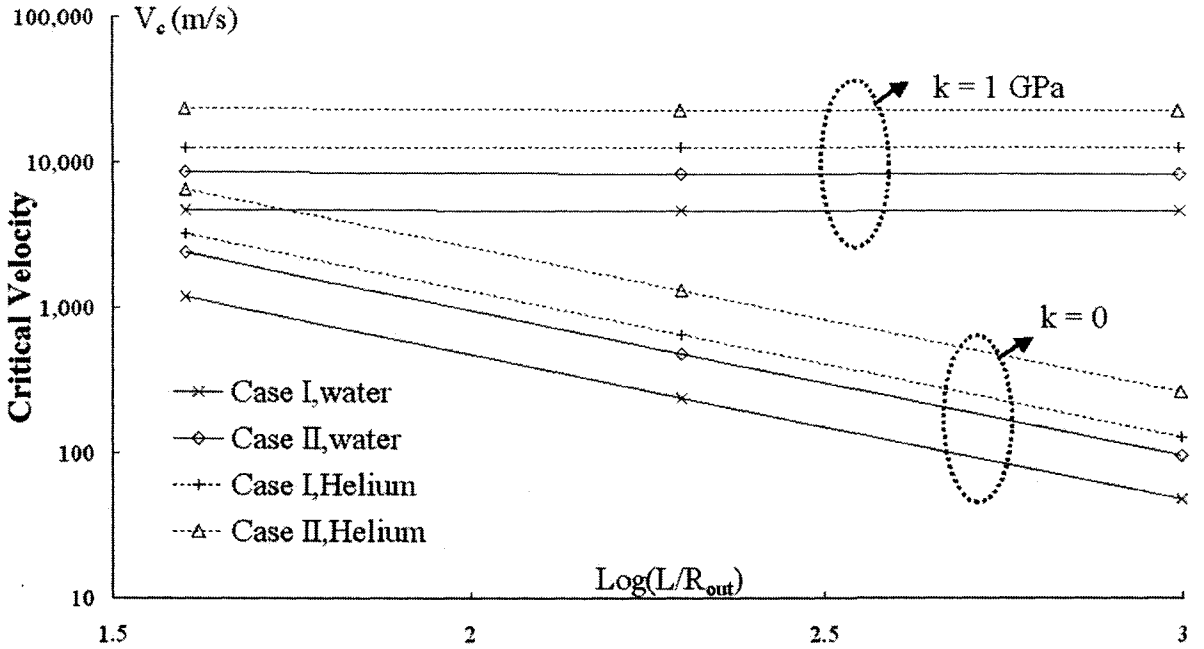

Fig.7.14. Critical flow velocity with the global pressure p^*=0 for simply supported CNTs.

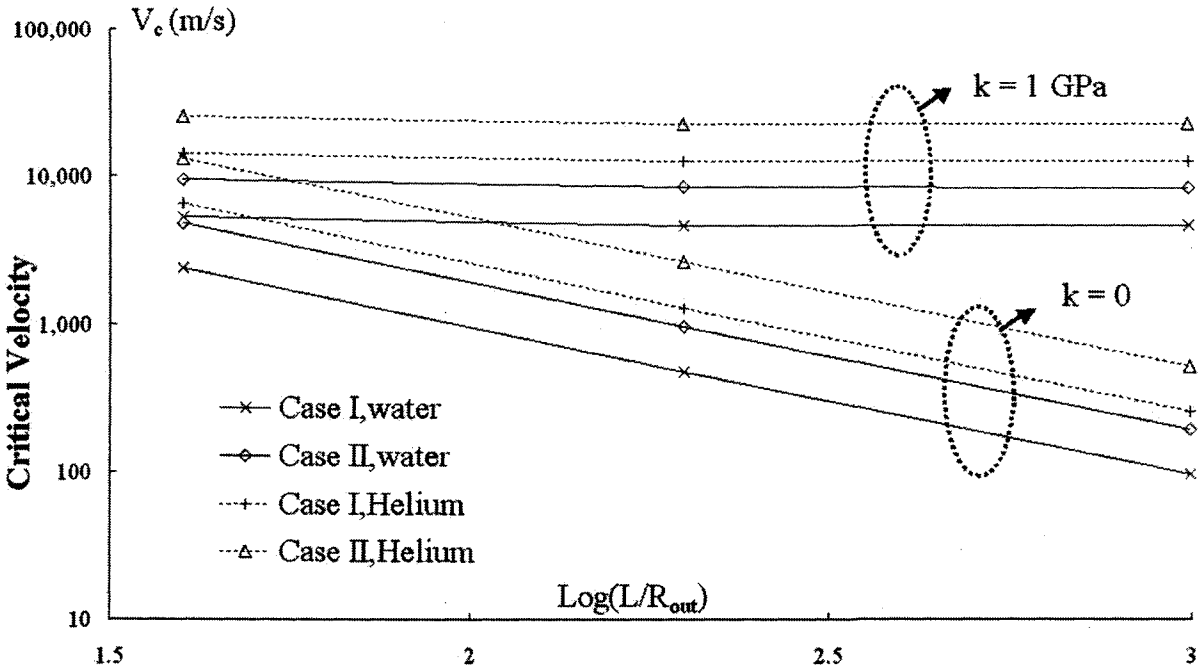

Fig.7.15. Critical flow velocity with the global pressure p^*=0 for clamped CNTs.

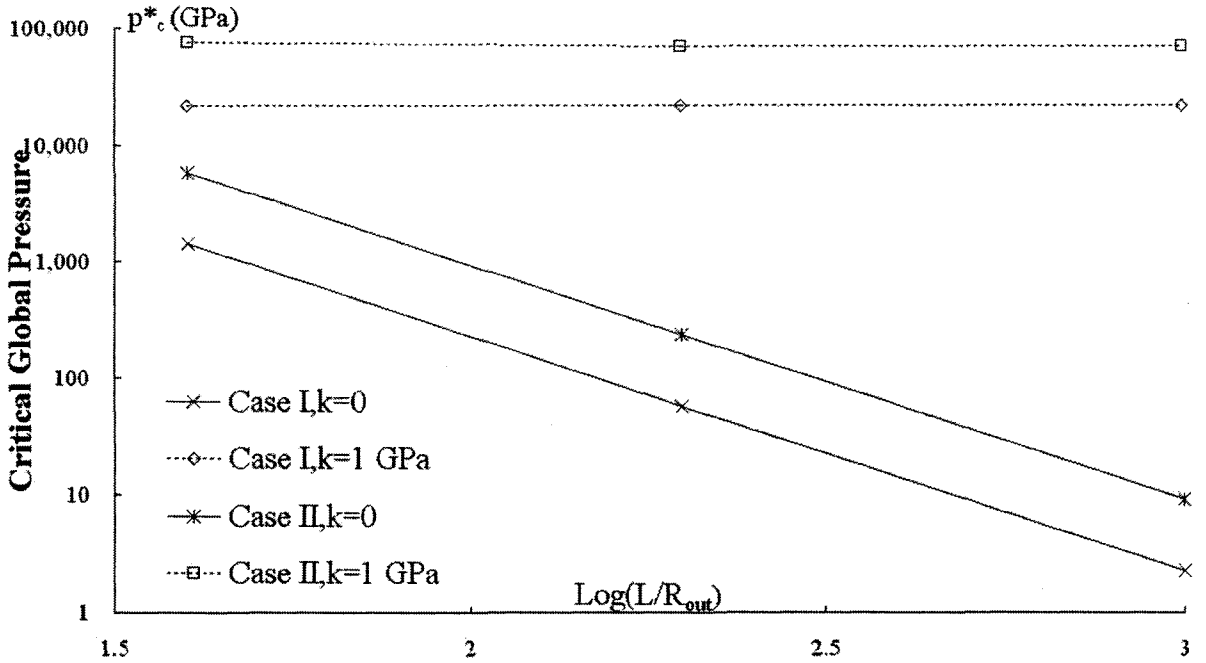

Fig.7.16. Critical global pressure with the flow velocity V=0 for simply supported CNTs.

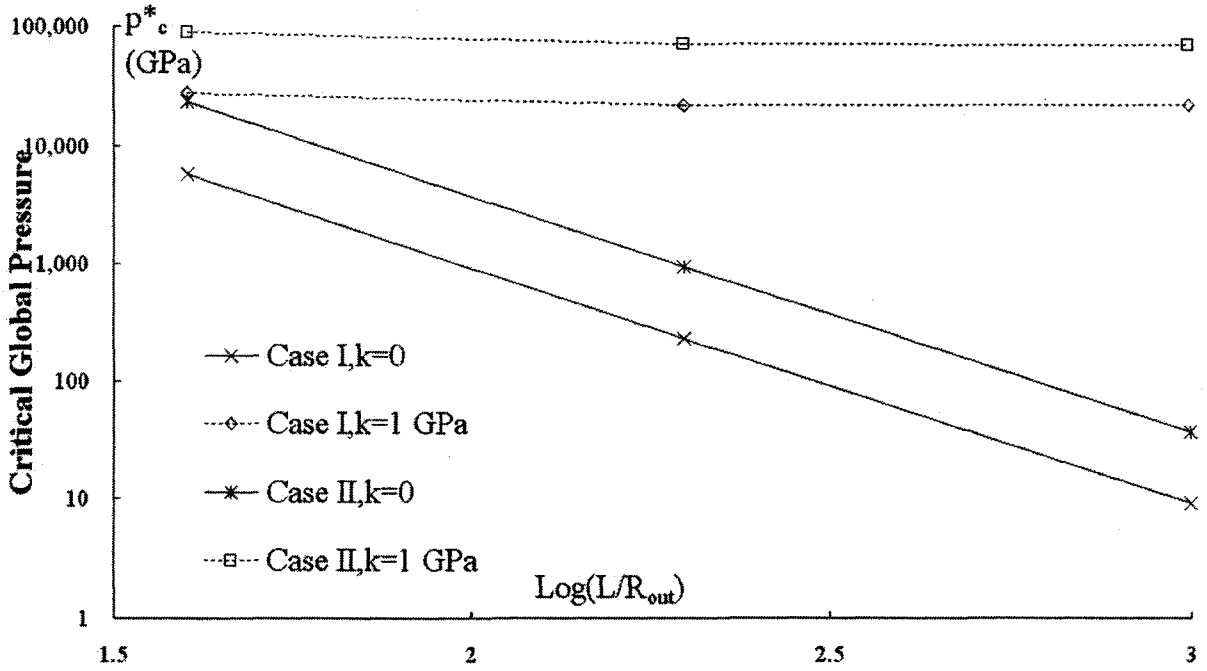

Fig.7.17. Critical global pressure with the flow velocity V=0 for clamped CNTs.

Chapter 8

Flow Induced Flutter Instability of Cantilever CNTs

8.1 Introduction

In the previous Chapter, the effects of internal moving fluid on free vibration and structural instability of CNTs pinned or clamped at both ends was studied [75]. In that case, internal flow-induced vibration of CNTs is conservative in nature and characterized by periodic vibration with constant amplitude, and the lowest frequency reduces to zero when a critical flow velocity is reached. This leads to "divergence instability" of supported CNTs, similar to static buckling of compressed elastic column. Our results show that internal moving fluid substantially affects vibrational frequencies especially for longer CNTs of larger innermost radius at higher flow velocity, and the critical flow velocity for "divergence instability" of CNTs in some cases may fall within the range of practical significance.

Many proposed applications of CNTs as nanopipes are likely involved with cantilever CNTs which are clamped at one end but free at the other end. It is known that flow-induced vibration of cantilever pipes is non-conservative in nature and characterized by decaying or growing amplitude [152-154]. When the flow velocity is sufficiently low, vibration of cantilever pipes fades off with

time. On the other hand, vibration amplitude will grow with time after a critical flow velocity is reached. This phenomenon is called "flutter" which has been studied extensively within the framework of aero-elasticity [156]. Motivated by the idea that vibration and flutter instability of cantilever CNTs conveying fluid are likely of both theoretical and practical interest, the present Chapter studies flow induced free vibration and flutter instability of cantilever CNTs [76].

8.2 The Model for CNTs Conveying Fluid

As shown in Fig. 8.1, a CNT conveying fluid will be described by a cantilever elastic hollow tube. Vibration and flutter instability of a cantilever CNT conveying fluid can also be described by the Eq. (7.1) [152-154]. It is again stressed that the role of internal moving fluid is characterized by two parameters of the fluid, its mass density M and the mean flow velocity V. The wall-fluid interaction and the viscosity of fluid inside CNTs do affect vibration and instability of CNT, but only through affecting the velocity distribution and the mean flow velocity. Hence, the effect of the wall-fluid interaction and the viscosity of fluid are implicitly included in the velocity distribution and the mean flow velocity, and will not explicitly appear in the governing equation (7.1). Therefore, the present work focuses on the effects of internal moving fluid on vibration and flutter instability, without concerning how the wall-fluid interaction and the viscosity of fluid affect the mean flow velocity V or what applied pressure gradient is required to achieve such a flow inside CNTs.

8.2.1. Flutter instability and Non Conservative System

As shown above, a cantilever pipe conveying fluid is a non-conservative system, which, for sufficiently high flow velocity, loses stability by flutter. Therefore cantilever CNTs conveying fluid are damped with decaying amplitude for flow velocity below a certain critical value. Beyond this critical flow velocity, flutter instability occurs and vibration becomes amplified with growing amplitude. To highlight the non-conservative nature of flow-induced flutter instability of cantilever CNTs, it is stated that, as explained by Benjamin [157] and Paidoussis and Li [154], the work (ΔW) done by the fluid forces to the elastic tube over a cycle of oscillation of period T is

$$\Delta W = -MV\int_0^T\left\{\left(\frac{\partial w}{\partial t}\right)^2 + V\left(\frac{\partial w}{\partial t}\right)\left(\frac{\partial w}{\partial x}\right)\right\}_L dt - \frac{M}{2}\int_0^L\left\{\left(\frac{\partial w}{\partial t}\right)^2 + V^2\left(\frac{\partial w}{\partial x}\right)^2\right\}_0^T dt \quad (8.1)$$

where $(\partial w/\partial t)_L$ and $(\partial w/\partial x)_L$ are the lateral velocity and the slope at the end x=L, respectively. For supported CNTs, because $(\partial w/\partial t)_L$ is identically zero, the first integral on RHS is zero. In addition, because the vibration is strictly periodic, the second term on RHS also vanishes. Hence, $\Delta W=0$ and vibration of supported CNTs is conservative. For a cantilever CNT, however, because the deflection and slope of the free end are not identically zero and the amplitude at t=T is not exactly the same as its value at t=0, none of the two integrals on RHS is identically zero. When V is sufficiently small, it turns out that the first term within the first square brackets is dominant over all other terms, it follows that

$\Delta W<0$, and thus the amplitude decays with time and the cantilever CNT is damped. However, this ceases to be true for sufficiently high flow velocity V which could lead to $\Delta W>0$. Thus cantilever CNTs could gain energy from the flow, and vibration would be amplified for sufficiently high flow velocity. In other words, for sufficiently high flow velocity, cantilever CNTs could lose stability by flutter. We believe that flutter instability of cantilever CNTs has significant consequences to the design of CNTs as nanopipes conveying fluid.

8.2.2 Vibrational Frequencies and Critical Flow Velocity

For free vibration of a cantilever CNT shown in Fig. 8.1, boundary conditions are

$$w(0,t)=\frac{\partial w}{\partial x}(0,t)=\frac{\partial^2 w}{\partial x^2}(L,t)=\frac{\partial^3 w}{\partial x^3}(L,t)=0 \tag{8.2}$$

Consider solutions of the form

$$w(x,t)=\mathrm{Re}[Ce^{i\alpha x}e^{i\omega t}] \tag{8.3}$$

where C is a constant, and ω is the complex circular frequency. Substitution of (8.3) into equation (7.1) gives

$$EI\alpha^4-MV^2\alpha^2-2MV\omega\alpha-(M+m)\omega^2+k=0 \tag{8.4}$$

which determines four complex roots α_n (n=1,2,3,4) as a function of ω. The complete solution of equation (7.1) is thus

$$w(x,t) = \mathrm{Re}[\sum_{n=1}^{4} C_n e^{i\alpha_n x} e^{i\omega t}] \tag{8.5}$$

where the constants C_n (n=1,2,3,4) should be determined by the boundary condition (8.2). Thus, substituting (8.5) into (8.2) yields

$$\begin{bmatrix} 1 & 1 & 1 & 1 \\ \alpha_1 & \alpha_2 & \alpha_3 & \alpha_4 \\ \alpha_1^2 e^{i\alpha_1} & \alpha_2^2 e^{i\alpha_2} & \alpha_3^2 e^{i\alpha_3} & \alpha_4^2 e^{i\alpha_4} \\ \alpha_1^3 e^{i\alpha_1} & \alpha_2^3 e^{i\alpha_2} & \alpha_3^3 e^{i\alpha_3} & \alpha_4^3 e^{i\alpha_4} \end{bmatrix} \begin{bmatrix} C_1 \\ C_2 \\ C_3 \\ C_4 \end{bmatrix} = 0 \tag{8.6}$$

The condition for existence of a non-trivial solution gives the characteristic equation in ω, which determines the eigenvalues and the associated vibrational modes. For very small V, it turns out that the imaginary parts of all eigenvalues, which represent the decaying rate of amplitude, are non-negative and hence the vibration amplitude decays with time. As V increases, the imaginary parts of ω vary and at least one of them will reduce to zero at a certain critical flow velocity $V=V_c$ beyond which the imaginary part of ω changes sign from positive to negative and the amplitude will grow with time. This indicates the onset of flutter instability. In this paper, we shall confine ourselves to the effect of internal moving fluid on the first three vibrational modes of the CNT described by (7.1). Here, as usual, the first, second, and third vibrational modes

are defined by the three lowest vibrational frequencies at V=0. For V>0, however, all frequencies vary with V. Hence, it is possible that the frequency of a higher mode may be even lower than the frequency of a lower mode for sufficiently high flow velocity V. For example, the frequency of mode 2 may be even lower than the frequency of mode 1 for sufficiently high V.

The examples of CNTs considered here are: I) MWNT with the outermost radius R=40 nm and thickness t=20 nm, II) MWNT with R=50nm and t=10nm [144], where the thickness t is defined as the difference between the outermost and the innermost radii. Here, two different aspect ratios of CNTs, L/2R=10 or 50, are considered. On the other hand, to be specific, water has been considered as the fluid inside CNTs. The mass density of CNTs is 2.3g/cm^3 with Young's modulus E of 1 TPa, and the mass density of water is 1g/cm^3. In addition, to study the effect of a surrounding elastic medium modeled as a Winkler-like elastic foundation, the Winkler-constant k is considered to have a value ranging from 1 KPa or 1MPa (for soft materials such as bio-tissue, [158]), to 1 GPa (for moderately stiff materials like polymers [71]). Finally, we shall consider here the flow velocity V up to 10000m/s, in spite of the fact that the available data for the flow velocity of water in CNTs (of very small innermost diameter) are much lower than this value.

In what follows, vibrational frequency f=Re($\omega/(2\pi)$) and the decaying rate Im($\omega/(2\pi)$) of cantilever CNTs conveying fluid are calculated and shown in Fig. 8.2-8.13 for CNTs with or without being embedded in a surrounding elastic

medium characterized by the Winkler constant k. The main results are summarized as follows.

1) The results of Figs. 8.2-8.13. indicate that internal moving fluid has a substantial effect on vibrational frequencies (=Re($\omega/(2\pi)$)) and the decaying rate (=Im($\omega/(2\pi)$)) of cantilever CNTs conveying fluid. This effect is more significant at higher flow velocity even for CNTs of smaller aspect ratio (L/2R=10), and for CNTs of larger aspect ratio (such as L/2R=50, as shown in Fig. 8.5-8.7 and 8.11-8.13) even at lower flow velocity, but is less significant for CNTs of smaller aspect ratio (such as L/2R=10, as shown in Figs. 8.2-8.4 and 8.8-8.10) at lower flow velocity.

2) Vibrational frequencies (=Re($\omega/(2\pi)$)) of CNTs conveying fluid vary with increasing flow velocity. For example, in Case I with L/2R=50 and K=0 (Fig. 8.5), vibrational frequency of mode 1 increases slowly up to V=1500m/s, then begins to decrease, and finally reduces to zero around V=2000m/s and remains zero until V=2700m/s. So, between V=2000m/s and 2700m/s, the frequency of the first mode is identically zero [156], which means that the amplitude of deflection of the cantilever CNT decays monotonically with time without backward and forward oscillation. In addition, for Case II with L/2R=10 and k=0, it is seen from Fig.8.8 that the frequency of the mode 1 reduces to zero around V=2800m/s and remains zero until V=4300m/s. These phenomena qualitatively agree with the general results of cantilever elastic tubes conveying fluid [153].

3) For lower flow velocity U, internal flow causes damping to cantilever CNTs in all modes and the vibration amplitude of CNTs decays with time. For example, for L/2R=10 and 50, the cantilever CNTs in all cases discussed here are damped for flow velocity below 6000m/s, and 1200m/s, respectively. This phenomenon is common for the examples I, II, with or without a surrounding elastic medium, as shown in Figs. 8.2-8.13.

Winkler const (K)		0		1KPa		1MPa		1GPa
Aspect ratio (L/2R)		10	50	10	50	10	50	10
Case I	Mode 1	-	-	-	-	-	-	-
	Mode 2	7560m/s	1510m/s	7560m/s	1510m/s	7560m/s	1790m/s	10080m/s
	Mode 3	-	-	-	-	-	-	-
Case II	Mode 1	-	-	-	-	-	-	-
	Mode 2	12070m/s	2410m/s	12070m/s	2420m/s	12070m/s	2440m/s	-
	Mode 3	6800m/s	1360m/s	6800m/s	1360m/s	6800m/s	1490m/s	7920m/s

Table 8.1 Critical flow velocity for flutter instability of cantilever CNTs

4) Without a surrounding elastic medium (k=0), the critical flow velocity for flutter instability, at which the decaying rate of amplitude changes from positive

to negative and thus the amplitude starts to grow, is inversely proportional to the aspect ratio (L/2R), while both vibrational frequency (=Re(ω/(2π))) and the decaying rate (=Im(ω/(2π))) are inversely proportional to square of the aspect ratio (L/2R) (Figs. 8.2-8.13). For example, in Case I, the critical flow velocities V_c for flutter instability (of mode 2) are 7564m/s and 1512m/s for L/2R =10 and 50, respectively (Table. 8.1). On the other hand vibrational frequencies (=Re(ω/(2π))) of mode 1 at V=0, at which the decaying rate is zero for both case, are 380MHz and 15MHz for L/2R =10 and 50, respectively. On the other hand, for the same aspect ratio (L/2R), the effect of internal flow on vibrational frequencies (=Re(ω/(2π))) and the decaying rate (=Im(ω/(2π))) are more significant for thin CNTs than for thicker CNTs. For example, for L/2R=10, flutter instability occurs at 7564m/s for thicker CNT of smaller innermost radius (Case I), and at 6803m/s for thin CNT of larger innermost radius (Case II) (Table. 8.1). This is attributed to the fact that when the outermost radius is not very different, the restoring flexural force of CNTs of smaller innermost radius is significantly larger than that of CNTs of larger innermost radius, and thus the destabilizing centrifugal force overcomes the restoring flexural force only at a higher flow velocity.

5) As studied in chapter 7, even a compliant surrounding elastic medium has a significant effect on flow-induced instability of supported CNTs conveying fluid. Here, Let us consider the role of a surrounding elastic medium in flutter instability of cantilever CNTs. First, with a very soft surrounding elastic medium, such as bio-tissue with k=1 KPa [158], all phenomena for vibration

and flutter instability of cantilever CNTs are similar as those obtained above in the absence of a surrounding elastic medium (k=0). For example, the critical flow velocity V_c of Case II when L/2R=50 and k=1KPa is 1364m/s, which is almost same as 1361m/s of the same case with k=0 (Table. 8.1). Hence, it is concluded that a very soft surrounding elastic medium (say k≤1KPa) has almost no effect on vibrational frequencies and the decaying rate of cantilever CNTs conveying fluid.

6) When the Winkler constant of the surrounding elastic medium increases to 1 MPa, the surrounding elastic medium still doesn't make any significant difference for CNTs of smaller aspect ratio L/2R=10. However, if the aspect ratio is larger (such as L/2R = 50), a surrounding elastic medium with k=1MPa significantly reduces the sensitivity of vibrational frequency (=Re($\omega/(2\pi)$)) and the decaying rate (=Im($\omega/(2\pi)$)) to the internal flow velocity V. For example, the critical flow velocity V_c of Case I with L/2R=50 increases from 1512m/s for k=0 to 1789m/s for k=1MPa (Table. 8.1). Hence, the role of a surrounding elastic medium with k=1MPa becomes significant for CNTs of larger aspect ratio, such as those shown in Figs. 8.5-8.7, and 8.11-8.13.

7) When a moderately stiffer surrounding elastic medium (such as polymer with k=1GPa) is considered, the surrounding elastic medium has a more significant effect on vibrational frequency and the decaying rate. For example, even for a short CNT (L/2R=10), the critical flow velocity V_c of Case I increases from 7564m/s when k=0 to 10076m/s when k=1GPa (Table. 8.1). Therefore, it is concluded that a moderately stiff surrounding elastic medium (with k=1GPa)

has a significant effect on vibrational frequencies and flutter instability even for CNTs of small aspect ratio L/2R=10.

8.3 Summary

The influence of internal moving fluid on free vibration and flow-induced flutter instability of cantilever CNTs is studied. Unlike supported CNTs, which lose stability by static buckling, cantilever CNTs lose stability by flutter at a certain critical flow velocity. These results indicate that internal moving fluid has a substantial effect on vibrational frequencies and the decaying rate of amplitude, and the critical flow velocity for flutter instability in some cases may fall within the range of practical significance. On the other hand, these studies indicate that a moderately stiff surrounding elastic medium can significantly reduce the effect of internal moving fluid on vibrational frequencies and suppress or eliminate the flow-induced flutter instability, while a very soft surrounding elastic medium has almost no effect on vibrational frequencies and the decaying rate of amplitude.

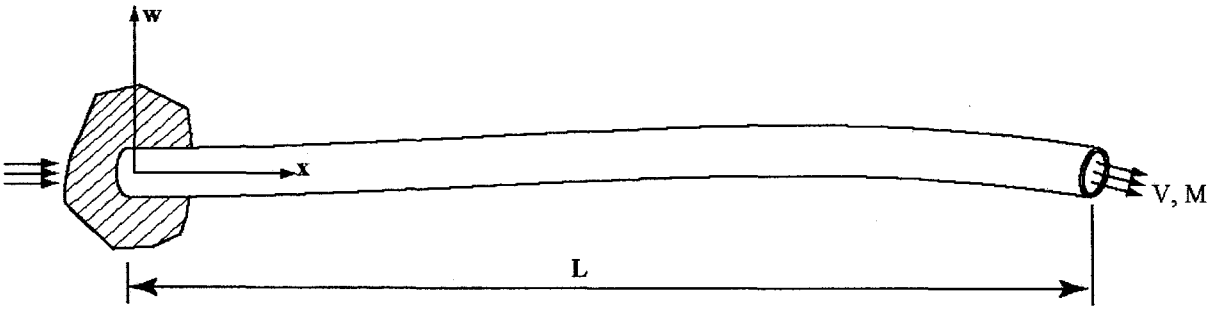

Fig. 8.1. Cantilever CNT conveying fluid of the mass density M (per unit axial length) and the mean flow velocity V.

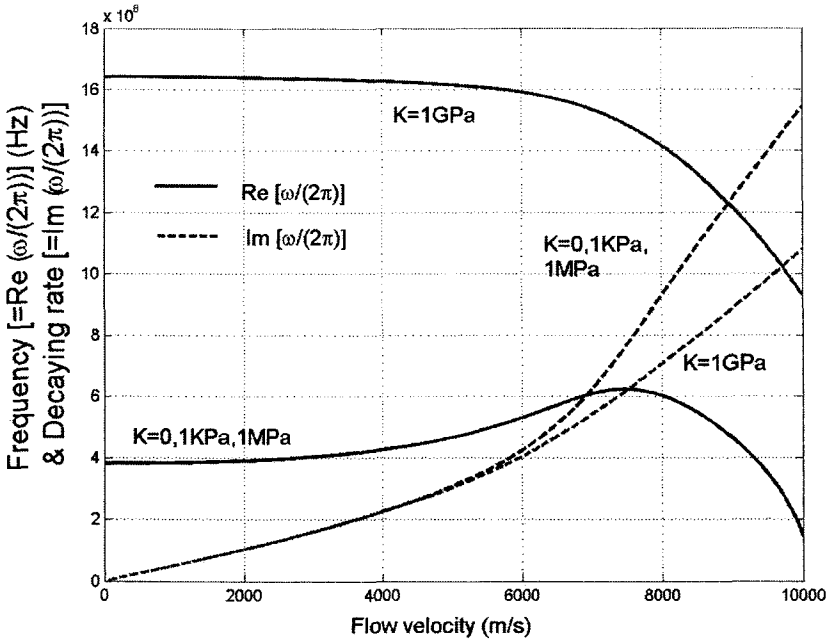

Fig. 8.2. Frequency and the decaying rate of amplitude as a function of the flow velocity (Case I, L/2R=10, mode 1)

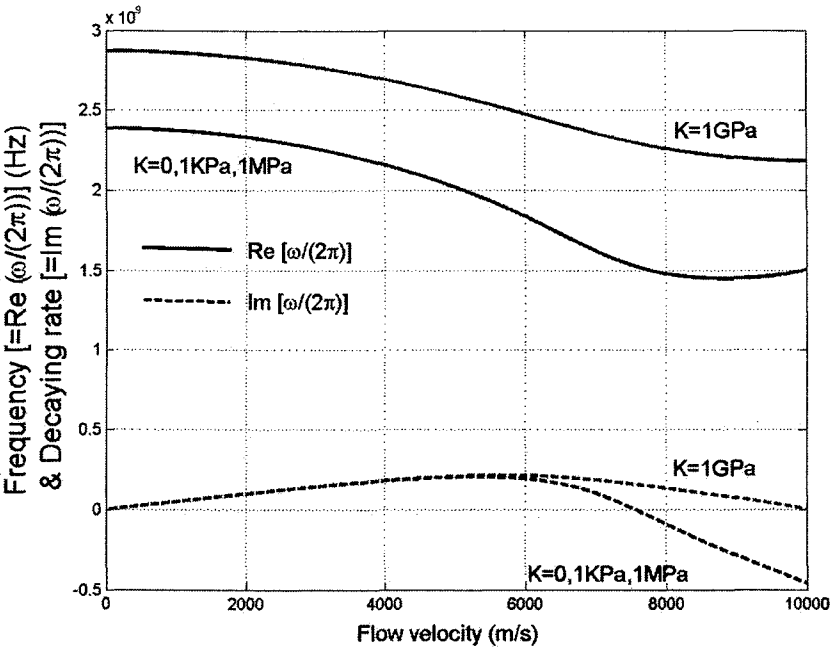

Fig. 8.3. Frequency and the decaying rate of amplitude as a function of the flow velocity (Case I, L/2R=10, mode 2)

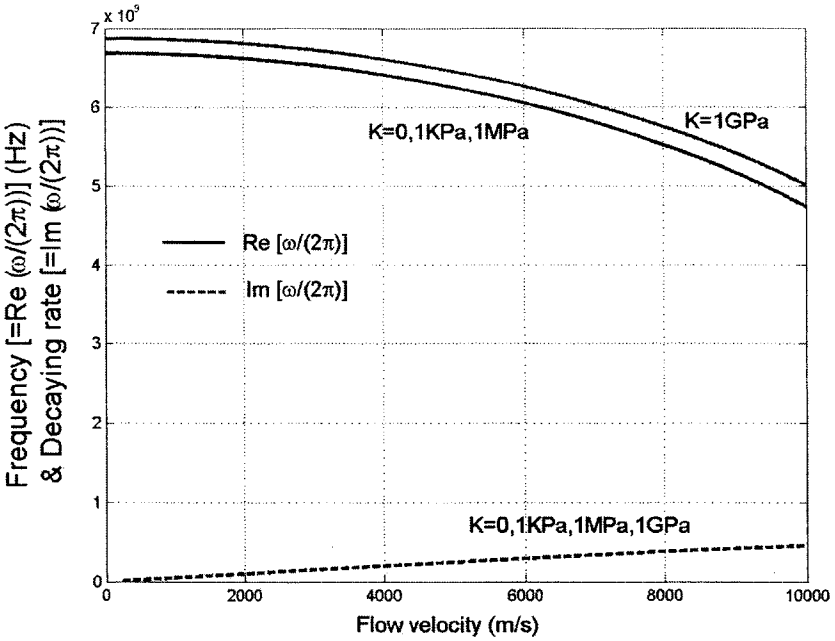

Fig.8.4. Frequency and the decaying rate of amplitude as a function of the flow velocity (Case I, L/2R=10, mode 3)

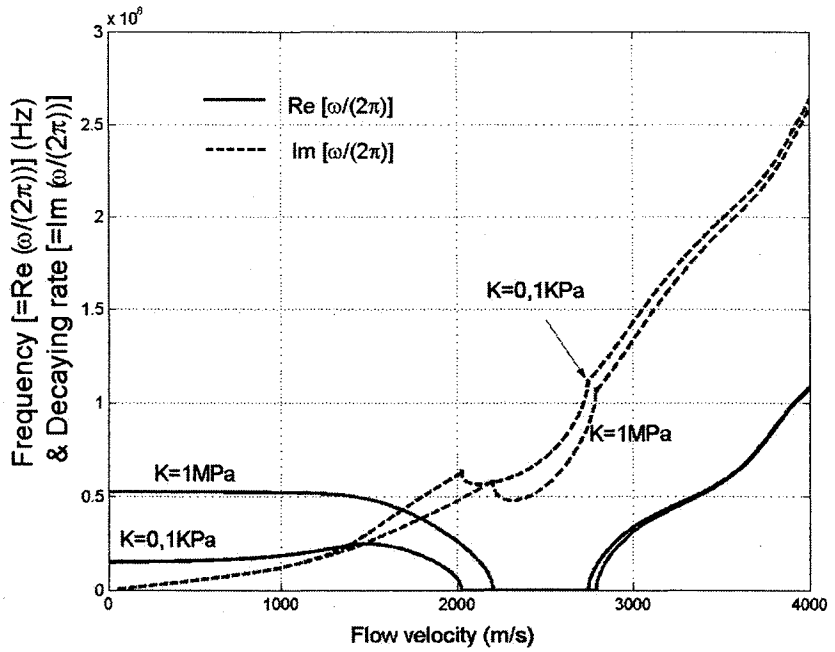

Fig. 8.5. Frequency and the decaying rate of amplitude as a function of the flow velocity (Case I, L/2R=50, mode 1)

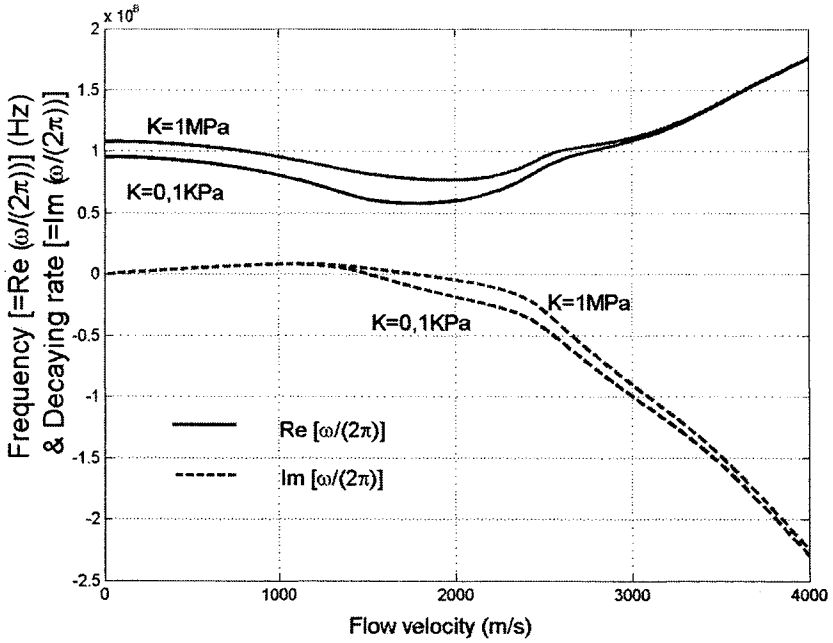

Fig. 8.6. Frequency and the decaying rate of amplitude as a function of the flow velocity (Case I, L/2R=50, mode 2)

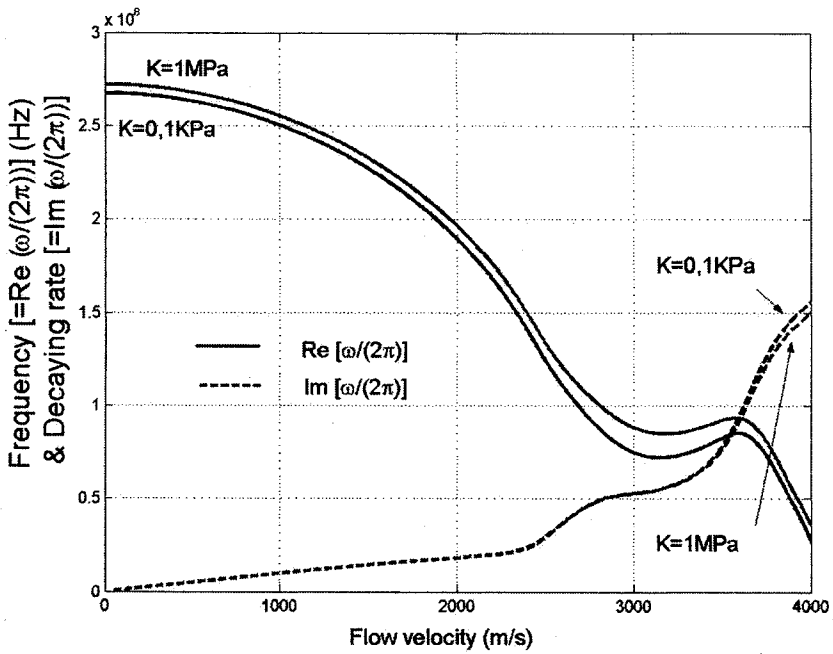

Fig. 8.7. Frequency and the decaying rate of amplitude as a function of the flow velocity (Case I, L/2R=50, mode 3)

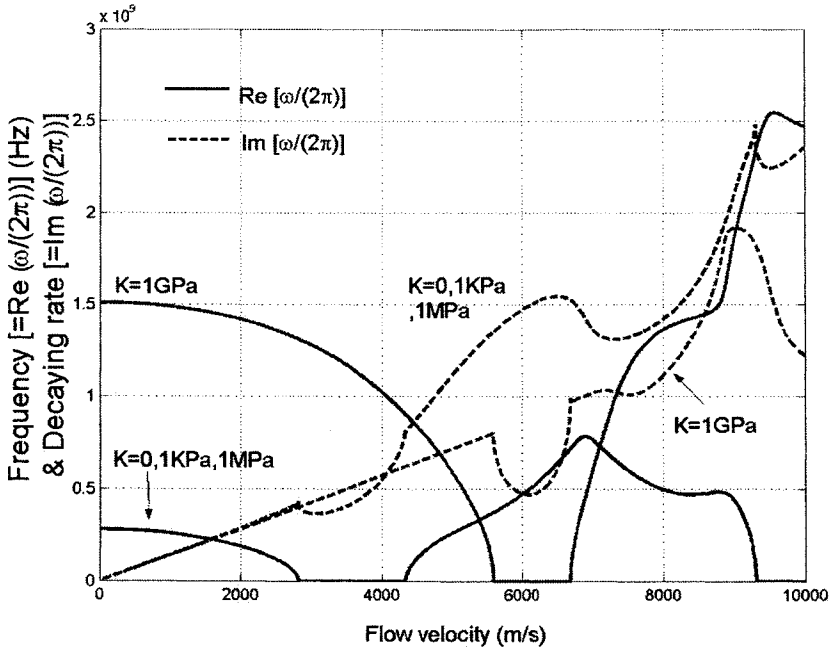

Fig. 8.8. Frequency and the decaying rate of amplitude as a function of the flow velocity (Case II, L/2R=10, mode 1)

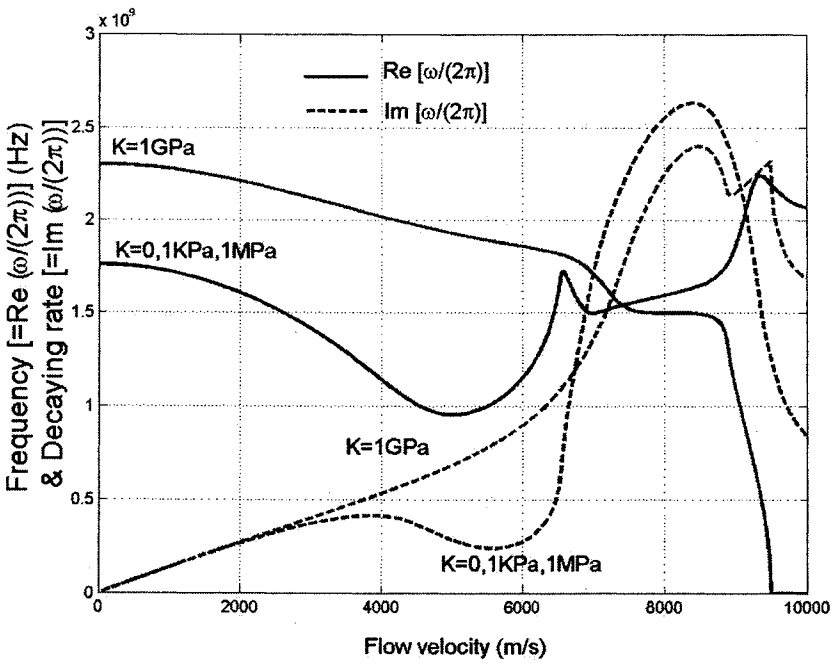

Fig. 8.9. Frequency and the decaying rate of amplitude as a function of the flow velocity (Case II, L/2R=10, mode 2)

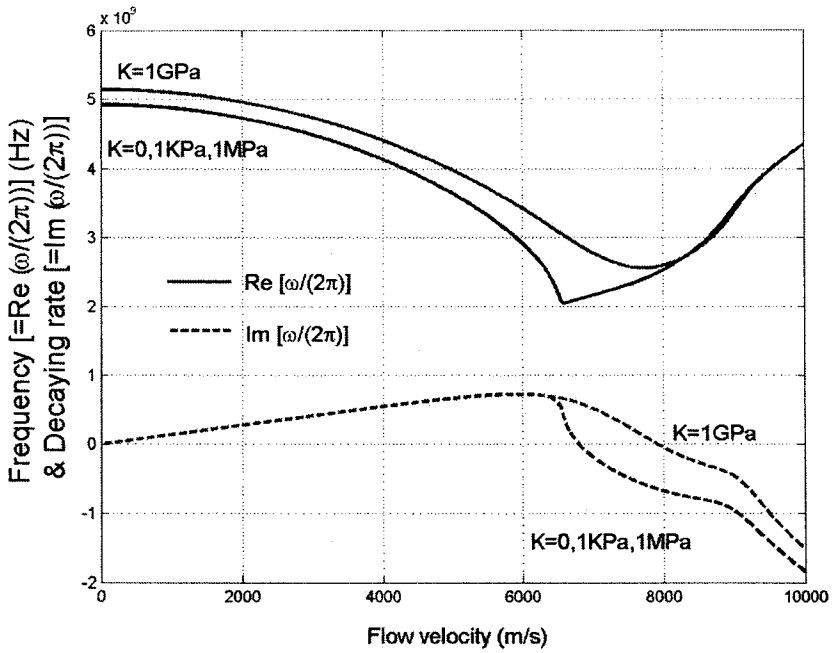

Fig. 8.10. Frequency and the decaying rate of amplitude as a function of the flow velocity (Case II, L/2R=10, mode 3)

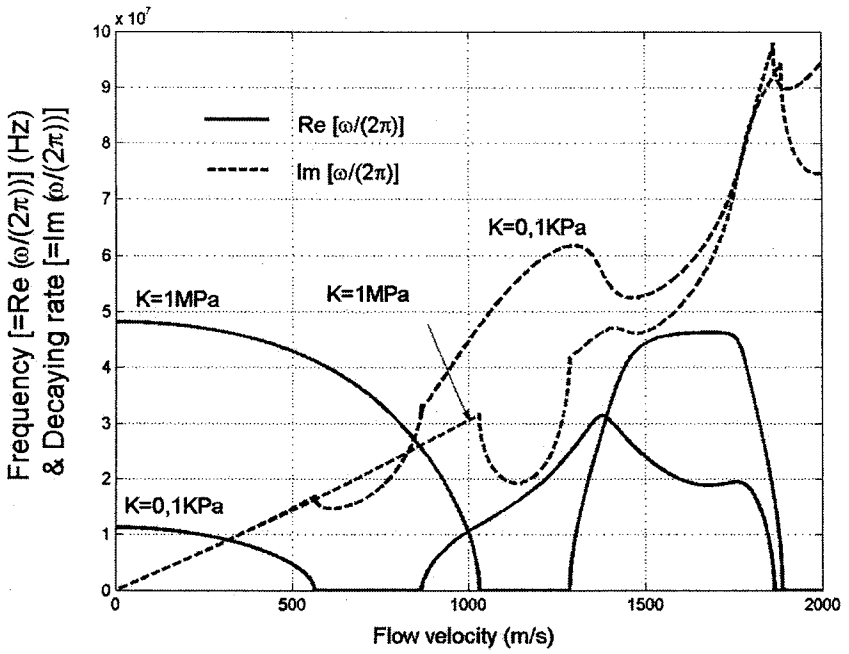

Fig. 8.11. Frequency and the decaying rate of amplitude as a function of the flow velocity (Case II, L/2R=50, mode 1)

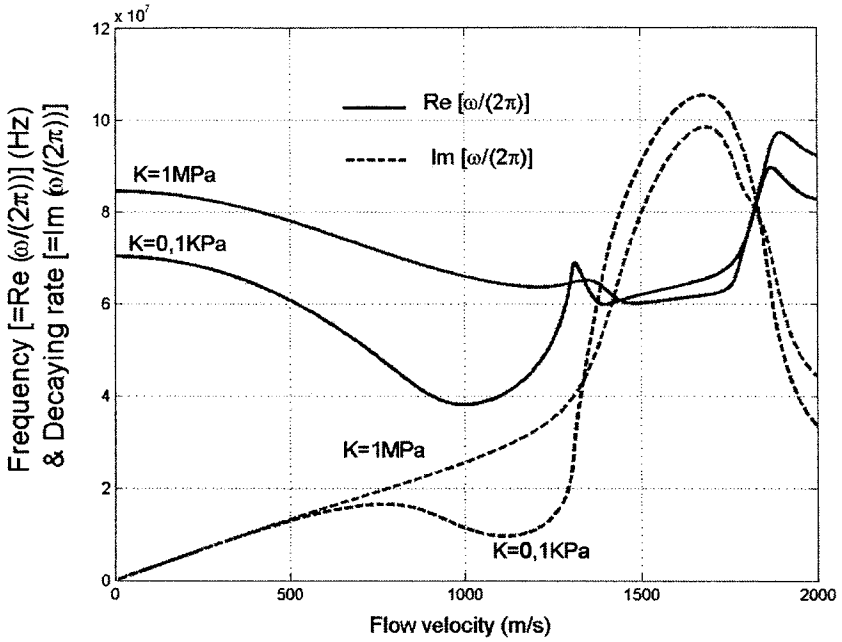

Fig. 8.12. Frequency and the decaying rate of amplitude as a function of the flow velocity (Case II, L/2R=50, mode 2)

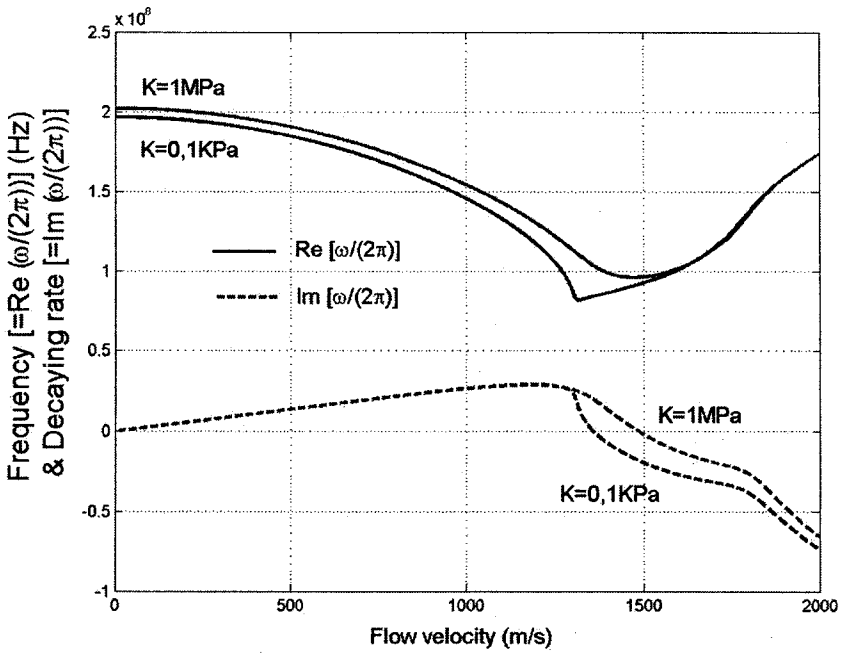

Fig. 8.13. Frequency and the decaying rate of amplitude as a function of the flow velocity (Case II, L/2R=50, mode 3)

Chapter 9

Conclusions and Future Plans

9.1 Conclusions

The elastic beam models provide a powerful and effective approach for CNTs, and could play an indispensable role in the study of CNTs. In addition, since the elastic beam models enjoy very simple mathematical formulas, they have the potential to identify the key parameters affecting basic mechanical behavior of CNTs (and thus rule out other less important parameters), explain or predict new physical phenomena, and stimulate and guide further experiments and molecular dynamics simulations.

In this dissertation, several elastic beam models have been developed and utilized to study dynamics of MWNTs, such as free vibration, sound wave propagation and instability. Since the existing single-elastic beam model widely used in the literature assumes that all nested individual tubes of a MWNT remain coaxial during deformation and vibration, it cannot be used to study intertube relative vibration of MWNTs. For this reason, a multiple-Euler-beam model is developed, in which each of the nested, originally concentric nanotubes of a MWNT is described as an individual elastic beam, and the deflections of all nested tubes are coupled through the van der Waals interaction

between any two adjacent tubes. As shown Chapter 3 and 4, the multiple-beam model shows that internal degrees of freedom of MWNTs become essential when the characteristic wavelength of vibrational modes is just few times larger than the outermost diameter of MWNTs. In this case, more accurate elastic model that considers interlayer radial displacements of MWNTs is required.

Another issue that is probably significant in this case is the effects of rotary inertia and shear deformation. For this reason, a multiple-Timoshenko-beam model is developed and studied in chapter 4 and 5 for vibration and wave propagation in CNTs. Finally, the influence of internal moving fluid on free vibration and flow-induced structural instability of (hollow) CNTs is studied based on the elastic beam model. Many of the results obtained by the present models are reported in literature for the first time, and still remain challenging for experiments and atomistic simulations. On the other hand, some results predicted by present models, such as non-coaxial vibration of MWNTs and the validity of the Timoshenko-beam model for CNTs have been confirmed by more recent atomistic simulations [95-97]. Here, major conclusions based on our work [70-76] are summarized as follows.

♦ Vibration of MWNTs

1) For the first time, non-coaxial vibration of MWNTs is predicted by the multiple-beam model. In particular, the first few non-coaxial resonant

frequencies are found to be insensitive to vibrational modes, length of MWNTs, and the end conditions, while they decrease with the number of nested layers.

2) For smaller aspect ratios, the lowest non-coaxial intertube resonant frequencies are found to be comparable to the first few higher natural frequencies. This implies that internal non-coaxial resonance will be excited at the higher natural frequencies, and MWNTs cannot maintain their concentric structure at ultrahigh frequencies. These results have been confirmed by more recent molecular simulations, which offers an evidence for validity of the multiple-beam models for CNTs [95, 96].

3) In addition, when the surrounding elastic medium is very compliant (such as polymers), the lowest resonant frequency predicted by the present model is almost coincident with the lowest natural frequency given by the existing single-beam model, while other new intertube resonant frequencies predicted by the present model are much higher than the lowest natural frequency given by the single-beam model.

4) Both the Timoshenko-beam effect and the double-beam effect are significant when the wavelength of DWNTs is just a few times larger than the outer diameter of DWNTs. In particular, it is the case when the higher-order frequencies (within the terahertz range) of short DWNTs (of smaller aspect ratio around or below 20) are considered.

5) On the other hand, if only the single lowest (first-order) resonant frequency is concerned, the classical single-Euler-beam model is accurate enough, any double-beam model or Timoshenko-beam model is not needed even for short MWNTs.

♦ Wave Propagation in MWNTs

1) For N-wall CNT, the multiple-Euler-beam model predicts (N-1) critical frequencies, while the multiple-Timoshenko-beam model predicts at least (2N-1) critical frequencies. For example, for DWNT, it is found that there is only one terahertz critical frequency based on the double-Euler-beam model, or there are a few (say, 3 or 4, depending on the diameters) terahertz critical frequencies based on the double-Timoshenko-beam model.

2) Sound wave propagation in MWNTs is essentially coaxial only when the frequency is much below all critical frequencies, and becomes substantially non-coaxial when the frequency is higher than at least one of the (N-1) critical frequencies. In the latter case, the sound speeds predicted by the multiple-beam model are significantly higher or lower than that given by the existing single-beam model, depending not only on the frequency but also on the vibrational modes.

3) When the frequency is close to or higher than the lowest critical frequencies, rotary inertia and shear deformation, incorporated by Timoshenko-beam model, have a substantial effect on the wave speeds especially for MWNTs of larger radii. In this case, the sound speeds predicted by the present model are significantly higher or lower than that given by the existing single-Euler-beam model. These results have been found to be in good agreement with more recent molecular dynamics simulations [97].

4) In particular, Timoshenko-beam effects significantly lower the value of the lowest critical frequency especially for MWNTs of larger radii. Hence, multiple-Timoshenko-beam model is more relevant for terahertz wave propagation in CNTs.

♦ Vibration and Instability of CNTs Conveying Fluid

1) Internal moving fluid could substantially affect resonant frequencies especially for suspended longer CNTs of larger innermost radius at higher flow velocity. Supported CNTs lose stability by static buckling, while cantilever CNTs lose stability by flutter at a certain critical flow velocity. In particular, the critical flow velocity for structural instability in some cases could fall within the range of practical significance.

2) On the other hand, our results indicate that a moderately stiff surrounding elastic medium (such as polymer with k=1GPa) can significantly reduce the effect of internal moving fluid on vibrational frequencies and suppress or eliminate the flow-induced flutter instability, while a very soft surrounding elastic medium (such as bio-tissue with k=1 KPa) has almost no effect on vibrational frequencies and the decaying rate of amplitude.

3) We believe that these results could provide useful data for the proposed application of CNTs as nanopipes conveying fluid. Also, the study of the dependence of resonant frequencies of CNTs conveying fluid on the flow velocity could offer a simple method to estimate the internal flow velocity by measuring the change in resonant frequencies.

9.2 Future Plans

♦ **Structure instability of CNTs due to van der Waals force**

Recently, suspended parallel and crossing array of CNTs has been proposed as a promising design towards CNT-based nanoelectonics [10, 22]. In such a design, because the van der Waals attractive forces between suspended CNTs and the substrate and any two adjacent CNTs have a crucial effect on the deformation of suspended CNTs, structural instability of suspended CNTs would be a major concern. Most recently, we studied structural instability of an elastic film under surface van der Waals forces based on Kerr's model [159,

160]. Structural instability of suspended CNTs interacting with the substrate can be studied using the elastic-beam model of CNTs by taking the attractive forces between CNTs and the substrate into account. This offers an interesting topic for future work.

♦ Deflection and vibration of SWNT ropes with individual deflection curves

SWNT ropes have been used in various nanodevices, such as probes in scanning probe microscopy [15], and nanotweezers [17]. The multiple-beam model can be modified to study the effects of the intertube relative displacements on the mechanical performance of SWNT ropes, and deflection, vibrational behavior and delamination of SWNT ropes. For example, when the intertube debonding force or the elastic energy stored in individual SWNTs exceeds a critical value, it is anticipated that delamination of individual CNTs from the SWNT ropes could occur. This significant issue for CNT ropes has not been studied in the literature.

♦ Contact mechanics of CNTs

When CNTs are used as building blocks of nanodeviecs, the electrostatic or van der Waals interaction between neighboring nanotubes or between nanotubes and other materials has a decisive effect on the deformation of the CNTs [10, 161]. Such deformation has an essential influence on electronic performance of CNT-based electronics, and can be studied by

crossing-beam and crossing-tube models with the assumption that the interacting force between the crossing nanotubes depends on the distance between the crossing nanotubes at the point of contact. Our recent studies [159, 160] indicated that the van der Waals like interacting forces between two bodies could lead to surface morphological instability of the contacting bodies. We believe that the morphological instability of CNTs is a significant research topic for contact mechanics of CNTs.

♦ Non-linear vibration of MWNTs

The present work is limited to infinitesimal linear free vibration of MWNTs. Although there is evidence that non-coaxial vibrational frequencies and modes predicted by the simple linear double-beam model are found to agree well with more recent atomistic simulations [95, 96], the non-linearity of the intertube van der Waals interaction would play a significant role in moderate or large amplitude non-coaxial vibration of MWNTs. Since CNTs has remarkable flexibility under axial compression or bending [23, 42], large-amplitude non-linear vibration of MWNTs could be an interesting research topic for CNTs.

Reference

1. Iijima, S., *Helical microtubules of graphitic carbon.* Nature, 1991. **354**: p. 56-58.
2. Ball, P., *Roll up for the revolution.* Nature, 2001. **414**: p. 142-144.
3. Baughman, R.H., A.A. Zakhidov, and W.A. de Heer, *Carbon Nanotubes--the Route Toward Applications.* Science, 2002. **297**: p. 787-792.
4. Ebbesen, T.W., *Carbon Nanotubes.* Annual review of materials science, 1994. **24**: p. 235-264.
5. Yakobson, B.I. and R.E. Smalley, *Fullerene Nanotubes: $C_{1,000,000}$ and Beyond.* American Scientist, 1997. **85**: p. 324-337.
6. Dresselhaus, M., G. Dresselhaus, and R. Saito, *Carbon Nanotues.* Physics World, 1998(January): p. 33.
7. Dai, H., *Carbon nanotubes: Opportunities and Challenges.* Surface Science, 2002. **500**: p. 218-241.
8. Dekker, C., *Carbon Nanotubes As Molecular Quantum Wires.* Physics Today, 1999. **52**(5): p. 22-28.
9. Collins, P.G. and P. Avouris, *Nanotubes for electronics.* Scientific American, 2000. **283**(6): p. 62-70.
10. Rueckes, T., et al., *Carbon Nonotube-Based Nonvolatile Random Access Memory for Molecular Computing.* Science, 2000. **289**: p. 94-97.
11. Derycke, V., et al., *Carbon nanotube inter- and intramolecular logic gates.* Nanoletters, 2001. **1**: p. 453-456.
12. Bachtold, A., et al., *Logic Circuits with Carbon Nanotube Transistors.* Science, 2001. **294**: p. 1317-1320.
13. Chung, D.S., et al., *Carbon nanotube electron emitters with a gated structure using backside exposure processes.* Applied Physics Letters, 2002. **80**: p. 4045-4047.
14. Tans, S.J., A.R.M. Verschueren, and C. Dekker, *Room-temperature transistor based on a single carbon nanotube.* Nature, 1998. **393**: p. 49-52.
15. Dai, H., et al., *Nanotubes as nanoprobes in scanning probe microscopy.* Nature, 1996. **384**: p. 147-150.

16. Collins, P.G., et al., *Nanotube Nanodevice.* Science, 1997. **278**: p. 100-103.
17. Kim, P. and C.M. Lieber, *Nanotube nanotweezers.* Science, 1999. **286**: p. 2148-2150.
18. Cumings, J. and A. Zettl, *Low-Friction Nanoscale Linear Bearing Realized from Multiwall Carbon Nanotubes.* Science, 2000. **289**: p. 602-604.
19. Ahlskog, M., et al., *Multiwalled carbon nanotubes as building blocks in nanoelectronics.* Journal of Low Temparture Physics, 2001. **124**: p. 335-352.
20. Snow, E.S., P.M. Campbell, and J.P. Novak, *Singlewall carbon nanotube atomic force microscope probes.* Applied Physics Letters, 2002. **80**: p. 2002-2004.
21. Dequesnes, M., S.V. Rotkin, and N.R. Aluru, *Calculation of pull-in voltages for carbon-nanotube-based nanoelectromechanical switches.* Nanotechnology, 2002. **13**: p. 120-131.
22. Postma, H.W.C., et al., *Carbon Nanotube Single-Electron Transistors at Room Temperature.* Science, 2000. **293**: p. 76-79.
23. Lourie, O., D.M. Cox, and H.D. Wagner, *Buckling and Collapse of Embedded Carbon Nanotubes.* Physical Review Letters, 1998. **81**: p. 1638-1641.
24. Calvert, P., *Nanotube composites: A recipe for strength.* Nature, 1999. **399**: p. 210-211.
25. Bower, C., et al., *Deformation of carbon nanotubes in nanotube-polymer composites.* Applied Physics letters, 1999. **74**: p. 3317-3319.
26. Qian, D., et al., *Load transfer and deformation mechanisms in carbon nanotube-polystyrene composites.* Applied Physics Letters, 2000. **76**: p. 2868-2870.
27. Thostenson, E.T., Z. Ren, and T.W. Chou, *Advances in the science and technology of carbon nanotubes and their composites: a review.* Composite Science and Technology, 2001. **61**: p. 1899-1912.
28. Lau, K.T. and D. Hui, *The revolutionary creation of new advanced materials?carbon nanotube composites.* Composite Part B, 2002. **33**(4): p. 263-277.
29. Harris, P.J.F., *Carbon nanotubes and related structures, new materials for the twenty-first century.* 2000.
30. Gibson, R.F. and E. Ayorinde, *A basic review of the vibrations of carbon nanotubes and their composites.* ASME International Mechanical Engineering Congress, November 13-19, Anaheim, California, 2004.

31. Finegan, I.C., G.G. Tibbetts, and R.F. Gibson, *Modeling and characterization of damping in carbon nanofiber/polypropylene composites.* Composite Science and Technology, 2003. **63**: p. 1629-1635.
32. Files, B.S., *Processing of carbon nanotubes for revolutionary space applications.* American Institute of Aeronautics and Astronautics (http://mmptdpublic.jsc.nasa.gov/jscnano/pubs/AIAA-3.PDF), 2000. **5345**: p. 1-5.
33. Roschier, L., et al., *Multiwalled carbon nanotubes as ultrasensitive electrometers.* Applied Physics Letters, 2001. **78**: p. 3295-3297.
34. Ishikawa, M., M. Yoshimura, and K. Ueda, *A study of friction by carbon nanotube tip.* Applied Surface Science, 2002. **188**: p. 456-459.
35. Dresselhaus, M.S., G. Dresselhaus, and R. Saito, *Carbon fibers based C_{60} and their symmetry.* Physical Review B, 1992. **45**: p. 6234-6242.
36. Lu, J.P., *Elastic Properties of Carbon Nanotubes and Nanoropes.* Physical Review Letters, 1997. **79**: p. 1297-1300.
37. Treacy, M.M.J., T.W. Ebbesen, and J.M. Gibson, *Exceptonally high young's modulus observed for individual carbon nanotubes.* Nature, 1996. **381**: p. 678-680.
38. Wong, E.W., P.E. Sheehan, and C.M. Lieber, *Nanobeam mechanics : elasticity, strength, and toughness of nanorods and nanotubes.* Science, 1997. **277**: p. 1971-1975.
39. Yu, M.F., et al., *Strength and Breaking Mechanism of Multiwalled Carbon Nanotubes Under Tensile Load.* Science, 2000. **287**: p. 637-640.
40. Yu, M.F., et al., *Tensile Loading of Ropes of Single Wall Carbon Nanotubes and their Mechanical Properties.* Physical Review Letters, 2000. **84**: p. 5552-5555.
41. Yakobson, B.I., C.J. Brabec, and J. Bernholc, *Nanomechanics of Carbon Tubes: Instabilities beyond Linear Response.* Physical Review Letters, 1996. **76**: p. 2511-2514.
42. Falvo, M.R., et al., *Bending and buckling of carbon nanotubes under large strain.* Nature, 1997. **389**: p. 582-584.
43. Schonenberger, C. and L. Forro, *Multiwall carbon nanotubes.* Physics World, 2000. **June**: p. 37-41.
44. Tang, Z.K., et al., *Superconductivity in 4 Angstrom Single-Walled Carbon Nanotubes.* Science, 2001. **292**: p. 2462-2465.

45. Kane, C.L. and E.J. Mele, *Size, Shape, and Low Energy Electronic Structure of Carbon Nanotubes.* Physical Review Letters, 1997. **78**: p. 1932-1935.
46. Yang, L. and J. Han, *Electronic Structure of Deformed Carbon Nanotubes.* Physical Review Letters, 2000. **85**: p. 154-157.
47. Maiti, A., A. Svixhenko, and M.P. Anantram, *Electronic Transport through Carbon Nanotubes: Effects of Structural Deformation and Tube Chirality.* Physical Review Letters, 2002. **88**: p. 126805.
48. Nardelli, M.B. and J. Bernholc, *Mechanical deformations and coherent transport in carbon nanotubes.* Physical Review B, 1999. **60**: p. R16338-R16341.
49. Liu, L., C.S. Jayanthi, and S.Y. Wu, *Structural and electronic properties of a carbon nanotorus: Effects of delocalized and localized deformations.* Physical Review Letters, 2001. **64**: p. 033412.
50. Tombler, T.W., et al., *Reversible electromechanical characteristics of carbon nanotubes under local-probe manipulation.* Nature, 2000. **405**: p. 769-772.
51. Schulz, W., *Crafting a nantional nanotechnology effort.* Nanotechnology Chemical & Engineering News (http://pubs.acs.org/cen/nanotechnology/7842/7842government.html), 2000: p. 39-42.
52. Gadd, G.E., et al., *The World's smallest gas cylinder.* Science, 1997. **277**: p. 933-936.
53. Che, G., et al., *carbon nanotubule membranes for electrochemical energy Storage and production.* Nature, 1998. **393**: p. 346-349.
54. Waters, J.F., et al., *Buckling instability in multiwalled carbon nanotubes under uniaxial compression.* Applied Physics Letters, 2004. **85**: p. 1787-1789.
55. Poncharal, P., et al., *Electrostatic deflections and electromechanical resonances of carbon nanotubes.* Science, 1999. **283**: p. 1513-1516.
56. Ruoff, R.S., et al., *Radial deformation of carbon nanotubes by van der Waals forces.* Nature, 1993. **364**: p. 514-516.
57. Iijima, S., et al., *Structural flexibility of carbon nanotubes.* Journal of Chemical Physics, 1995. **104**: p. 2089-2092.
58. Salvetat, J.-P., et al., *Elastic and Shear Moduli of Single-Walled Carbon Nanotube Ropes.* Physical Review Letters, 1999. **82**: p. 944-947.
59. Salvetat, J.-P., et al., *Elastic Modulus of Ordered and Disordered Multiwalled*

Carbon Nanotubes. Advanced Materials, 1999. **11**: p. 161-165.

60. Sanchez-Portal, D., et al., *Ab initio structural elastic, and vibraional properties of carbon nanotubes.* Physical Review B, 1999. **59**: p. 12678-12688.
61. Srivastava, D., M. Menon, and K. Cho, *Anysotropic nanomechanics of boron nitride nanotubes: Nanostructred "skin" effect.* Physical Review B, 2001. **59**: p. 12678-12688.
62. Hernandez, E., et al., *Elastic properties of C and BxCyNz composite nanotubes.* Physical Review Letters, 1998. **80**: p. 4502-4505.
63. Srivastava, D., M. Menon, and K. Cho, *Nanoplasticity of single-wall carbon nanotubes under uniaxial compression.* Physical Review Letters, 1999. **83**: p. 2973-2976.
64. Ru, C.Q., *Effect of van der Waals forces on axial buckling of a double-walled carbon nanotube.* Journal of Applied Physics, 2000. **87**: p. 7227-7231.
65. Ru, C.Q., *Effective bending stiffness of carbon nanotubes.* Physical Review B, 2000. **62**: p. 9973-9976.
66. Ru, C.Q., *Elastic buckling of single-walled carbon nanotube ropes under high pressure.* Physical Review B, 2000. **62**: p. 10405-10408.
67. Ru, C.Q., *Column buckling of multiwalled carbon nanotubes with interlayer radial displacements.* Physical Review B, 2000. **62**: p. 16962-16967.
68. Ru, C.Q., *Degraded axial buckling strain of multiwalled carbon nanotubes due to interlayer slips.* Journal of Applied Physics, 2001. **89**: p. 3426-3433.
69. Ru, C.Q., *Axially compressed buckling of a doublewalled carbon nanotube embedded in an elastic medium.* Journal of the Mechanics and Physics of Solids, 2001. **49**: p. 1265-1279.
70. Yoon, J., C.Q. Ru, and A. Mioduchowski, *Noncoaxial resonance of an isolated multiwall carbon nanotube.* Physical Review B, 2002. **66**: p. 233402.
71. Yoon, J., C.Q. Ru, and A. Mioduchowski, *Vibration of embedded multiwall carbon nanotubes.* Composite Science and Technology, 2003. **63**: p. 1533-1542.
72. Yoon, J., C.Q. Ru, and A. Mioduchowski, *Sound wave propagation in multiwall carbon nanotubes.* Journal of Applied Physics, 2003. **93**: p. 4801-4806.
73. Yoon, J., C.Q. Ru, and A. Mioduchowski, *Timoshenko beam effects on transverse wave propagation in carbon nanotubes.* Composite Part B, 2004. **35**: p. 87-93.
74. Yoon, J., C.Q. Ru, and A. Mioduchowski, *Terahertz vibration of short carbon*

nanotubes modeled as Timoshenko beams. Journal of Applied Mechanics, 2005. **72**: p. 10-17.

75. Yoon, J., C.Q. Ru, and A. Mioduchowski, *Vibration and instability of carbon nanotubes conveying fluid.* Composite Science and Technology, 2005. **65**: p. 1326-1336.
76. Yoon, J., C.Q. Ru, and A. Mioduchowski, *Flow-induced flutter instability of cantilever carbon nanotubes.* International Journal of Solids and Structures, 2005. **(available online)**.
77. Garg, Y., J. Han, and S. Sinnott, *Interactions of carbon-nanotubule proximal probe tips with diamond and graphene.* Physical Review Letters, 1998. **81**: p. 2260-2263.
78. Popov, V.N., V.E. Van Doren, and M. Balkanski, *Elastic properties of single-walled carbon nanotubes.* Physical Review B, 2000. **61**(4): p. 3078-3084.
79. Timoshenko, S., *Vibration problems in engineering.* 1974.
80. Doyle, J.F., *Wave propagation in structures.* 1989.
81. Cornwell, C.F. and L.T. Wille, *Elastic properties of single-walled carbon nanotues in compression.* Solid State Communications, 1997. **101**: p. 555-558.
82. Ozaki, T., Y. Iwasa, and T. Mitani, *Stiffness of Single-Walled Carbon Nanotubes under Large Strain.* Physical Review Letters, 2000. **84**: p. 1712-1715.
83. Venkateswaran, U.D., et al., *Probing the single-wall carbon nanotube bundle: Raman scattering under high pressure.* Physical Review B, 1999. **59**: p. 10928-10934.
84. Peters, M.J., et al., *Structural phase transition in carbon nanotube bundles under pressure.* Physical Review B, 2000. **61**: p. 5939-5944.
85. Gaal, R., J.-P. Salvetat, and L. Forro, *Pressure dependence of the resistivity of single-wall carbon nanotube ropes.* Physical Review B, 2000. **61**: p. 7320-7323.
86. Tang, D.S., et al., *The electrical behavior of carbon nanotubes under high pressure.* Journal of Physics and Chemistry of Solids, 2000. **61**: p. 1175-1178.
87. Wang, C.Y., C.Q. Ru, and A. Mioduchowski, *Axially compressed buckling of pressured multiwall carbon nanotubes.* Journal of Nanoscience and Technology, 2003. **No. 40**: p. 3893-3903.
88. Govindjee, S. and J.L. Sackman, *On the use of continuum mechanics to estimate the properties of nanotubes.* Solid State Communications, 1999. **110**: p. 227-230.

89. Kahn, D., K.W. Kim, and M.A. Stroscio, *Quantized vibrational modes of nanospheres and nanotubes in the elastic continuum model.* Journal of Applied Physics, 2001. **89**: p. 5107-5111.
90. Harik, V.M., *Ranges of applicability for the continuum beam model in the mechanics of carbon nanotubes and nanorods.* Solid State Communications, 2001. **120**: p. 331-335.
91. Wang, Z.L., et al., *Nano-Scale Mechanics of Nanotubes, Nanowires, and Nanobelts.* Advanced Engineering Materials, 2001. **3**: p. 657-661.
92. Qian, D., et al., *Mechanics of carbon nanotubes.* Applied Mechanics Reviews, 2002. **55**: p. 495-533.
93. Yu, J., R.K. Kalia, and P. Vashiashta, *Phonons in graphitic tubules: A tight-binding molecular dynamics study.* The Journal of Chemical Physics, 1995. **103**(15): p. 6697-6705.
94. Dresselhaus, M.S. and P.C. Eklund, *Phonons in carbon nanotubes.* Advances in Physics, 2000. **49**: p. 705-814.
95. Zhao, Y., et al., *Energy Dissipation Mechanisms in Carbon Nanotube Oscillators.* Physical Review Letters, 2003. **91**: p. 175504.
96. Li, C. and T.W. Chou, *Vibrational behaviors of multiwalled-carbon-nanotube-based nanomechanical resonators.* Applied physics Letters, 2004. **84**(1): p. 121-123.
97. Wang, L. and H. Hu, *Flexural wave propagation in single-walled carbon nanotubes.* Physical Review B, 2005. **71**: p. 195412.
98. Gere, J.M., *Mechanics of Materials (fifthe edition).* Brooke/Cole, 2001.
99. Nardelli, M.B., B.I. Yakobson, and J. Bernholc, *Brittle and Ductile Behavior in Carbon Nanotubes.* Physical Review Letters, 1998. **81**: p. 4656-4659.
100. Yao, N. and V. Lordi, *Carbon nanotube caps as springs: Molecular dynamics simulations.* Physical Review B, 1998. **58**: p. 12649-12651.
101. Lanir, Y. and Y.C.B. Fung, *Fiber composite columns under compressions.* Journal of Composite Materials, 1972. **6**: p. 387-401.
102. Kerr, A.D., *On the formal development of elastic foundation models.* Ingenieur-Archiv, 1984. **54**: p. 455-464.
103. Krishnan, A., et al., *Young's modulus of single-walled nanotubes.* Physical Review B, 1998. **58**: p. 14013.
104. Charlier, J.-C. and J.-P. Michenaud, *Energetics of multilayered carbon tubules.*

Physical Review Letters, 1993. **70**: p. 1858-1861.

105. Kolmogorov, A.N. and V.H. Crespi, *Smoothest Bearings: Interlayer Sliding in Multiwalled Carbon Nanotubes.* Physical Review Letters, 2000. **85**: p. 4727-4730.
106. Girifalco, L.A. and R.A. Lad, *Energy of Cohesion, Compressibility, and the Potential Energy Functions of the Graphite System.* The Journal of Chemical Physics, 1956. **25**: p. 693-697.
107. Kiang, C.-H., et al., *Size Effects in Carbon Nanotubes.* Physical Review Letters, 1998. **81**: p. 1869-1872.
108. Saito, R., et al., *Anomalous potential barrier of double-wall carbon nanotube.* Chemical Physics Letters, 2001. **348**(3-4): p. 187-193.
109. Rao, S.S., *Natural vibrations of systems of elastically connected Timoshenko beams.* The Journal of the Acoustical Society of America, 1974. **55**: p. 1232-1237.
110. Hutchinson, J.R., *Shear coefficients for Timoshenko beam theory.* Journal of Applied Mechanics, 2001. **68**: p. 87-92.
111. Cowper, G.R., *The shear coefficient in Timoshenko's beam theory.* Journal of Applied Mechanics, 1966. **33**: p. 335-340.
112. Chopra, N.G. and A. Zettl, *Measurement of the elastic modulus of multiwall boron nitride nanotubes.* Solid State Communications, 1998. **105**: p. 297-300.
113. Paulson, S., et al., *In situ resistance measurements of strained carbon nanotubes.* Applied Physics Letters, 1999. **75**: p. 2936-2938.
114. Gao, R., Z. Pan, and Z.L. Wang, *Work function at the tips of multiwalled carbon nanotubes.* Applied Physics Letters, 2001. **78**: p. 1757-1759.
115. Zhao, Y.-P., et al., *Frequency-dependent electrical transport in carbon nanotubes.* Physical Review B, 2001. **64**: p. 201402.
116. Kasumov, A.Y., et al., *Conductivity and atomic structure of isolated multiwalled carbon nanotubes.* Europhysics Letters, 1998. **43**: p. 89-94.
117. Suenaga, K., C. Colliex, and S. Iijima, *In situ electron energy-loss spectroscopy on carbon nanotubes during deformation.* Applied Physics Letters, 2001. **78**: p. 70-72.
118. Hassanien, A., et al., *Imaging the interlayer interactions of multiwall carbon nanotubes using scanning tunneling microscopy and spectroscopy.* Applied Physics Letters, 2001. **79**: p. 4210-4212.

119. Miyamoto, Y., S. Saito, and D. Tomanek, *Electronic interwall interactions and charge redistribution in multiwall nanotubes.* Physical Review B, 2001. **65**: p. 041402-5.
120. Collins, P.G., et al., *Current Saturation and Electrical Breakdown in Multiwalled Carbon Nanotubes.* Physical Review Letters, 2001. **86**: p. 3128-3131.
121. Lu, W., J. Dong, and Z. Li, *Optical properties of aligned carbon nanotube systems studied by the effective-medium approximation method.* Physical Review B, 2000. **63**: p. 033401-4.
122. Jin, Z., et al., *Nonlinear optical properties of some polymer/multiwall carbon nanotube composites.* Chemical Physics Letters, 2000. **318**: p. 505-510.
123. Smith, B.W. and D.E. Luzzi, *Formation mechanism of fullerene peapods and coaxial tubes: a path to large scale synthesis.* Chemical Physics Letters, 2000. **321**(1-2): p. 169-174.
124. Bandow, S., et al., *Raman scattering study of double-wall carbon nanotubes derived from the chains of fullerenes in single-wall carbon nanotubes.* Chemical Physics Letters, 2001. **337**(1-3): p. 48-54.
125. Seelig, J.M. and W.H. Hoppmann, *Impact on an elastically connected double-beam system.* Journal of Applied Mechanics, 1964. **31**: p. 621.
126. Majorana, E. and Y. Ogawa, *Mechanical thermal noise in coupled oscillators.* Physics Letters A, 1997. **233**: p. 162-168.
127. Burrows, B.L. and M. Cohen, *Coupled N-dimensional harmonic oscillator systems.* Molecular Physics, 2000. **98**: p. 1083-1088.
128. Wagner, H.D., et al., *Stress-induced fragmentation of multiwall carbon nanotubes in a polymer matrix.* Applied Physics Letters, 1998. **72**: p. 188-190.
129. Thostenson, E.T., et al., *Carbon nanotube/carbon fibers hybrid multiscale composites.* Applied Physics Letters, 2002. **91**: p. 6034-6036.
130. Hahn, H.T. and J.G. Williams, *Compression failure mechanisms in unidirectional composites.* Composite Materials : Testing and Design, 1984. **7**: p. 115-139.
131. Sirtori, C., *Applied physics: Bridge for the terahertz gap.* Nature, 2002. **417**: p. 132-133.
132. Jeon, T., et al., *Terahertz conductivity of anisotropic single walled carbon nanotube films.* Applied Physics Letters, 2002. **80**: p. 3403-3405.

133. Antoneli, G.A., et al., *Picosecond ultrasonics study of the vibrational modes of a nanostructure.* Journal of Applied Physics, 2002. **91**: p. 3261-3267.
134. Knap, W., et al., *Nonresonant detection of terahertz radiation in field effect transistors.* Journal of Applied Physics, 2002. **91**(11): p. 9346-9353.
135. Brauns, E.B., et al., *Complex Local Dynamics in DNA on the Picosecond and Nanosecond Time Scales.* Physical Review Letters, 2002. **88**: p. 158101.
136. Reulet, B., et al., *Acoustoelectric Effects in Carbon Nanotubes.* Physical Review Letters, 2000. **85**(13): p. 2829-2832.
137. Buitelaar, M.R., et al., *Multiwall Carbon Nanotubes as Quantum Dots.* Physical Review Letters, 2002. **88**: p. 156801.
138. Landau, L.D. and E.M. Lifshitz, *Theory of Elasticy.* 1995.
139. Evans, E. and H. Bowman, *Biomembrane templates for nanoscale conduits and networks.* Science, 1996. **273**: p. 933-935.
140. Gao, Y. and Y. Bando, *Carbon nanothermometer containing gallium.* Nature, 2002. **415**: p. 599.
141. Hummer, G., J.C. Rasaiah, and J.P. Noworyta, *Water conduction through the hydrophobic channel of a carbon nanotubes.* Nature, 2001. **414**: p. 188-190.
142. Karlsson, A., *Networks of nanotubes and containers.* Nature, 2001. **409**: p. 150-152.
143. Liu, J., A.G. Rinzler, and H.J. Dai, *Fullerene pipes.* Science, 1998. **280**: p. 1253-1256.
144. Galanov, B.A., S.B. Galanov, and Y. Gogotsi, *Stress-strain state of multiwall carbon nanotubes under internal pressure.* Journal of Nanoparticl Research, 2002. **4**: p. 207-214.
145. Gogotsi, Y., *In situ multiphase fluid experiments in hydrothermal carbon nanotubes.* Applied Physics Letters, 2001. **79**: p. 1021-1023.
146. Mao, Z. and S.B. Sinnott, *A computational study of molecular diffusion and dynamics flow through CNTs.* The Journal of Physical Chemistry, 2000. **104**: p. 4618-4624.
147. Megaridis, C.M., et al., *Attoliter fluid experiments in individual closed-end CNTs.* Physics of Fluids, 2002. **14**: p. L5-L8.
148. Skoulidas, A., et al., *Rapid transport of gases in carbon nanotubes.* Physical Review Letters, 2002. **89**: p. 185901.
149. Sokhan, V.P., D. Nicholson, and N. Quirke, *Fulid flow in nanopores: Accurate*

boundary conditions for carbon nanotubes. The Journal of Chemical Physics, 2002. **117**: p. 8531-8539.

150. Supple, S. and N. Quirke, *Rapid imbibition of fluids in CNTs.* Physical Review Letters, 2003. **90**: p. 214501.
151. Tuzun, R.E., et al., *Dynamics of fluid flow inside carbon nanotubes.* Nanotechnology, 1996. **7**: p. 241-246.
152. Chen, S.S., *Flow-induced vibration of circular cylindrical structures.* Hamisphere Publishing, 1987.
153. Paidoussis, M.P., *Fluid-Structure Interaction.* Academic Press, 1998. **vol. 1.**
154. Paidoussis, M.P. and G.X. Li, *Pipes conveying fluid: a model dynamical problem.* Journal of Fluids and Structures, 1993. **7**: p. 137-204.
155. Palmer, A.C. and J.A.S. Baldry, *Lateral buckling of axially constrainted pipelines.* Journal of Petroleum Technology, 1974. **26**: p. 1283.
156. Fung, Y.C., *An introduction to the theory of aeroelasticity.* Dover Publications, 1993.
157. Benjamin, T.B., *Dynamics of a system of articulated pipes conveying fluid. I. Theory.* Proceedings of the Royal Society (London), 1961. **A 261**: p. 457-486.
158. Shull, K.R., *Contact mechanics and the adhesion of soft solids.* Materials Science and Engineering, 2002. **R36**: p. 1-45.
159. Ru, C.Q., *Surface instability of an elastic thin film interacting with a suspended elastic plate.* Journal of Applied Mechanics, 2002. **69**: p. 97-103.
160. Yoon, J., C.Q. Ru, and A. Mioduchowski, *Surface Instability of a Bilayer Elastic Film due to Surface van der Waals Forces.* Submitted, 2005.
161. Hertel, T., R.E. Walkup, and P. Avouris, *Deformation of carbon nanotubes by surface van der Waals forces.* Physical Review B, 1998. **58**: p. 13870-13873.